

DTIC FILE COPY

UNIVERSITY OF CALIFORNIA, SAN DIEGO

BERKELEY • DAVIS • IRVINE • LOS ANGELES • RIVERSIDE • SAN DIEGO • SAN FRANCISCO



SANTA BARBARA • SANTA CRUZ

DEPARTMENT OF APPLIED MECHANICS AND
ENGINEERING SCIENCES, MAIL CODE R-011

LA JOLLA, CALIFORNIA 92093-0411

September 27, 1990

AD-A227 579

Department of the Navy
Office of the chief of Naval Research
800 North Quincy Street
Arlington, VA 22217-5000

Attention: M.M. Reischman
Director (Acting)
Mechanics Division

Ref: 500
Ser 1132/154

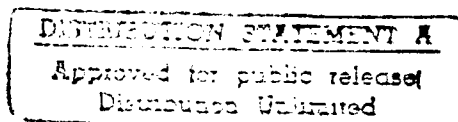


Dear Dr. Reischman,

Enclosed is the annual Performance Report for work performed under our project,
"Mechanics of Interface Cracks", grant number N00014-90-J-1398.

We trust this complies with your request.

Sincerely yours,



Robert Asaro
Robert Asaro
Dept. of AMES

Encl

RA/ba

100-1132-154

Introduction

Fracture of advanced materials, such as intermetallic alloys, ceramics, and composite materials nearly always begins at interfaces of one sort or another. Fibrous fractures, for example, initiate at the interfaces between second phase particles (or reinforcement fibers, whiskers, etc) and the ductile matrix; the conditions for this to occur are sensitive to both matrix constitutive properties as well as to the chemistry and structure of the interfaces between the two phases. Interfacial cleavage involves the initiation of micro-cracks and their propagation along interfaces and transgranular cleavage often initiates at interfacial sites, e.g. twin boundaries in intermetallic compounds, especially those with non-cubic crystal structures. Here again, the conditions required for this to occur are sensitive to the constitutive properties of the matrix materials as well as to the interfacial properties themselves. Intermetallic alloys, in particular, are known to possess complicated thermal and strain rate dependencies that can lead to either brittle or ductile behavior which in any event are very much dependent upon the loading conditions.

Our research over the past three years has been concerned with providing a theoretical and computational framework for analyzing the deformation of complex crystalline materials, like intermetallic alloys, and in particular of the failure of interfaces within these materials and between these materials and other phases. In addition, we have been developing experimental methods to study the failure of interfaces between metals and metals and ceramics. Our experimental studies are to be directly correlated with our theoretical/computational work. Specifically, our aims are to

1) conduct computational, and complimentary experimental studies of interface crack mechanics, including crack growth, at interfaces separating crystalline phases described by physically based slip theories;

2) extend our physically based slip theories to specifically account for the dislocation micromechanisms that are peculiar to more complex crystalline materials such as ordered intermetallic compounds;

3) conduct analytical and computational modeling of the deformation and failure of ordered intermetallic alloys, and especially of the deformation and failure near interfaces; and

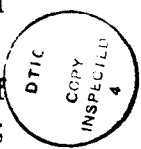
4) further develop our vacuum diffusion bonding methods to prepare metal/ceramic, alloy/alloy, and intermetallic/metal (ceramic) interfaces with controlled defects.

Our ongoing experimental work has been concerned with the Nb/Al_2O_3 interface. We have used vacuum diffusion bonding methods to prepare pre-cracked interfaces in this system and have been conducting experiments to measure the fracture toughness. We have extended these studies to the interfaces of Ni_3Al and Nb and $TiAl/Nb$ for the purposes of measuring interface toughness and also to correlate the interface toughness with ductility and toughness of composites. We have also formulated a flow theory for

STATEMENT "A" per Dr. Lekoudis
ONR/Code 1132
TELECON 10/10/90

CC

Availability Codes	
Dist	Avail and/or Special
A-1	



per call

intermetallic alloy materials that accounts for deviations from Schmid's rule. We have previously shown that such deviations have important implications for the stability of uniform flow.

During the next year, we plan to:

1) Continue our work of the past year on the analyses of the mechanics of cracks on interfaces. Our intention is to perform computational analyses of the very *near crack tip fields* under a complete range of mixed mode loadings *and* of the full fields for cracked specimen geometries of the type we are studying experimentally. We intend to explore the effects of geometric constraints on the development of the crack tip fields, and in particular, the influence of interface geometry on the buildup of hydrostatic stresses. The role of hydrostatic stress in determining the *failure modes* of the interfaces, and the resulting ductility of the microstructure in specimens containing the interface, will also be assessed.

2) Extend our computational studies of localized deformation to ordered intermetallic alloy systems, in particular Ni_3Al and later $TiAl$ alloys. As noted above, we have formulated a constitutive theory for such materials and have analyzed the behavior in single crystal Ni_3Al . We are now implementing the theory in our FEM codes to perform analyses of deformation processes in these materials.;

3) Residual stresses, due to incompatible thermal strains, are known to play an important role in the development and propagation of flaws and cracks along interfaces. We have formulated a finite strain theory for thermal strains, and have implemented this theory in our finite-element models for composite behavior, and interface fracture. We intend to carry out simulations of crack growth along interfaces of bimaterial couples such as Nb/Al_2O_3 for which the thermal strain mismatch is minimal and intermetallic compounds such as $TiAl$, Nb_3Al , and Ni_3Al/Nb for which thermal mismatch is significant; and

4) We will continue our experiments on the fracture of metal/ceramic and metal/metal interfaces prepared by diffusion bonding methods. We are currently conducting experimental studies of crack growth along Nb/Al_2O_3 interfaces which are prepared by vacuum diffusion bonding. We will be exploring the use of the bend specimen to subject interface crack tips to a wide range of mixed mode loadings in addition to the compact tension specimen we developed in the initial phase of our project. We will extend these studies to interfaces involving intermetallic compound/metal and intermetallic compound/ceramic couples.

Summary of Research

In the past three years, we have completed a series of analyses on 1) the structure of *interface crack tip fields*; 2) the full field analyses of the elastic-plastic fields associated with interface cracks and flaws; 3) the micromechanical and macromechanical process of crack and flaw propagation along interfaces; and 4) deformation at the tips of cracks lying on interfaces with structure. We have also completed the formulation of a flow theory for ordered intermetallic alloys. Our computations have been carried out for stationary cracks as well as for cracks propagating along interfaces where the phenomenology of propagation is governed by adhesive laws ascribed to the interface. Nine papers have been submitted

for publication. Four of these have appeared in print in 1990; one additional has been accepted for publication.

R.J. Asaro:

- 1) *Cracktip Fields in Ductile Crystals* (with J.R. Rice and D.E. Hawk), International Journal of Fracture **42**, 301 (1990).

R.J. Asaro and C.F. Shih:

- 2) *Elastic-Plastic Analysis of Cracks on Bimaterial Interfaces: Part I - Small Scale Yielding*, J. Appl Mechanics **55**, 299 (1988).
- 3) *Elastic-Plastic Analysis of Cracks on Bimaterial Interfaces: Part II - Structure of Small Scale Yielding Fields*, J. Appl. Mechanics **III**, 763 (1990).
- 4) *Elastic-Plastic Analysis of a Collinear Array of Cracks on a Bimaterial Interface*, J. Material Science and Engineering A **107**, 145 (1989).

R.J. Asaro, N.P. O'Dowd and C.F. Shih:

- 5) *Cracks on Bimaterial Interfaces: Plasticity Aspects*, in proceedings of the Acta/Scripta Metallurgica Conference on Bonding, Structure and Mechanical Properties of Metal/Ceramic Interfaces, 1989.
- 6) *Elastic-Plastic Analysis of Cracks on Bimaterial Interfaces: Part III - Large Scale Yielding*, submitted to J. Appl Mechanics (1989).
- 7) *Elastic-Plastic Analysis of Cracks on Bimaterial Interfaces: Part IV - Interfaces with Structure*, submitted to J. Appl Mechanics (1990).

R.J. Asaro, N.P. O'Dowd, C.F. Shih and A.G. Varias:

- 8) *Failure of Bimaterial Interfaces*, submitted for publication, Mat. Sci. and Eng. A **126**, 65 (1990).
- 9) *Crack Growth on Bimaterial Interfaces*, in proceedings of the Acta/Scripta Metallurgica Conference on Bonding, Structure, and Mechanical Properties of Metal/Ceramic Interfaces (1990)

A tenth manuscript authored by R.J. Asaro and M. Dao, entitled *The Mechanics of Plastic Flow in Ni_3Al* is under preparation; the work associated with it was completed during July/August 1990 at the University of California, San Diego.

Our initial studies under this project were concerned with the structure of plane strain interface crack tip fields. Specifically in Parts I and II of our four part series of articles (i.e., refs. 2 and 3 listed above), the structure of the crack tip field that develop under conditions pertaining to small scale yielding was determined. In reference 4, the stress and strain field that evolve under conditions producing contained yielding and fully plastic conditions were examined through a study of collinear interface crack geometries. These (primarily) numerical studies led to an understanding of the asymptotic structure of interface crack tip fields along with a correspondence of these fields to the well characterized small strain (HRR) fields in homogeneous media. In particular, it was found that the small scale

yielding fields of the interface crack are members of a family parameterized by a plastic phase angle, ξ , defined as

$$\xi = \varphi + \varepsilon \ln \left(\frac{K}{\sigma_0} \right)^2 = \hat{\phi} + \varepsilon \ln \left(\frac{K^2}{\sigma_0^2 \hat{L}} \right) = \phi + \varepsilon \ln \left(\frac{Q^2}{\sigma_0^2 L} \right)$$

where the parameters and L are defined vis-a-vis the linear elastic interface crack tip field as follows.

In terms of polar coordinates, r, θ , centered at the crack tip, the crack tip fields can be organized in the form

$$\sigma_{ij} = \sigma_0 \left(\frac{J}{\alpha \sigma_0 \varepsilon_0 r} \right)^{1/(n+1)} h_{ij}(\theta, \tilde{r}; \xi, n)$$

where n is a power law strainhardening index prescribed in connection with J_2 deformation, or J_2 flow theory. h_{ij} is a bounded function which, however, varies with $\tilde{r} (= r/(J/\sigma_0))$. For $-\pi/6 \leq \xi \leq \pi/6$ however, h_{ij} varies slowly with \tilde{r} so that the near tip field conforms closely with that of an HRR field. K is the complex stress intensity factor defined, with respect to the elastic crack tip asymptotic field, as

$$\sigma_{ij} = \frac{1}{\sqrt{2\pi r}} \left[\operatorname{Re}\{K r^{i\varepsilon}\} \tilde{\sigma}_{ij}(\theta; \varepsilon) + \operatorname{Im}\{K r^{i\varepsilon}\} \tilde{\sigma}_{ij}(\theta; \varepsilon) \right]$$

ε is a dimensionless bimaterial constant and L is a crack dimension. Our results showed that for cases involving two elastic-plastic media that the fields, in both materials, are parts of a single asymptotic field; the intensity of the stresses are determined by the yield strength of the weaker material whereas the angular distribution of stress about the crack tip is set by the strainhardening characteristics of the more weakly hardening material.

In reference 4, analyses involving *contained yielding* and *fully plastic* states were carried out. An interesting discovery was that the fields scaled with the value of the J integral when J was normalized by yield strength and crack length. In particular, a value J , prescribed as $J/(\sigma_0 \varepsilon_0 L)$ was found to scale the fields that developed between colinear arrays under conditions that produced deformation states ranging from small-scale yielding - to contained yielding - to fully plastic behavior.

Finite deformation analyses were carried out in references 5, 6, 7, 8 and in Part IV. Computational studies were performed using crystal plasticity theory as well as phenomenological J_2 flow theory. Our finite strain calculations have included studies of the deformation of cracks on interfaces with structure. An example of this is Fig. 1 which shows the deformed meshes for cracks lying on an interface between two materials described by a rate dependent, finite strain J_2 flow theory. The materials on either side of the interface differed by a factor of two in yield strength; their properties were taken to

match those of the dissimilar steels that we studied experimentally. The interface region had properties intermediate between these two phases.

Figure 1 indicates the strong influence of mixed mode loading in that our calculations were carried out for three values $\xi = -\pi/6, 0, \pi/6$. The crack tip openings, and associated extents of plastic deformation, are greatest for the mixed mode states. In fact, for a given value of the applied far field J , the crack tip opening was largest for the mixed mode state corresponding to $\xi = -\pi/6$. Figure 2 shows contours of hydrostatic stress which also illustrate the effects of mixed mode loading. A particularly remarkable feature is the shift in hydrostatic stress with mode from the softer to the harder materials as the mode shifts from that corresponding to $\xi = 0$. These particular calculations were part of a set of model studies of our experiments concerned with dissimilar steel interfaces. One such interface is shown in Fig. 3. Note that this interface is rather broad and is characterized by an *interdiffusion* zone of about $60 \mu\text{m}$ in thickness. Our observations showed that, as the initial crack began to propagate, it quickly travelled to the boundary of the transition zone and the softer steel. Given that the fracture mode was fibrous, this is, in fact, expected since our computations showed that the hydrostatic stresses are larger in the transition zone toward the softer steel. Fibrous fractures, which are driven by void initiation and growth, are accelerated by hydrostatic tensile states of stress.

Recent Work

Our more recent work has been concerned with the formulation of a flow theory for ordered intermetallic alloys. Ni_3Al was proposed as an initial example. One of the particularly interesting features of the dislocation mechanics in such crystalline materials is that they display strong departures from Schmid's rule of a *critical resolved shear stress*. Deviations from the Schmid rule of this type represent non-normality in the flow rule. Asaro and Rice have shown that there are indeed important implications of non-normality of this type regarding stable, uniform, plastic flow.

As part of this project, Dao and Asaro have formulated a flow rule for both rate independent and rate dependent materials. For rate independent materials, the flow rule takes the form (for each slip system)

$$\dot{\gamma}_{ms} = \frac{1}{h} \mathbf{Q} : \dot{\boldsymbol{\tau}}$$

where $\boldsymbol{\tau}$ is the shear stress phrased on slip system coordinates as shown in Fig. 4. This figure also indicates some typical micromechanical processes, involving dislocations, that give rise to the non-schmid effects. \mathbf{Q} is the dyad

$$\mathbf{Q} = \mathbf{s}\mathbf{m} + \boldsymbol{\sigma} : \mathbf{H} : \mathbf{L}^{-1}$$

where $\boldsymbol{\alpha}$ is the matrix of non-Schmid factors, i.e.

$$\alpha = \begin{pmatrix} \alpha_{ss} & 0 & \alpha_{sz} \\ 0 & \alpha_{mm} & \alpha_{mz} \\ \alpha_{sz} & \alpha_{mz} & \alpha_{zz} \end{pmatrix}.$$

For rate dependent materials, the flow law instead takes the form

$$\dot{\gamma} = \text{function}(\mathbf{Q} : \sigma; \text{material state}).$$

Dao and Asaro have analyzed the behavior of Ni_3Al within this framework and have calculated, based on experimental data, values for their non-Schmid coefficients.

We are currently in the process of implementing our theory in one of our FEM codes. Our initial objectives will be to study the development of flow patterns in single and polycrystalline microstructures of these materials and to then analyze the behavior of interfaces between Ni_3Al and Nb .

List of Participants and Status

S. Schoenfeld, Graduate Student

M. Dao, Graduate Student

Both of these students are in their second year.

Other Sponsored Research

"Fundamental Studies of Localized Plastic Deformation", NSF, 71,900.

Awards

R.J. Asaro has been awarded the TMS Champion H. Mattewson Gold Metal for 1991 for his research on micromechanics.

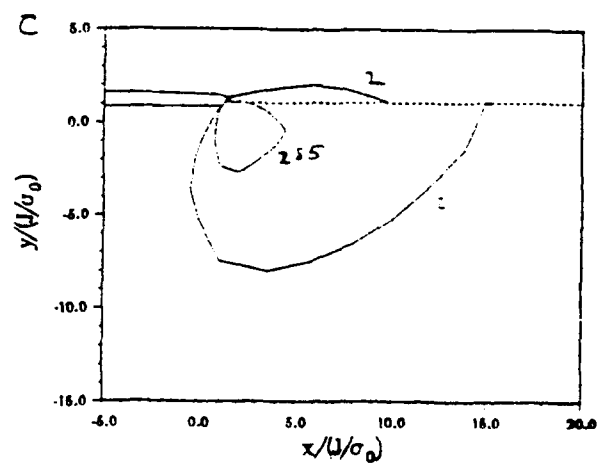
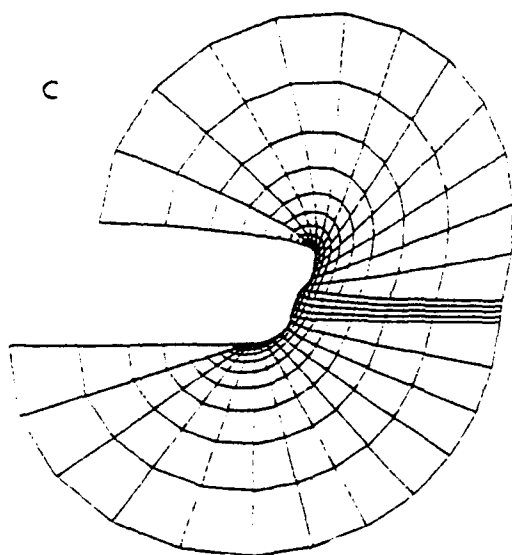
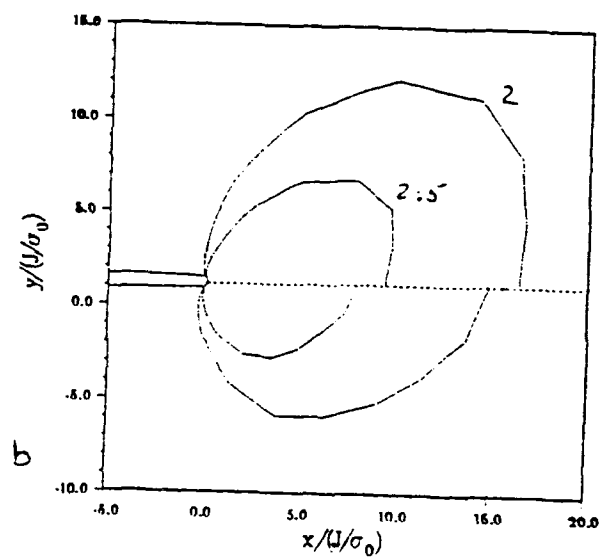
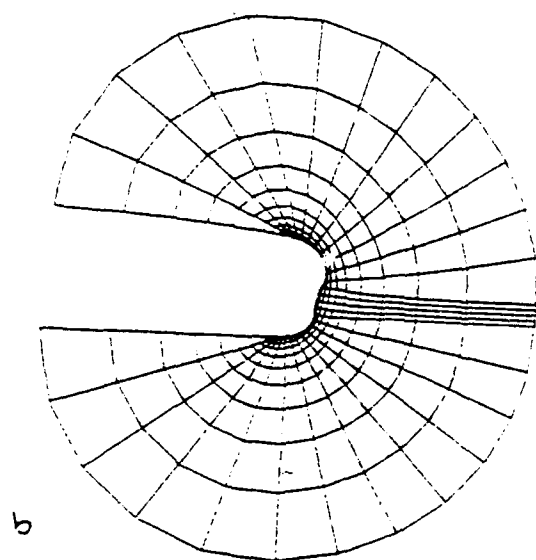
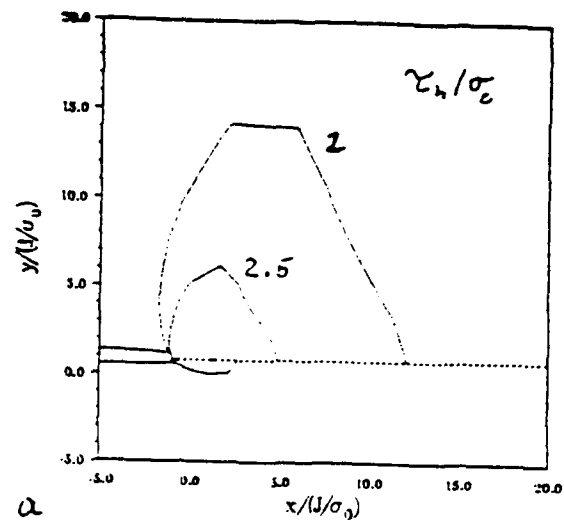
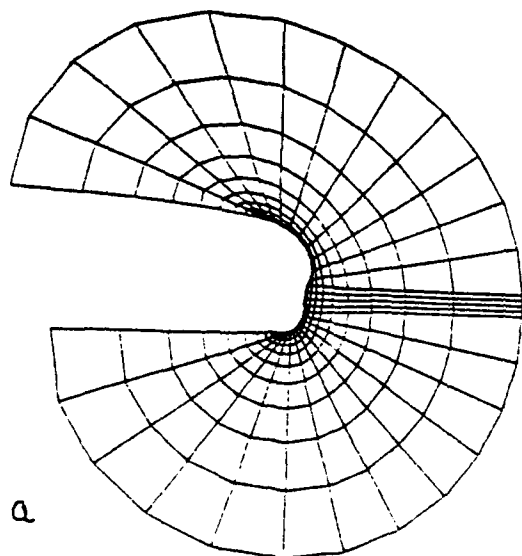


Fig. 1

Fig. 2

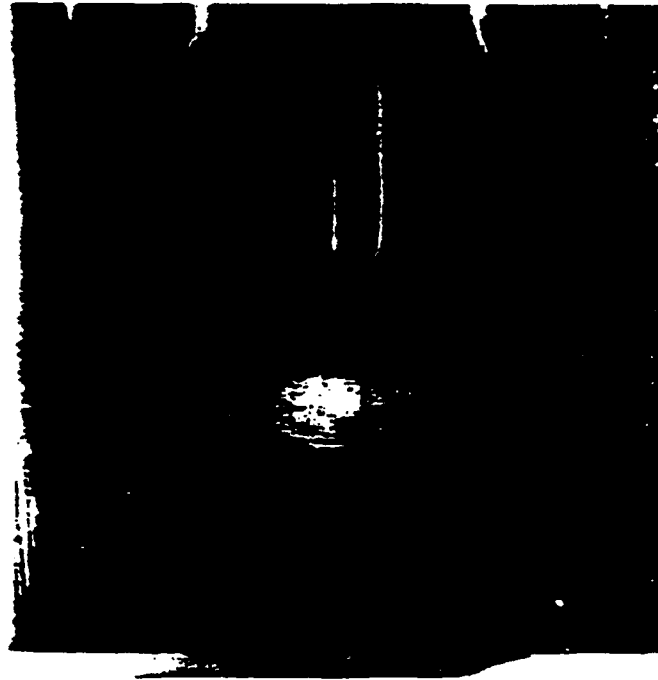
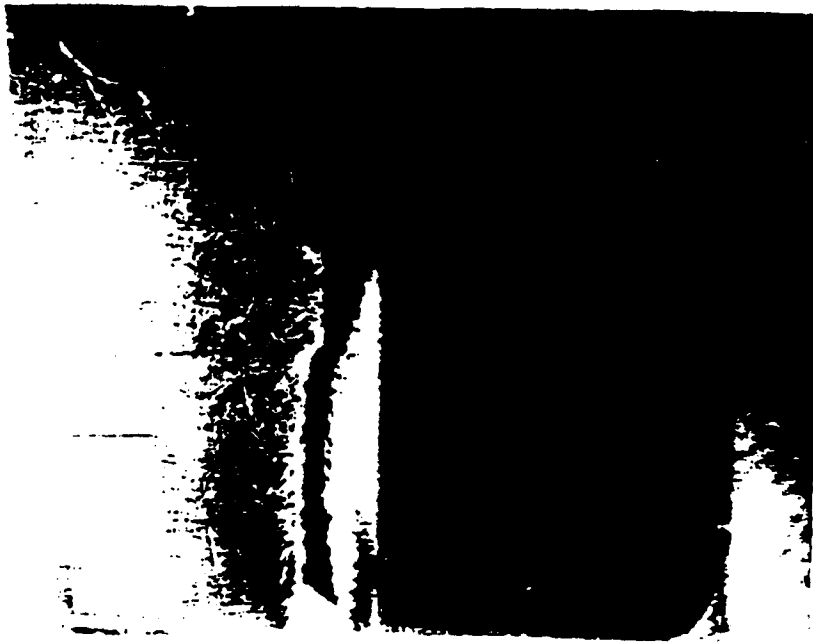


Fig. 3



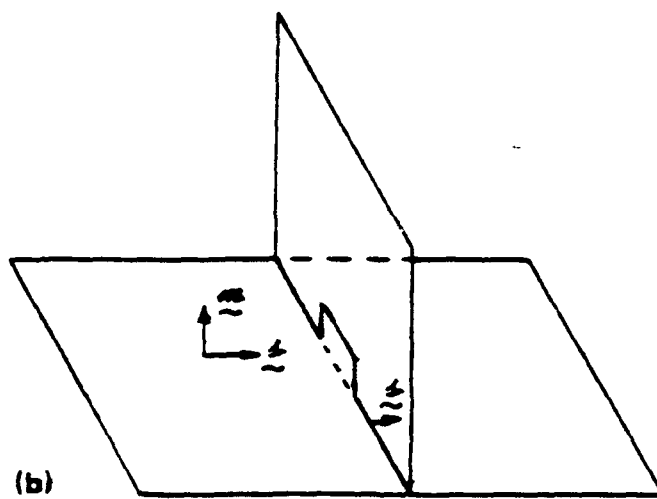
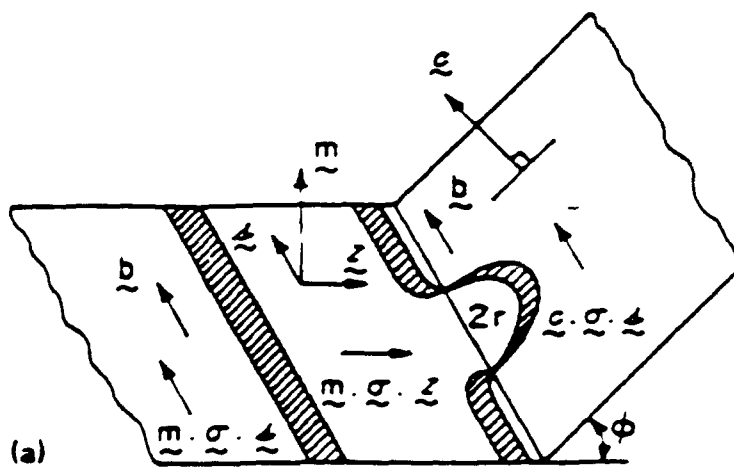


Fig. 4

UNIVERSITY COMMUNICATIONS

UCSD NEWS

Media Contact:

Warren R. Froelich, University Communications, 534-8564

Aug. 10, 1990

Robert J. Asaro Honored by Metallurgical Society

Robert J. Asaro, a professor in the Department of Applied Mechanics and Engineering Sciences (AMES) at the University of California, San Diego (UCSD), has been awarded the TMS Champion H. Mathewson Gold Medal for 1991.

The Mathewson Gold Medal is presented to an author, or authors, of a paper published in "Metallurgical Transactions," which is considered to be the most notable contribution to metallurgical science during the period under review. The award was established in 1950 to honor Dr. Champion H. Mathewson, a noted scientist and teacher.

Formal presentation of the award will be made during the annual dinner of the Minerals, Metals and Materials Society, to be held Feb. 19, 1991, at the Radisson Suite Hotel in New Orleans, La.

The Minerals, Metals and Materials Society is a member society of the American Institute of Mining, Metallurgical and Petroleum Engineers, Inc.

#####

Crack tip fields in ductile crystals

J.R. RICE,* D.E. HAWK*[†] and R.J. ASARO[‡]

**Division of Applied Sciences, Harvard University, Cambridge MA 02138, USA; Current affiliation: AT&T Bell Laboratories, Allentown, PA 18103, USA; †Department of Applied Mechanics and Engineering Sciences, University of California at San Diego, La Jolla, CA 92093, USA*

Received 1 August 1988; accepted 15 August 1988

Abstract. Results on the asymptotic analysis of crack tip fields in elastic-plastic single crystals are presented and some preliminary results of finite element solutions for cracked solids of this type are summarized. In the cases studied, involving plane strain tensile and anti-plane shear cracks in ideally plastic fcc and bcc crystals, analyzed within conventional small displacement gradient assumptions, the asymptotic analyses reveal striking discontinuous fields at the crack tip.

For the stationary crack the stress state is found to be locally uniform in each of a family of angular sectors at the crack tip, but to jump discontinuously at sector boundaries, which are also the surfaces of shear discontinuities in the displacement field. For the quasi-statically growing crack the stress state is fully continuous from one near-tip angular sector to the next, but now some of the sectors involve elastic unloading from, and reloading to, a yielded state, and shear discontinuities of the velocity field develop at sector boundaries. In an anti-plane case studied, inclusion of inertial terms for (dynamically) growing cracks restores a discontinuous stress field at the tip which moves through the material as an elastic-plastic shock wave. For high symmetry crack orientations relative to the crystal, the discontinuity surfaces are sometimes coincident with the active crystal slip planes, but as often lie perpendicular to the family of active slip planes so that the discontinuities correspond to a kinking mode of shear.

The finite element studies so far attempted, simulating the ideally plastic material model in a small displacement gradient type program, appear to be consistent with the asymptotic analyses. Small scale yielding solutions confirm the expected discontinuities, within limits of mesh resolution, of displacement for a stationary crack and of velocity for quasi-static growth. Further, the discontinuities apparently extend well into the near-tip plastic zone. A finite element formulation suitable for arbitrary deformation has been used to solve for the plane strain tension of a Taylor-hardening crystal panel containing a center crack with an initially rounded tip. This shows effects due to lattice rotation, which distinguishes the regular versus kinking shear modes of crack tip relaxation, and holds promise for exploring the mechanics of crack opening at the tip.

1. Introduction

This paper summarizes recent analytical and numerical investigations into the nature of the near-crack-tip stress and deformation fields in ductile single crystals. Ductile crystals deform plastically by the motion of dislocations on a limited set of slip systems. A continuum representation of this plastic deformation consistent with the Schmid rule, which states that flow on a system is activated when the shear stress resolved on that system reaches a critical value, is used in the analyses to be presented. This formulation leads to a yield surface in stress space consisting of planar facets joined at vertices and to an "associated" plastic straining relation.

General methods of constructing asymptotic near-tip fields for such crystals, with either stationary or quasi-statically growing cracks, have been obtained in the ideally plastic case for both anti-plane strain (mode III: [1]) and tensile plane strain (mode I: [2]) cracks. The results, as illustrated for common crack orientations in fcc and bcc crystals, lead to

striking predictions of discontinuities at the crack tip. Full scale elastic-ideally plastic solutions to the near-tip stress and deformation fields have been given for stationary cracks in the mode III study. These show that all flow is confined to planar plastic zones emanating from the crack tip, across which both displacement and stress are discontinuous. Asymptotic analysis of dynamic crack growth, i.e., including inertia, has been developed as well for that mode [3] and reveals that an elastic-plastic shock discontinuity moves along with the tip. In addition, asymptotic fields of the HRR type have been developed for stationary cracks in crystals showing Taylor hardening, with a power-law stress-strain relation at large strain, in mode III [4] and mode I [5].

The mode I asymptotic analysis [2], based on ideal plasticity and a "small displacement gradient" formulation, shows that for material at yield the stress state is constant within angular sectors whose boundaries are certain crystallographic directions on which discontinuities in either displacement (stationary crack) or velocity (quasi-statically growing crack) are possible. A direct comparison of the mode I analyses is made here with the numerical results of Hawk and Asaro [6]. When comparing different types of crystals, or crack orientations within a given crystal, the structure of the dislocations necessary to produce the same continuum field discontinuity is different. Furthermore, certain dislocations structures may induce rotation of the lattice relative to the material, thus changing the resolved shear stresses on slip systems and causing a geometric hardening or softening of the crystal. This is important particularly when large deformations are taken into account.

Recently, full scale elastic-plastic solutions for mode I cracks in ductile crystals have been obtained numerically by the detailed finite element analyses of Hawk and Asaro [6]. Some of their results are briefly summarized here for several different loading cases. These analyses model the constitutive behavior of the crystal with a visco-plastic formulation in the nearly rate-independent limit. The numerical analysis of Asaro [6] models from small-scale to general yielding a center cracked panel with a blunted crack tip under uni-axial tension. The slip systems of the crystal are idealized by a planar double-slip model. The effect of Taylor type hardening of the slip systems and large displacement gradients (e.g., lattice rotation) are included. In the small-scale-yielding analysis of Hawk [6], both a stationary and quasi-statically propagating perfectly sharp tensile crack are simulated. The crystal is modeled as elastic-ideally plastic using a complete description of the slip systems in a fcc crystal. Small displacement gradients are assumed.

2. Constitutive law

The crystals considered can undergo both elastic and plastic deformation. The plastic deformation is consistent with a continuum description of single crystals [7-10]. The total strain-rate is taken as the sum of the elastic strain-rate and plastic strain-rate

$$\dot{\epsilon}_{ij} = \dot{\epsilon}_{ij}^e + \dot{\epsilon}_{ij}^p \quad (1)$$

Under plane strain conditions, which are possible for the high-symmetry crack orientations considered here, $\dot{\epsilon}_{13}$, $\dot{\epsilon}_{23}$, $\dot{\epsilon}_{33}$, σ_{23} are zero. The plastic deformation of the crystal occurs by the motion of dislocations along certain preferential crystallographic planes. The movement of these dislocations causes a permanent dilationless straining of the crystal. A slip

system denoted by α is defined by two unit vectors giving the slip direction $\mathbf{s}^{(\alpha)}$ and the normal to the slip plane $\mathbf{n}^{(\alpha)}$. The parameter $\gamma^{(\alpha)}$ describes the amount of shear strain on each slip system. These preferential slip systems defined by $\mathbf{s}^{(\alpha)}$ and $\mathbf{n}^{(\alpha)}$ vary according to the crystal structure (e.g., face centered cubic, f.c.c. or body centered cubic, b.c.c.). It is possible to express the plastic strain rate as a sum over all the N slip systems of the crystal as

$$\dot{\epsilon}_{ij}^p = \sum_{\alpha=1}^N \mu_{ij}^{(\alpha)} \dot{\gamma}^{(\alpha)} \quad (2)$$

Here $\mu_{ij}^{(\alpha)}$ is termed the Schmid factor and is determined from the slip direction $\mathbf{s}^{(\alpha)}$ and the normal to the slip plane $\mathbf{n}^{(\alpha)}$ as

$$\mu_{ij}^{(\alpha)} = \frac{1}{2} (s_i^{(\alpha)} n_j^{(\alpha)} + s_j^{(\alpha)} n_i^{(\alpha)}) \quad (3)$$

The resolved shear stress, $\tau^{(\alpha)}$, on a system is expressible in terms of these Schmid factors as

$$\tau^{(\alpha)} = \sigma_{ij} \mu_{ij}^{(\alpha)} \quad (4)$$

The plastic deformation of a crystal is said to obey the Schmid rule if the instantaneous shear response $\dot{\gamma}^{(\alpha)}$ of any given system α depends on the current stress state only through the combination in (4). In a time-independent plasticity formulation, a necessary but not sufficient condition for slip to occur is that the resolved shear stress $\tau^{(\alpha)}$ reaches a critical value $g^{(\alpha)}$. This criteria results in a yield surface in stress space which consists of planar facets that join at vertices at which two or more systems are simultaneously active. Equation (2) then assures that the flow rule is of an "associated" type. Rice [11] showed that for rigid-plastic incompressible solids of this class in plane flow, the yield surface can be represented as a curve in the reduced stress space of $(\sigma_{11} - \sigma_{22})/2$ and σ_{12} . Such a yield surface is schematically shown in Fig. 1 and for crystals as described here, it is polygonal. In an elastic-plastic

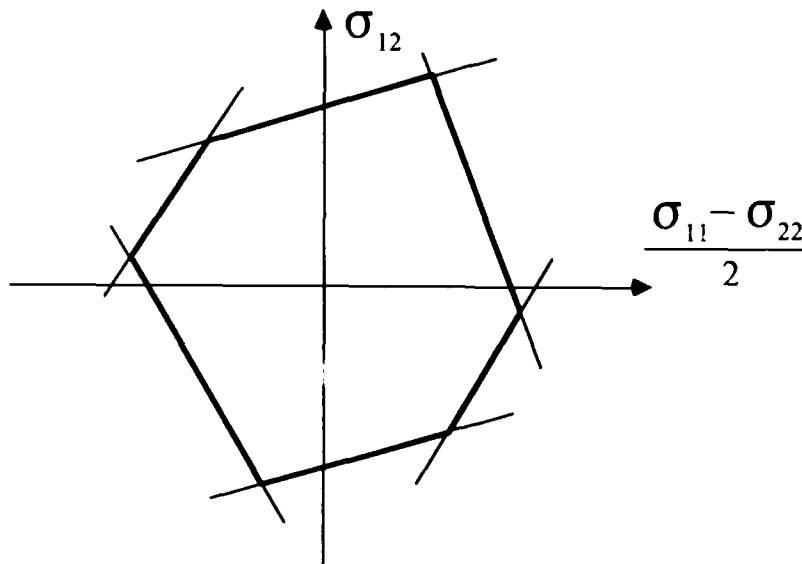


Fig. 1. Schematic of yield surface for a ductile crystal undergoing plane straining.

material the same result applies for stress states in large sustained plastic strain. However, in such a case limited deformation may occur on slip systems corresponding to segments of the yield surface sensitive to the value of $(\sigma_{11} + \sigma_{22})$ but which cannot produce sustained plane flow. We will term the sides of the polygon as "flats" and the point of junction of two sides as a "vertex". The flow law of (2) being associative, the direction of plastic straining, with components $(\dot{\epsilon}_{11}^p - \dot{\epsilon}_{11}^e)/2$ and $\dot{\epsilon}_{12}^p$, is normal to the yield surface on a "flat" and within the forward fan of normals at a "vertex".

It will also be convenient to represent the slip systems of the crystal as traces in the x_1, x_2 plane. For example, in Fig. 2a, a unit cube representing the lattice of an fcc crystal is shown. The slip planes of a fcc crystal are the $\{111\}$ planes indicated by the various shaded planes in the cube. The slip directions are $\langle 101 \rangle$ directions which are the diagonals of the cube faces. If the crack lies in the plane (010) and the crack tip lies along the diagonal of the cube face as indicated, then the traces of the slip systems (i.e. intersection of the slip planes with the x_1, x_2 plane) are as indicated in Fig. 2b. It is then possible to represent the slip direction s and slip plane normal n as the directions S and N respectively in the x_1, x_2 plane as shown in the figure. Only those traces shown correspond to systems which can produce sustained

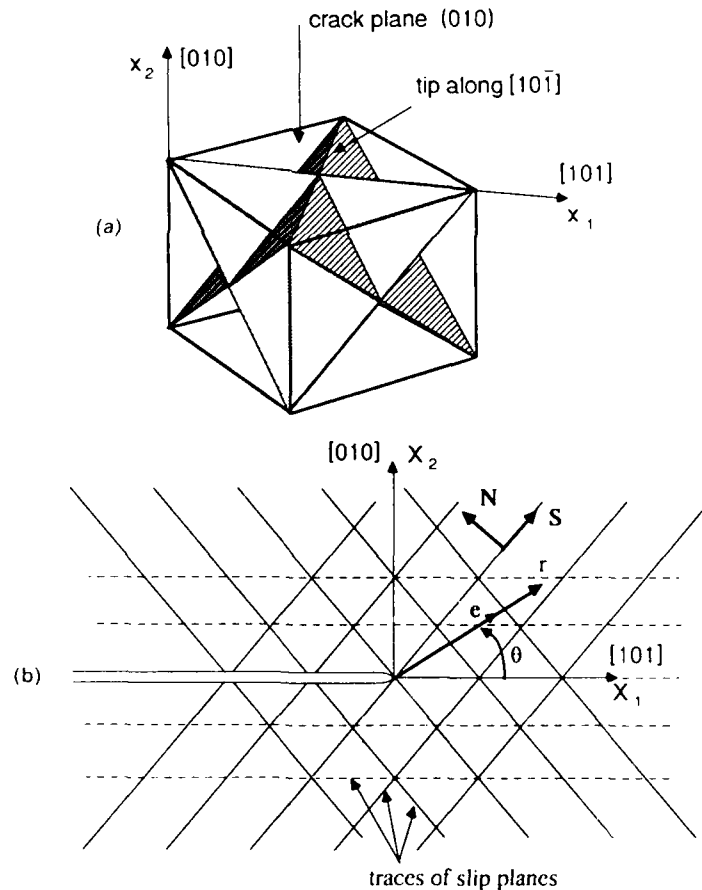


Fig. 2. (a) Face centered cubic slip systems, and orientation of the crack plane and crack tip for case illustrated below. (b) Crack on (010) plane growing in $[101]$ direction. Traces are shown of those slip plane families which can accommodate sustained plane straining.

plane flow. The solid line traces correspond to individual $\{111\}$ planes, and the dashed lines to two such planes which intersect along a $\langle 110 \rangle$ slip direction common for each and which, by equal coincident slip, produce plane flow.

The finite element analyses use a visco-plastic formulation where slip can occur on any system so long as resolved shear stress on that system is non-zero. A simple power-law relation [12-14] can be used to describe the rate of slip on each system as

$$\dot{\gamma}^{(n)} = \dot{\gamma}_0^{(n)} \operatorname{sgn}(\tau^{(n)}) \left(\left| \frac{\tau^{(n)}}{g^{(n)}} \right| \right)^{1/m} \quad (5)$$

As the exponent $m \rightarrow 0$ the visco-plastic model approaches the rate-independent formulation. Use of a visco-plastic law in a finite element formulation, pioneered in the work of Pierce et al. [14], eliminates certain problems of uniqueness and considerations of when a point is at yield. The $g^{(n)}$ reflects the current level of strain hardening in the crystal. In [6], results are presented for both ideal plasticity i.e., $g^{(n)}$ is a constant, τ_0 , and cases where $g^{(n)}$ is a function of the sum of the magnitudes of the slips ($\Gamma = \sum_n |\dot{\gamma}^{(n)}|$), which coincides with Taylor hardening.

3. Asymptotic analysis

The asymptotic analyses (e.g., $\lim_{r \rightarrow 0} \sigma_{\alpha\beta}(r, \theta, t)$) of Rice [2] are summarized here for the case of ideal plasticity in a "small displacement gradient" formulation of the mode I problem. Based on the equations of equilibrium with a bounded crack tip stress state and with the further condition that the stress state is at yield relative to a slip plane trace in the direction S_x , the following requirement is found:

$$(N_x e_x)(S_x e_x)(\sigma'_{11} + \sigma'_{22}) = 0 \quad (6)$$

Greek indices range from 1 to 2. As indicated, Fig. 2b, the e_x are the components of the radial unit vector in the x_1, x_2 plane; $(e_1, e_2) = (\cos \theta, \sin \theta)$. The terms S_x and N_x are the components of the traces of the slip direction and slip plane normal as previously defined. The $\sigma'_{\alpha\beta}$ denote

$$\sigma'_{\alpha\beta} = \lim_{r \rightarrow 0} \frac{\partial \sigma_{\alpha\beta}(r, \theta)}{\partial \theta} \quad (7)$$

Equation (6) implies $\sigma'_{11} + \sigma'_{22} = 0$ for all θ except for four special values when \mathbf{e} is aligned with either \mathbf{N} or \mathbf{S} . Based on the form of the stresses consistent with equilibrium for material at yield, this statement further implies that within sectors bounded by these four special values of θ , all $\sigma'_{\alpha\beta}$ are zero; i.e. the stress state is independent of θ . For a tensile crack it is shown that, in order to meet boundary conditions, either (i) the stresses in certain angular sectors around the crack tip are not at yield or (ii) that the stresses change discontinuously at the special values of θ as mentioned above.

3.1. Stationary crack

For the stationary crack, as $r \rightarrow 0$, the yield condition can be met in all angular sectors around the crack tip, thus requiring discontinuous jumps in the stress state. The stress discontinuity must be from one point on the yield surface to another, and considering the nature of restrictions on such discontinuities, this path must be a straight line in the stress space and the line must lie everywhere along the yield locus (and hence correspond to a flat segment in Fig. 1) since otherwise elastic unloading would occur. The solution which satisfies the jump conditions for the stress discontinuity is one where the stress state changes from vertex to vertex on the yield surface. The deformation fields, consistent with the above stress state, must have a shear type of discontinuity in the displacement field along the same direction, \mathbf{e} , for which the stress is discontinuous. These correspond to concentrated shear parallel to the slip plane traces when \mathbf{e} is aligned with \mathbf{S} , and to kink-like shear perpendicular to the traces when \mathbf{e} is aligned with \mathbf{N} . The specifics of constructing such solutions may be found in [2]. Specific examples of these solutions will be given in the discussion of the finite element solutions of [6].

3.2. Growing crack

For the quasi-statically growing crack, Drugan and Rice [15] demonstrated for this type of material that discontinuities in stresses and displacements cannot exist. However, it is possible to have velocity discontinuities. It is therefore necessary to have bordering on the plastic sectors angular sectors in which elastic unloading (and perhaps reloading) occur. Construction of the solution for a particular crystal orientation, again for which the details are given in [2], shows a complicated pattern of plastic sectors and elastic unloading and reloading sectors is necessary to model the crack tip fields for quasi-static growth. A specific example will be presented for comparison with the finite element solutions of Hawk [6] in the next section which shows that one of the physically active system for the stationary crack becomes inactive in the growing case.

3.3. Note on role of \mathbf{S} and \mathbf{N}

In the asymptotic analyses presented, based on the "small displacement gradient" formulation, the role of the slip direction \mathbf{S} and slip plane normal \mathbf{N} are interchangeable since they come in through the symmetric form of (3). In certain cases [2] fcc crystals and bcc crystals differ only by an interchange of \mathbf{S} and \mathbf{N} . Therefore solutions obtained for such fcc crystals are also valid for bcc crystals as well (aside from a slight scaling). However, the structure of the actual dislocations necessary to produce the shear deformation is quite different when \mathbf{S} and \mathbf{N} are reversed. For example, shown in Fig. 3a and 3b is shear parallel to the slip planes and shear perpendicular to the slip planes respectively. The motion indicated in Fig. 3a can be generated by the emission of dislocations from the crack tip along the slip direction as shown in Fig. 3c. Notice however that in Figure 3b the slip planes must form a kink in order to accommodate the deformation. Experiments in Fe-3% Si crystals [16] show results consistent with kink-like shear. This kink requires dislocation dipoles as in Fig. 3d. These dipole loops, illustrated as pairs of dislocations, cannot be swept out from the crack tip and

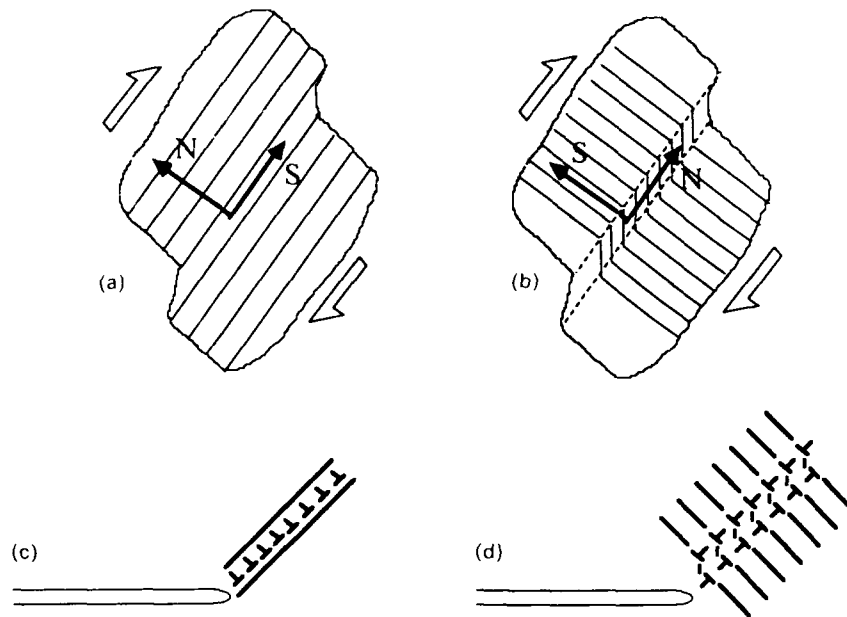


Fig. 3. (a) Shear in band lying parallel to the active slip systems. (b) Shear by a kinking mode in a band lying perpendicular to the active system. (c) Dislocations can be generated at the crack tip and swept out along slip planes, or can be generated from internal sources, to produce the slip-plane-parallel shear band of (a). (d) Dislocations dipole loops must be nucleated from internal sources and expand as illustrated to produce the kinking shear band of (b).

must therefore depend on the availability of internal sources to produce them. Requiring the availability of internal sources, as opposed to allowing dislocations to be swept out from the crack tip along slip planes, may influence whether the fracture of a particular crystal is brittle or ductile. It is seen also that the lattice between the pair of dislocations in Fig. 3d is apparently rotated. This can cause either a geometric hardening or softening of the material because the resolved shear stress $\tau^{(s)}$ on each slip system varies as the Schmid factor, $\mu_{ij}^{(s)}$, changes due to rotation of **S** and **N** directions. The effect of such lattice rotation will be seen later in the large deformation results of Asaro [6].

3.4. Some further analyses of mode III cracks

The analyses discussed so far have been for tensile cracks, which is the physically more interesting case. However they are approximate in that their validity is only in the limit as $r \rightarrow 0$. The simpler nature of the equations for mode III (anti-plane strain) type loading allows for more complete solutions [1, 3] which we briefly summarize here. Three such solutions are shown in Fig. 4 exclusively for the fcc crystal with the orientation of the crack the same as in Fig. 2a with the crack along the (010) plane with crack tip along the $[10\bar{1}]$ direction. Under mode III loading conditions the only non-zero displacement is $u_3(x_1, x_2)$ which gives rise to only two non-zero stress components σ_{31} and σ_{32} . In this case only the solid-line slip plane traces in Fig. 2b can provide anti-plane straining. The yield surface can thus be represented in σ_{31}, σ_{32} stress space and for this orientation is diamond

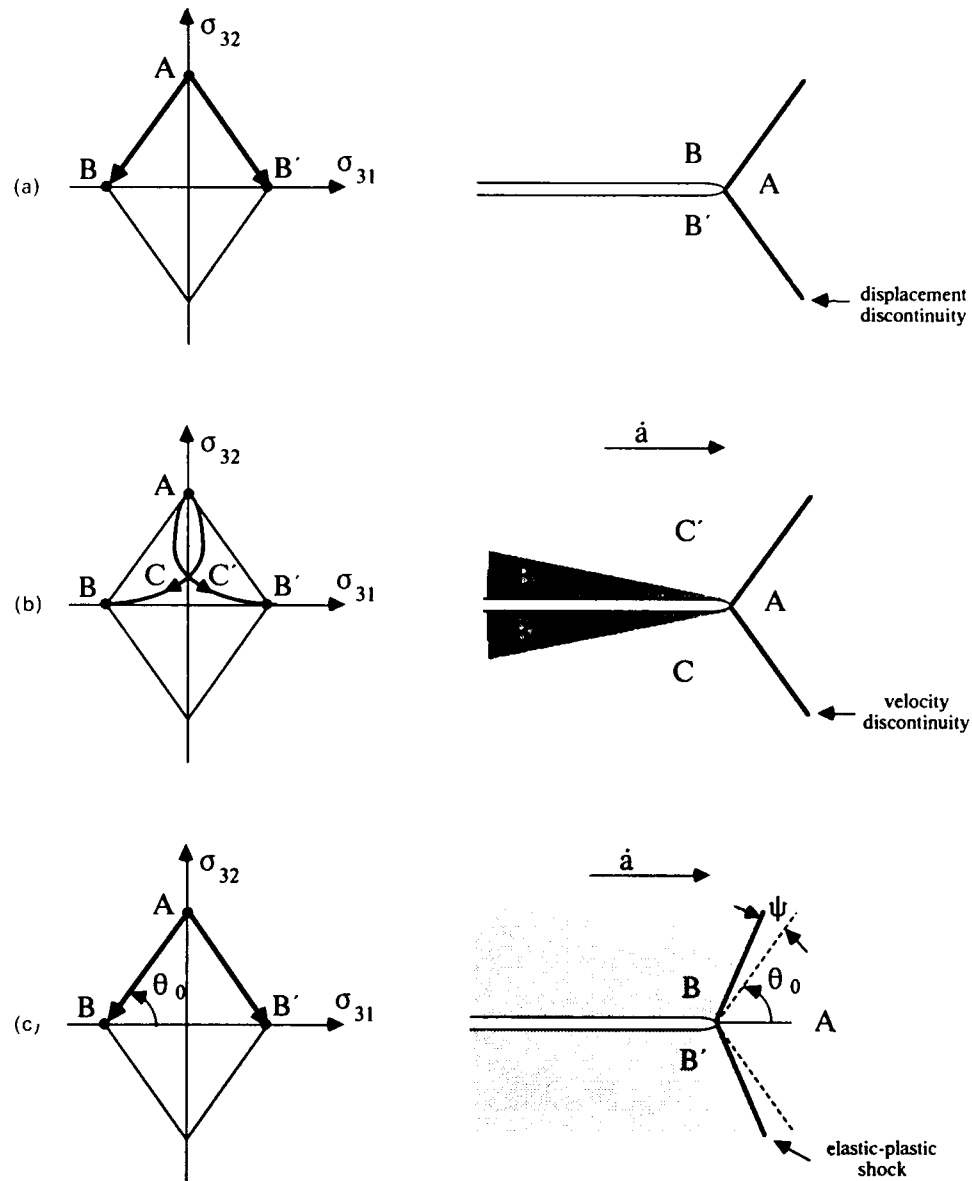


Fig. 4. Summary of analyses for anti-plane shear of a cracked ideally plastic crystal: (a) Stationary crack; (b) Quasi-static crack growth; (c) Dynamic crack growth asymptotic field (inertial effects included).

shaped. The assembled stress sectors for these solutions will be labeled with A , B , etc. with corresponding points or trajectories labeled on the yield surface. As is often the case, similar features are seen to carry over from the mode III solution to the mode I solution.

The stationary case is shown in Fig. 4a with the corresponding yield surface and stress trajectories as indicated. Only two sectors A , B in the upper half plane (a corresponding sector to B labeled B' is shown in the lower half plane) of the constant stress type, as previously discussed for plane strain in the asymptotic limit as $r \rightarrow 0$, are necessary to construct the full solution. Both of the corresponding stress points are on the yield surface

as indicated. These sectors are separated by a line of discontinuity in both displacement and stress. The stress discontinuity can be thought of as a rapid transition (in a vanishing small sector) from point A to point B as indicated by the arrow on the yield surface. The complete solution of Rice and Nikolic [1] shows that these sectors are actually elastic with all plasticity collapsed into a shear zone along the line of the displacement discontinuity. The size of this plastic zone is found exactly in their analysis.

The quasi-static crack growth case is shown in Fig. 4b. Three sectors A , B' and C'' in the upper half plane (with corresponding sectors B and C in the lower half plane) are necessary to assemble the solution. Sector A is of the constant stress type with the state of stress at the yield surface as indicated on the yield surface plot. As necessary from the asymptotic solution this sector is bounded by an elastic sector C'' . Sector A is separated from C'' by a velocity discontinuity (expected to extend over a finite size region based on the approximate analysis of Rice and Nikolic [1]) along which all the plastic flow takes place in the region forward of the crack tip. As shown by the lightly shaded region in Fig. 4b, as the crack grows this velocity discontinuity also leaves behind a wake of plastic deformation. Sector C'' , as indicated by the corresponding path within the yield surface, unloads elastically and reloads to yield by the time it reaches the other plastic sector B' creating a thin wedge of plastic deformation along the crack face, shown in darker shading. The exact details of the construction of the angles for these sectors is presented in [1].

Finally, the case of dynamic crack growth where the effects of inertia are taken into account is shown in Fig. 4c [3]. In this case the entire field consists of constant stress sectors separated by an elastic-plastic shock (possible only in single-crystal-like materials with flat segments along their yield locus). Both velocity and stress are discontinuous across the shock. Remarkably, the strain accumulated in crossing the shock is finite at the crack tip. It is of the order of the strain at first yield divided by the elastic Mach number associated with the crack speed. The angle ψ , in Fig. 4c, is proportional to the Mach number at low speed and approaches $(\pi - \theta_0)/2$ at the sonic speed. There must be a complicated transition between the near tip field with the inertia included, Fig. 4c, and that without Fig. 4b. This is an example of nonuniform asymptotic limits as one considers $r \rightarrow 0$ and $\sqrt{\rho v^2/G} \rightarrow 0$ where ρ is the density, G is the shear modulus and v is the crack speed. E.g., the quasi-static growth case may be considered as letting $\rho \rightarrow 0$, or $v \rightarrow 0^+$, before letting $r \rightarrow 0$.

4. Comparison of asymptotic and numerical analyses for mode I

4.1. Small-scale-yielding results

Under small-scale-yielding conditions, a stationary and quasi-statically propagating plane strain mode I crack in a fcc crystal has been investigated by the finite element analysis of Hawk [6]. The material is elastic-ideally plastic, modeled by a visco-plastic formulation as in (5), with $g^{(1)} = \tau_0$ and $m = 0.005$. Small-scale-yielding conditions exist when the size of the plastic zone is much smaller than the region over which the elastic singular stress field dominates. The dominance of the elastic singularity allows the crack tip region to be modeled as an infinite solid with a semi-infinite crack where the stresses approach those of the elastic singularity as $r \rightarrow \infty$. The finite element mesh of both analyses is shown in Fig. 5. Since the mode I problem is symmetric, only the upper half plane is modeled. The finite element mesh

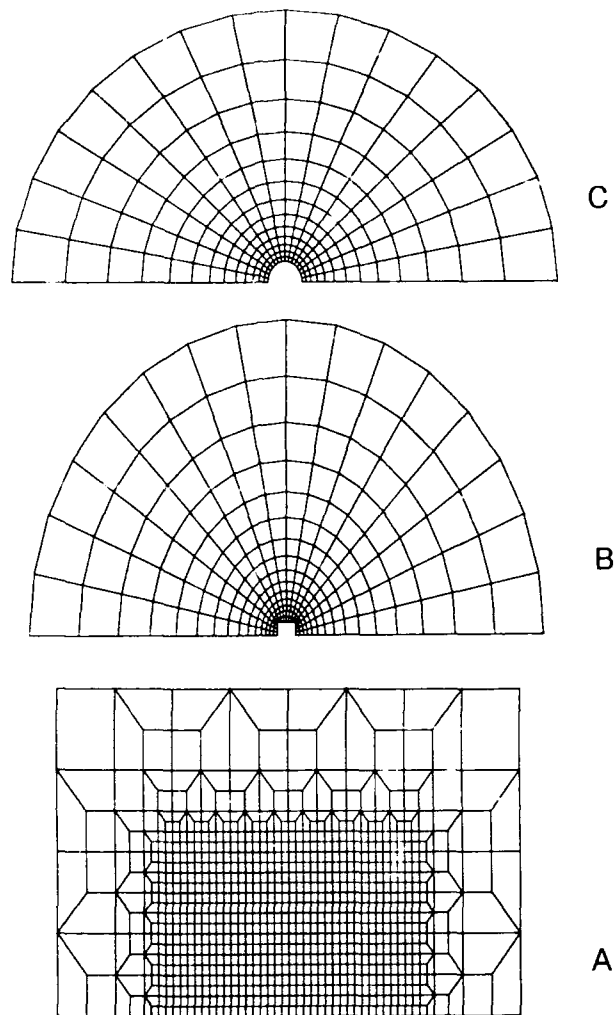


Fig. 5. Finite element mesh for "small displacement gradient" analysis of small-scale yielding in an ideally plastic crystal.

is shown in three sections A, B and C for clarity. Section A fits into the rectangular space of section B and section B in turn fits into the space in section C. The ratio of the size of the smallest rectangular element of region A to the outermost radius of region C is approximately 10^{-4} . Each quadrilateral element is actually a so called cross triangle element [17] made up of four constant-strain triangles (formed from the diagonals of the element) which as a group behave well under incompressible conditions. The crack opens to the left with nodes ahead of the crack tip constrained from vertical movement by the symmetry boundary condition. Traction corresponding to the elastic K field singularity are applied to the outer boundary of section C. The results are primarily from section A and the region immediately surrounding it. The details of the finite element method are presented in [6].

The analysis of the stationary crack in an fcc crystal was performed with the orientation of the crack the same as shown in Fig. 2a. The crack lies in the (010) plane with the crack tip along the $[10\bar{1}]$ direction. Elasticity was modeled as isotropic. The yield surface

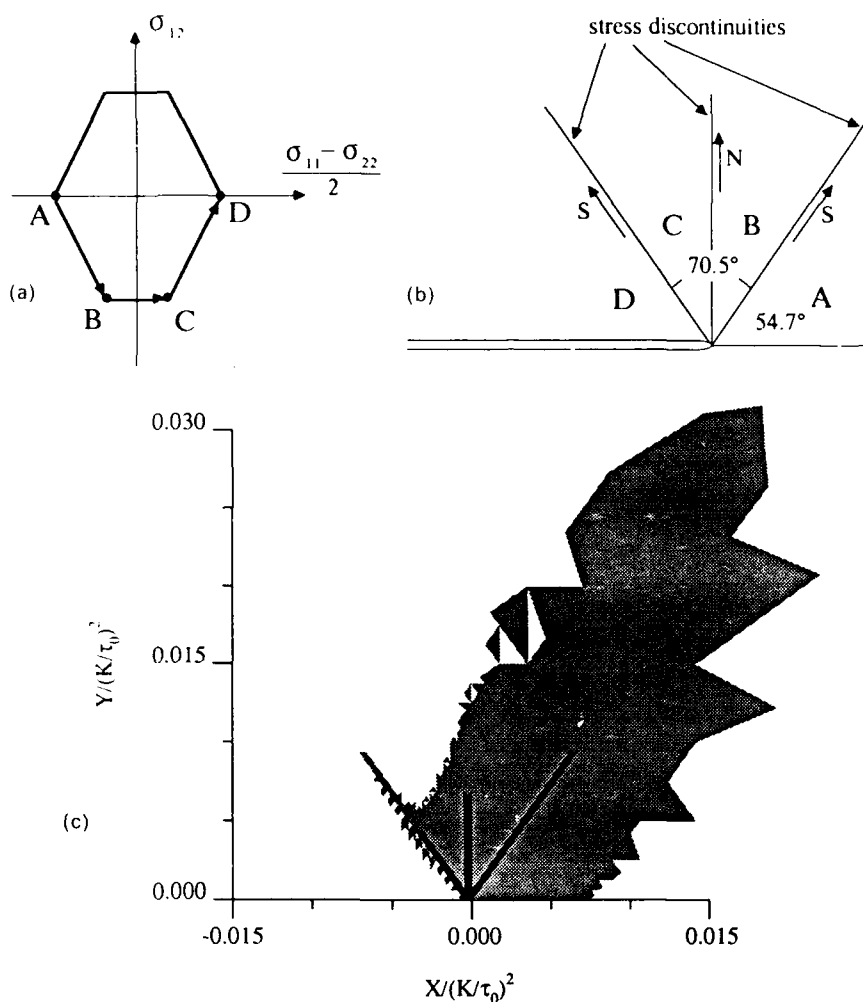


Fig. 6. Stationary crack in ideally plastic crystal of Fig. 2: (a) Yield surface; (b) Asymptotic structure of crack tip field; (c) Finite element results: grey zone with $\Gamma \geq 0.01$ ($\tau_0 G$) essentially denotes plastic zone; black zone with $\Gamma \geq 10$ ($\tau_0 G$) shows zone of more concentrated plastic strain.

(appropriate to sustained flow) for this orientation is shown in Fig. 6a. The asymptotic solution obtained by Rice [2] for the stationary crack case is shown in Fig. 6b. In the stationary case, the entire crack tip region may deform plastically. For the upper half plane, the solution consists of four constant stress sectors labeled A, B, C, and D separated by stress and displacement discontinuities as indicated in Fig. 6b. The stress state of each sector is similarly labeled as points on the yield surface A, B, C and D in Fig. 6a. The discontinuity between A and B at 54.7° and the one between C and D at 125.3° correspond to the slip directions for the solid traces in Fig. 2b. The discontinuity between sectors B and C corresponds to the normal of the slip plane indicated by the dashed traces in Fig. 2b. Each discontinuity in stress represents a rapid transition from point to point on the yield surface as shown by the arrows.

Let the sum over the slip systems of the magnitude of slip, $\sum_i |\gamma_i^{(n)}|$ be denoted as Γ . This quantity is an overall measure of the amount of plastic straining and is shown in Fig. 6c

normalized by the elastic strain at yield, τ_0/G . The grey zone, formed by shading individual triangular elements whose value of $\Gamma/(\tau_0/G)$ is between 0.01 and 10, is representative of the overall plastic zone shape. The black bands are those elements whose value of Γ is greater than 10. Therefore, the most intense straining is along the predicted discontinuities of the asymptotic solution. It is interesting to note that all the sectors are predicted to be stressed to yield as $r \rightarrow 0$, but only the interfaces between them are proven to be deforming plastically in the asymptotics. The finite element solution indicates that sector D bounding the crack face is relatively free of plastic deformation while the others deform. Some plastic strain

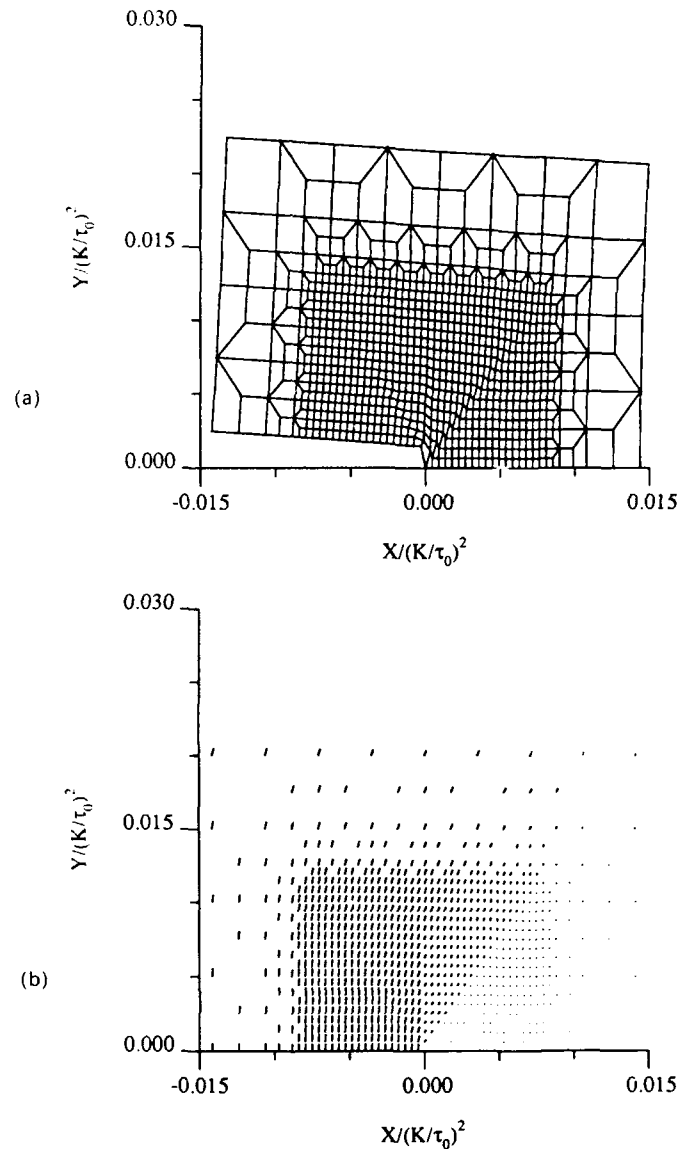


Fig. 7. (a) Deformed mesh for stationary crack (factor of 50 amplification of displacements); note shear zones coincident with directions shown in Fig. 6(b). (b) Line lengths proportional to displacements accumulated in a load increment; suggests that displacement discontinuities predicted by asymptotic analysis extend well into plastic zone.

ahead of the crack occurs on slip systems other than those of Fig. 2b, i.e., on systems which cannot undergo sustained plane flow. The deformation of the finite element mesh around the crack tip is shown in Fig. 7a with the displacements magnified by a factor of 50. The most intense deformation is in those elements which lie along the discontinuity between sectors A and B. The increment of displacement, scaled up for visibility, over a load increment is shown in Fig. 7b. Four distinct sectors exist with the motion in each sector fairly uniform. This indicates the majority of deformation is caused by the movement of nodes near the predicted discontinuities.

A quasi-statically propagating crack in a fcc crystal is simulated using a node release technique the details of which are given in [6]. The crack propagates to the right through 9 elements under constant load from an initial stationary position to the center of section A in Fig. 5. The same orientation of the crack with respect to the crystal is used in the propagating crack case as in the stationary crack case above. The yield surface for this orientation is repeated in Fig. 8a for reference. As discussed in the previous section on

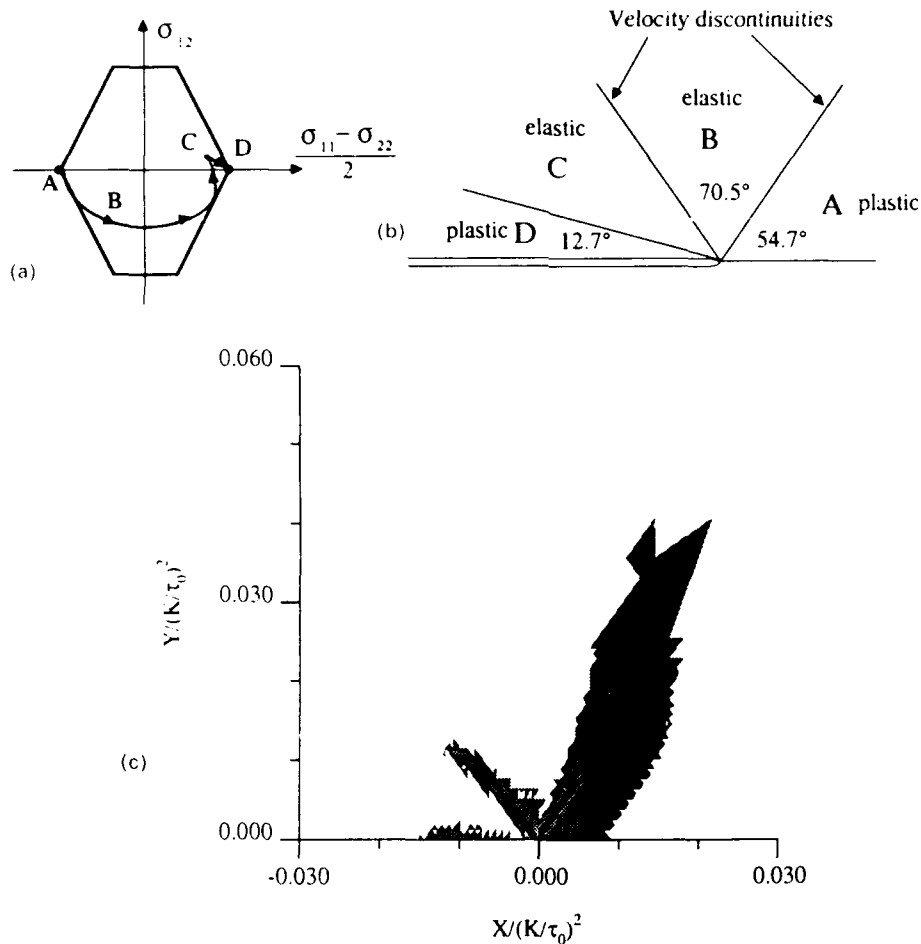


Fig. 8. Quasi-statically growing crack in ideally plastic crystal of Fig. 2: (a) Yield surface and stress trajectory. (b) Asymptotic structure of near tip field. (c) Finite element results showing plastic activity, as measured by increment of Γ , during one finite element step of crack growth. Grey zone corresponds essentially with plastically active zone during growth; black zone has more concentrated plastic straining.

asymptotic solutions, neither stress nor displacement discontinuities may exist and if a sector is plastic it must border an elastic sector. The assembly of sectors for this orientation [2] is shown in Fig. 8b. For the upper half plane, the solution again consists of four sectors labeled A, B, C, and D. Sector A is a constant stress plastic sector and it is separated from an elastic sector B by a discontinuity in velocity at 54.7° . As indicated by the stress trajectory in Fig. 8a, sector B involves an elastic unloading and reloading back to yield by the time a second velocity discontinuity is reached at 125.3° . Sector C is another elastic unloading and reloading sector. Finally, sector D is plastic.

The crack leaves behind a wake of plastic deformation which makes the quantity Γ not as illustrative as it had been in the stationary crack case. The increment in Γ (τ_0, G) ($= \Delta\Gamma(\tau_0, G)$) from just before the last node release to just after it, is shown in Fig. 8c, which eliminates much of the accumulated plastic wake and shows only the regions which are plastically active during growth. Elements which sustained $\Delta\Gamma(\tau_0, G)$ between 0.001 to 1 are shaded gray and those with increments greater than 1 are in shaded black. There are very striking similarities between the predicted asymptotic solution, Fig. 8b, and the finite element solution, Fig. 8c. Sector A is plastic and is bounded by an intense band of plastic deformation along the predicted velocity discontinuity. Sector B is relatively free of plastic deformation as predicted. At the second velocity discontinuity at 125.3° where the predicted stress trajectory is tangent to the yield surface an intense band of plastic deformation is encountered. Subsequently, an elastic sector roughly similar in angular extent to sector C is seen in the finite element solution. Finally, elements along the crack faces are loading plastically. The deformed mesh after the crack growth has taken place is shown in Fig. 9a. It is interesting to note that while the crack was stationary (as load was increased) the solution was the same as in Fig. 7a, as shown by the distinct kink in the crack profile at the crack's initial position. However, once crack growth began and a displacement discontinuity was no longer allowed the crack profile was smooth. The increment in nodal displacements, again scaled up for visibility, from just before the final crack growth increment to just after is shown in Fig. 9b. Two rather distinct bands of discontinuity are seen close to the crack tip corresponding to the lines of the velocity discontinuities. The smooth change of direction of the increments directly above the crack clearly indicates that the discontinuity seen at 90° in the stationary case is no longer present in the growing crack case.

4.2. Center crack panel results

A square, center cracked panel under plane strain conditions has been modeled from small-scale-yielding to general yielding in the finite element analyses of Asaro [6]. Three sections of the finite element mesh are shown in Fig. 10. Section A is imbedded in the dense part of section B which is in turn imbedded in the densest part of section C. Section C is then extended outwards in a similar pattern to slightly more than 20 times the size shown, with the outer boundaries of successive "rings" of elements forming two adjacent sides of a succession of squares. Symmetry reduces the analysis to just that of one quarter of the specimen, represented by section C as extended to a large square with sides of dimension b . The total length of the crack is $2a$ with the ratio of a/b equal to 0.01. The ratio of the size of elements in section A to the size of the elements in the outermost mesh is approximately 2×10^{-4} . The crack tip is initially rounded as we can see from the mesh in section A. Stresses

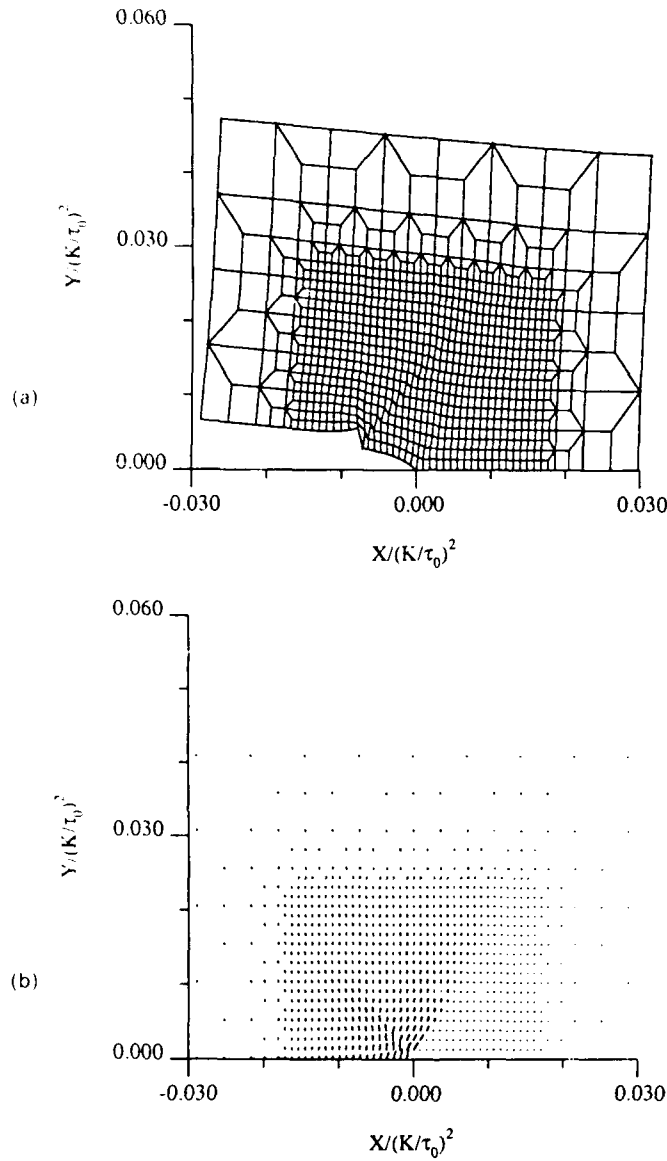


Fig. 9. (a) Deformed mesh (factor of 100 amplification) after several steps of crack growth at constant far-field stress intensity K_I . (b) Line lengths proportional to displacement increments during crack growth over one finite element step of crack growth. Suggests that velocity discontinuities predicted by asymptotic analysis extend well into the plastic zone.

corresponding to uniform tension σ' perpendicular to the crack are applied to the outer boundary.

Finite rotations of both material and the crystal lattice are taken into account in this work. The computational procedures used in the finite element calculations follow the initial work of [14] and [18]. The elements used are the same cross triangle type [17] discussed in conjunction with the small scale-yielding analysis. The plasticity is modeled by a visco-plastic formulation with the slip rate on each system as given by (5) with $m = 0.005$. A Taylor type

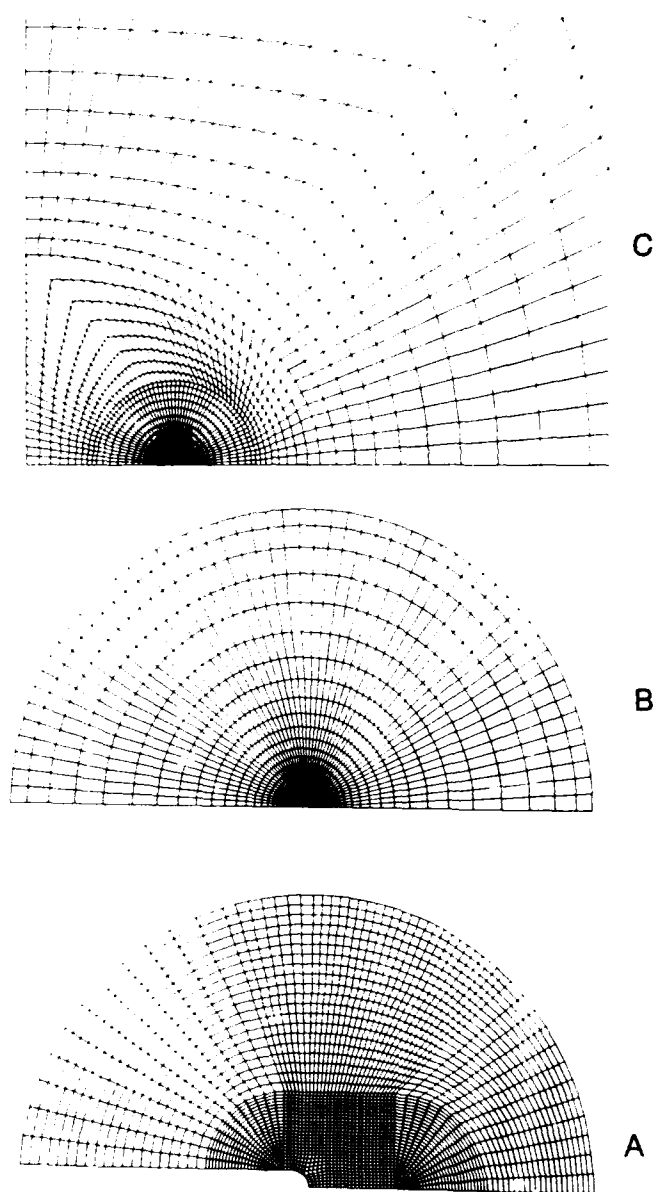


Fig. 10. Finite element mesh for analysis of tensile load of a panel containing a center crack with initially rounded tip. Used for crystal models with double slip, as in insets of Figs. 11(a) and (b). Strain hardening and arbitrary displacement gradients are included in the analysis.

of hardening of slip systems is included with $g^{(s)}$ a function of $\Gamma = \sum_s |\dot{\gamma}^{(s)}|$,

$$g^{(s)} = g_0 [1 + 0.8 \tanh (11.1 \Gamma)] \quad (8)$$

where $g_0/G = 0.0026$.

The crystal is idealized by a planar double slip model for two orientations of the crack as shown by the insets of Fig. 11a and 11b. The first orientation corresponds to that in Fig. 2b

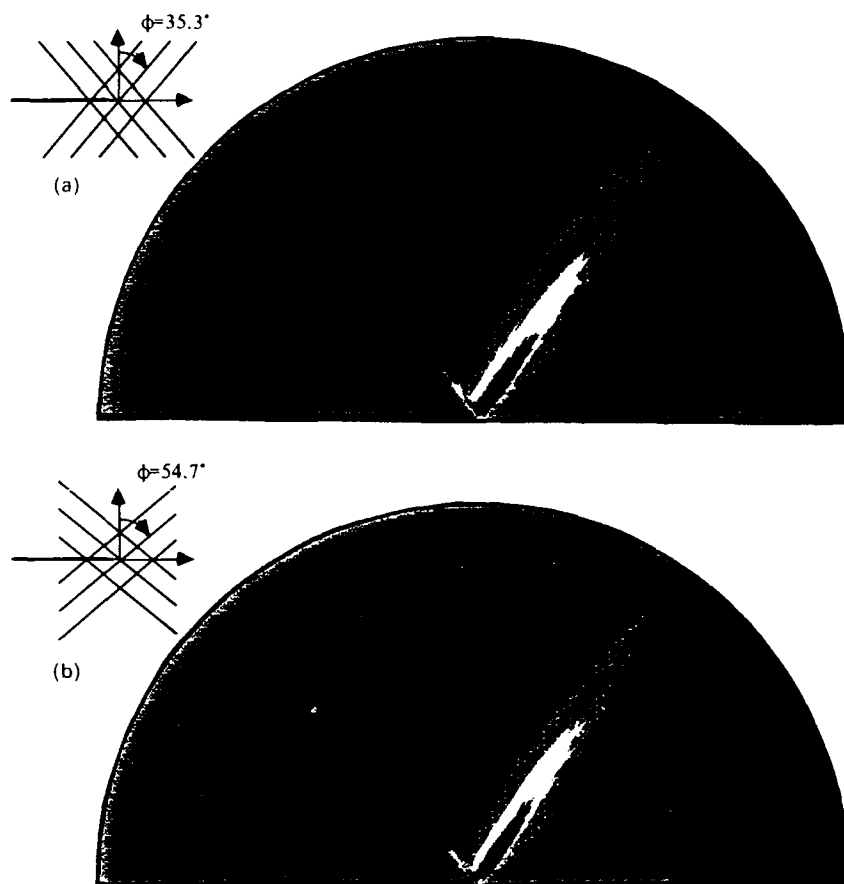


Fig. 11. Contours of equivalent shear strain Γ near the tip; outermost is $\Gamma = 0.005$, next is $\Gamma = 0.01$ and innermost is $\Gamma = 0.02$: (a) For 35.3° angle between slip planes and tensile direction; (b) For 54.7° angle.

for a fcc crystal, *i.e.*, a (010) crack growing in the $[101]$ direction, when we neglect the slip plane traces shown as the dashed lines. It also corresponds to a bcc crystal with the crack on the (101) plane growing in the $[010]$ direction when we similarly neglect certain slip plane traces parallel to the crack. The angle between the x_2 axis and the traces of the slip direction S , denoted by ϕ , is equal to 35.3° in this case. The second orientation has $\phi = 54.7^\circ$. It corresponds, with neglect of certain systems as above, to a crack lying on the (101) plane growing in the direction $[010]$ in a fcc crystal, or to a crack on the (010) plane growing in the $[101]$ direction in a bcc crystal. See [2] for fuller discussion of yield surfaces in these cases. These orientations with only the slip systems indicated correspond to a diamond shaped yield surface, *e.g.*, as in Figs. 6a and 8a but without the horizontal cut-offs. An identical diamond-shaped surface applies for the two cases shown in Fig. 11a and b. The fcc crack orientation coinciding with Fig. 11a is sometimes observed in fatigue studies on ductile Cu and Al crystals, whereas the bcc crack orientation noted to coincide with Fig. 11b is a common cleavage crack orientation, *e.g.*, in Fe-3% Si crystals [16]. The term g_0 in (8) is the critical resolved shear stress in the x_1, x_2 plane of deformation for the double slip model. It corresponds to $g_0 = (2/\sqrt{3})\tau_0$ for the fcc interrelations and to $g_0 = \tau_0$ for bcc [2].

Contours of constant plastic strain (as measured by the accumulated sum of the slips, $\Gamma = \sum_i |\gamma_i^{(2)}|$) are shown in Figs. 11a and 11b for the orientations $\phi = 35.3^\circ$ and $\phi = 54.7^\circ$ respectively. The outermost contour is for $\Gamma = 0.005$, the next is for $\Gamma = 0.01$ and the innermost for $\Gamma = 0.02$. Away from the immediate near-tip region, the plastic deformation is confined to two discrete bands of deformation emanating from the crack tip. For a diamond shaped yield surface, the vertical ($\theta = 90^\circ$) discontinuity present in the small-scale yielding case (associated with the slip system represented by the dashed line in Fig. 2b) does not exist. The deformation in Fig. 11a corresponds to shear bands with the line of discontinuity parallel to the slip direction **S**. However, the deformation in Fig. 11b has the discontinuities aligned with the slip plane normal **N** which was discussed earlier as giving rise to kink bands and lattice rotation; see Fig. 3b and 3d. Not until we are within two to three initial root radii of the initial blunted crack tip does the straining pattern deviate significantly from that predicted from the small-scale yielding perfectly sharp crack tip results, based on the "small displacement gradient" formulation. The solutions for the two cases in Fig. 11 are identical within that formulation, and the slight broadening of the strain contours in Fig. 11b, compared to those in Fig. 11a, reflects geometrical hardening due to the lattice rotation in the Fig. 11b case.

The maximum extent of the plastic zone r_p varies nearly linearly with $a(\sigma'/g_0)^2 \propto K_I^2$ for values of $r_p/a \leq 0.018$, such that $r_p \approx 0.14 a(\sigma'/g_0)^2$. (The corresponding numerical factor is ≈ 0.15 in the ideally plastic fcc solution of Hawk ([6] Fig. 6c), and both results are close to the factor 0.16 based on the approximate ([19] Eqn. (37b)) model for yield on a pair of inclined shear planes at a crack tip, when the angle of those planes is taken as 55° with the cracking direction.) For larger plastic zone sizes in the Asaro solution, departures from such linearity occur indicating a departure from self-similar growth of the plastic zone, *i.e.*, a violation of small-scale yielding, presumably explainable over some range of σ' prior to full plasticity in terms of the nonsingular, crack-parallel stress ($= -\sigma'$) of the elastic crack tip field (*e.g.*, [20]).

Lattice rotations from the initial orientations, caused by plastic deformation at the crack tip, are shown in Figs. 12a and 12b. These show the deformed orientations of the traces of one of the slip plane families in the double-slip model. For the case with $\phi = 35.3^\circ$, Fig. 12a indicates that although quite large rotations occur at the crack tip itself, very little reorientation of the lattice occurred in the shear band regions. This is compatible with flow parallel to slip plane traces as in Fig. 3a. In contrast to this, Fig. 12b indicates, for the case where $\phi = 54.7^\circ$, rather discrete bands of lattice reorientation occur that more-or-less coincide with the bands of concentrated straining of Fig. 11b. By sighting along the slip plane traces in this latter case, one may observe a zone of kinking shear, as in Fig. 3b, extending out from the crack tip. This is further illustrated in Fig. 12c, also for the $\phi = 54.7^\circ$ case, in which contours of constant lattice rotation are shown. The outermost contour corresponds to a 2° rotation, and it protrudes out from the crack tip in the directions of the bands of concentrated straining in Fig. 11b; no such outward protrusion of regions of significant lattice rotation occurs in the $\phi = 35.3^\circ$ case. By comparing Figs. 12a and b, it is seen that although the overall plastic zone sizes differ little in the two cases, the patterns of large deformation in crack tip opening are quite different and seem to be dominated by the geometrical hardening and softening from lattice rotations. The results also show the development of features resembling "high-angle boundaries", or at least narrow transition zones between regions of significantly different lattice rotation, in the near tip region.

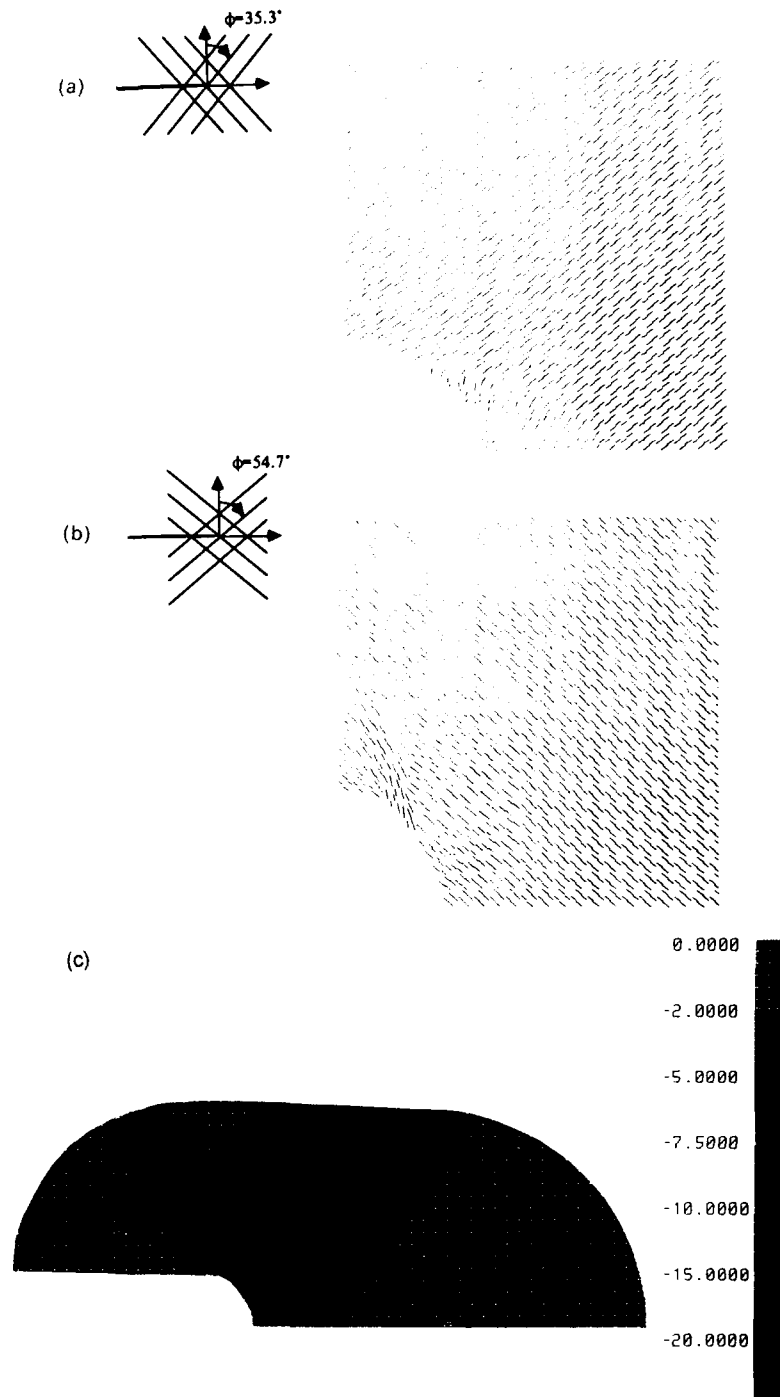


Fig. 12. Rotated orientations of slip plane traces (from one of the two slip systems in the double-slip model) near the crack tip: (a) For 35.3° angle between planes and tensile direction; shows little evidence of lattice rotation except near blunting tip. (b) For 54.7° angle; shows significant lattice rotation as in the kinking shear zone of Fig. 3(b). (c) Also for 54.7° angle; shows contours of constant lattice rotation near the tip, of which the outermost corresponds to 2° clockwise.

5. Conclusion

The analytical and numerical investigations into the near-crack-tip fields of ductile crystals have been shown to be consistent. The results show that for ideally plastic crystals obeying the Schmid rule, the near-crack-tip deformation fields are characterized by discontinuities in either displacement (stationary crack) or velocity (quasi-statically growing crack). These discontinuities are either parallel or normal to crystallographic planes on which slip can take place (i.e. by the motion of dislocations) for the *fcc* and *bcc* orientations considered. The state of stress is constant within angular sectors bounded by these discontinuities for material at yield.

The asymptotic methods developed [1, 2] provide a general way of constructing such fields around the crack once the yield surface has been determined for the particular crystal and orientation of the crack. In the case of a mode III crack [1, 3] a more complete analysis is possible of stationary cracks (exact full analysis) and quasi-static crack growth (asymptotic plus approximate analysis) and even dynamic crack growth (asymptotic). The general features seen in the mode III cases carry over to the physically more interesting mode I plane strain asymptotic analyses [2].

The numerical investigation of Hawk [6] by detailed finite element analyses provided confirmation that the features seen in the mode I asymptotic analyses (stationary and quasi-static growth) are valid over a finite size region. The finite element analysis of Asaro [6] of a center crack with initially rounded tip in a tension panel from small-scale yielding to general yielding, including hardening and full account of arbitrary displacement gradients, shows the effects of lattice rotation and the limits of small-scale yielding. However, the overall feature of concentrated deformation along the predicted discontinuities is retained throughout.

Finally, the analyses summarized here may provide some insight into why certain crystals undergo ductile fracture while others are brittle. One possible factor is the structure of the dislocations necessary to produce the predicted slip patterns which in one case involves a shear band parallel to the active slip system and in another involves a band perpendicular to the active system that deforms by kinking shear. In the parallel shear case it is possible for these dislocations to be generated at the crack tip and swept out along the slip planes while in the kinking case it is necessary to have present, and to activate, internal sources to generate the necessary dislocation dipoles. The finite strain pattern associated with large ductile opening at the crack tip is also significantly different in the two cases.

Acknowledgements

J.R. Rice and D.E. Hawk acknowledge the support of the Office of Naval Research under contract N00014-85-K-0045 to Harvard University. The computations of D.E. Hawk were carried out at the John von Neumann Center, Princeton N.J., under grant NAC-519 supported by the U.S. National Science Foundation. R.J. Asaro also acknowledges the support of the Office of Naval Research under contract N00014-88-K-0119 to Brown University. His computations were done during a June 1987 visit to Sandia National Laboratory, Livermore, Calif.

References

1. J.R. Rice and R. Nikolic, *Journal of the Mechanics and Physics of Solids* 33 (1985) 595-622.
2. J.R. Rice, *Mechanics of Materials* 6 (1987) 317-335.
3. R. Nikolic and J.R. Rice, *Mechanics of Materials* 7 (1988) 163-173.
4. J.R. Rice and M. Saeedvafa, *Journal of the Mechanics and Physics of Solids* 36 (1988) 189-214.
5. M. Saeedvafa and J.R. Rice, *Journal of the Mechanics and Physics of Solids* (1989) in press.
6. D.E. Hawk and R.J. Asaro, work in progress on finite element analysis of cracked elastic-plastic crystals (1988).
7. G.I. Taylor and C.F. Elam, *Proceedings of the Royal Society of London* A102 (1923) 643.
8. G.I. Taylor and C.F. Elam, *Proceedings of the Royal Society of London* A108 (1925) 28.
9. G.I. Taylor, in *Stephen Timoshenko 60th Anniversary Volume*, Macmillan, New York (1938) 218-224.
10. R.J. Asaro, in *Advances in Applied Mechanics*, J.W. Hutchinson (ed.), 23 (1983) 1-115.
11. J.R. Rice, *Journal of the Mechanics and Physics of Solids* 21 (1973) 63-74.
12. J.W. Hutchinson, *Proceedings of the Royal Society of London* A350 (1976) 101-127.
13. J. Pan and J.R. Rice, *International Journal of Solids and Structures* 19 (1983) 973-987.
14. D. Pierce, R.J. Asaro, and A. Needleman, *Acta Metallurgica* 31 (1983) 1951-1976.
15. W.J. Drugan and J.R. Rice, in *Mechanics of Material Behavior*, G.J. Dvorak and R.T. Shield (eds.), Elsevier, Amsterdam (1984) 59-73.
16. A.S. Tetelman and W.D. Robertson, *Acta Metallurgica* 11 (1963) 415-426.
17. J.C. Nagtegaal, D.M. Parks, and J.R. Rice, *Computer Methods in Applied Mechanics and Engineering* 4 (1974) 153-177.
18. R.J. Asaro and A. Needleman, *Acta Metallurgica* 33 (1985) 923-953.
19. J.R. Rice, in *Fatigue Crack Propagation*, ASTM STP 415 (1967) 247-309.
20. J.R. Rice, *Journal of the Mechanics and Physics of Solids* 22 (1974) 17-26.

Elastic-Plastic Analysis of Cracks on Bimaterial Interfaces: Part II—Structure of Small-Scale Yielding Fields

C. F. Shih

R. J. Asaro

Division of Engineering,
Brown University,
Providence, R. I. 02912

In Part I we found that although the near tip fields of cracks on bimaterial interfaces do not have a separable form of the HRR type, they appear to be nearly separable in an annular zone within the plastic zone. Furthermore, the fields bear strong similarities to mixed mode HRR fields for homogeneous medium. Based on our numerical results, we have been able to identify a clear mathematical structure. We found that the small-scale yielding crack tip fields are members of a family parameterized by a near tip phase angle ξ , and that the fields nearly scale with the value of the J-integral. In Part II, the original derivation of the mathematical structure of the small-scale yielding fields is elaborated upon. The issue of crack face contact is addressed and the phenomenology is described in terms of the phase parameter ξ . Crack tip plastic deformation results in an open crack for a range of ξ which is nearly symmetric about the state corresponding to pure remote tension. Plane-strain plastic zones and crack tip fields for the complete range of ξ are presented. Over distances comparable to the size of the dominant plastic zone, the stress levels that can be achieved are limited by the yield stress of the weaker (lower yield strength) material. On the other hand, the stresses well within the plastic zone are governed by the strain-hardening behavior of the more plastically compliant (lower strain-hardening) material. We observe that the extent of the annular zone where the fields are nearly separable (i.e., of the HRR form) is dependent on the remote load combinations and the material combination. When the tractions on the interface are predominantly tensile, there are no indications of crack face contact over any length scale of physical relevance. Instead, the crack tip opens smoothly and crack tip fields as well as the crack opening displacement are scaled by the J-integral. The paper concludes with a discussion on the range of load combinations which could be applied to two fracture test specimen geometries to obtain valid fracture toughness data.

1 Introduction

In Part I of this article (Shih and Asaro, 1988), numerical solutions were presented for the elastic-plastic fields of a crack on the interface between a nonlinear power-law hardening material and a rigid substrate. Specifically, the problem of an infinite crack embedded in an infinite bimaterial body (see Fig. 1) subject to combinations of remote tension and shear was analyzed under loading conditions that caused small-scale yielding. The calculations were performed for a material described by a small strain, isotropic J_2 deformation theory. This

facilitated making the connection between the interface crack solutions, the existing framework for nonlinear fracture mechanics, and specific solutions for crack tip fields in homogeneous media (e.g., Hutchinson, 1983). In one sense the work complimented analyses such as that of Knowles and Sternberg (1983) who studied the behavior of an interface crack between two neo-Hookean sheets. In these analytic asymptotic solutions, as well as the numerical solutions of Part I, it was shown that pathological features of the linear elastic solutions, such as the near tip oscillations in stresses and displacements are strongly mitigated by nonlinear kinematics or material behavior. The linear elastic asymptotic solutions, which provided the point of departure for our numerical analyses, were discussed in Part I.

The numerical analyses described in Part I also provided clarification of the structure of the small-scale yielding fields. In particular, it was found that the interface crack small-scale

Contributed by the Applied Mechanics Division of THE AMERICAN SOCIETY OF MECHANICAL ENGINEERS for publication in the JOURNAL OF APPLIED MECHANICS.

Discussion on this paper should be addressed to the Editorial Department, ASME, United Engineering Center, 345 East 47th Street, New York, N. Y. 10017, and will be accepted until two months after final publication of the paper itself in the JOURNAL OF APPLIED MECHANICS. Manuscript received by ASME Applied Mechanics Division, April 25, 1988; final revision, February 1, 1989.

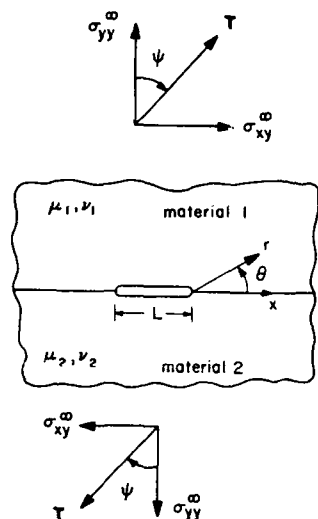


Fig. 1 Crack on bimaterial interface

yielding fields are members of a family parameterized by a near-tip *phase angle*, ξ , defined as $\xi \equiv \phi + \epsilon \ln(Q\bar{Q}/\sigma_0^2 L)$. Q is a complex stress intensity factor defined by the linear elastic asymptotic solution, ϕ is its phase angle, L is a characteristic crack dimension, σ_0 is the yield stress of the weaker material, and ϵ is a elastic bimaterial constant. We found that the dependence of the crack tip fields on radial distance is nearly of the HRR form for asymptotic fields in homogeneous media (Hutchinson, 1968; Rice and Rosengren, 1968) and that the small-scale yielding fields nearly scale with the value of the J -integral (Rice, 1968). This structure is reviewed in Section 2 of this paper.

In the present paper we describe the small-scale yielding fields in more detail and also demonstrate how the phenomenology of crack face contact can be described in terms of ξ . In the absence of plastic deformation, the range of ξ for which the crack is *open* is skewed about the state corresponding to pure remote tension. In contrast, crack tip plastic deformation results in an *open* crack range, which is more nearly symmetrical about the state corresponding to pure remote tension. We make contact with a dimensional analysis by Rice (1988) and a subsequent study by Zywicz and Parks (1988), which contain results which are consistent with our general framework.

The plan of the paper is as follows. In the next section the structure of the small-scale yielding fields is described. Numerical methods and the finite element boundary problems are described in Section 3. Results of plane-strain crack tip fields for two material combinations involving an elastic-plastic solid bonded onto an elastic substrate and, secondly, to an elastic-plastic material with different material properties, are presented in Section 4. The range of validity of linear elasticity and small-scale yielding solutions as they pertain to two fracture test specimens are discussed in Section 5.

2 Structure of Fields Under Small-Scale Yielding

2.1 Linear Elasticity Solutions. Solutions to specific problems of cracks lying along bimaterial interfaces of isotropic media have been given by Cherepanov (1962), England (1965), Erdogan (1965), and Rice and Sih (1965). More recently, Ting (1986) has presented a framework for determining the degree of singularity and the nature of the asymptotic fields for the general interfacial crack between two elastic anisotropic materials. Park and Earmme (1986), Hutchinson, Mear, and Rice (1987), and Suo and Hutchinson (1988) have obtained solutions for several elastic interfacial crack problems, and Rice (1988)

has reexamined elastic fracture mechanics concepts for interface cracks.

A crack of total length L lying on the interface between two semi-infinite slabs of isotropic elastic solids with differing material moduli is shown in Fig. 1. The shear moduli and Poisson's ratios are μ_1, μ_2 , and ν_1, ν_2 , and r and θ are polar coordinates centered at the crack tip. There are three independent non-dimensional material parameters but, as has been shown by Dundurs (1969), the solution for this class of problems depends on only two parameters. In plane strain they are

$$\beta_1 = [\mu_1(1 - \nu_2) - \mu_2(1 - \nu_1)] / [\mu_1(1 - \nu_2) + \mu_2(1 - \nu_1)] \quad (1)$$

$$\beta_2 = [\mu_1(1 - 2\nu_2) - \mu_2(1 - 2\nu_1)] / [\mu_1(1 - \nu_2) + \mu_2(1 - \nu_1)] \quad (2)$$

These parameters vanish for identical materials across the interface and change sign when the materials are interchanged.

At small distances from the crack tip, the in-plane stresses have the singular form

$$\sigma_{ij} = \text{Re} \left\{ \frac{Q}{\sqrt{2\pi r}} \left(\frac{r}{L} \right)^i \bar{\sigma}_{ij}(\theta; \epsilon) \right\} \quad (3)$$

where $i = \sqrt{-1}$, Q is the complex stress intensity factor, $|(r/L)^i| = 1$, and $\bar{\sigma}_{ij}(\theta; \epsilon)$ is the universal complex dimensionless angular function which depends on the bimaterial constant ϵ defined by (Williams, 1959) as

$$\epsilon = \frac{1}{2\pi} \ln \left(\frac{1 - \beta_2}{1 + \beta_2} \right) \quad (4)$$

In (3), L is a characteristic dimension of the crack geometry. As an example, L is identified as the crack length of the geometry depicted in Fig. 1. It is convenient to write Q as

$$Q = Q_1 + iQ_2 = |Q|e^{i\phi} \quad (5)$$

where $|Q|$ and ϕ are the amplitude and phase of Q . Thus, tractions on the bond line are

$$t = (\sigma_{yy} + i\sigma_{xy})_{\theta=0} = \frac{Q}{\sqrt{2\pi r}} \left(\frac{r}{L} \right)^i = \frac{|Q|}{\sqrt{2\pi r}} e^{i(\phi + \epsilon \ln(r/L))} \quad (6)$$

and displacement jumps across crack faces take the form

$$\begin{aligned} \Delta u &= \Delta u_y + i\Delta u_x = (u_y + iu_x)_{\theta=\pi} - (u_y + iu_x)_{\theta=-\pi} \\ &= \frac{8\Lambda}{\sqrt{1+4\epsilon^2}} \frac{|Q|\sqrt{r}}{\sqrt{2\pi}} e^{i(-\Theta + \phi + \epsilon \ln(r/L))} \end{aligned} \quad (7)$$

where $\Theta = \tan^{-1}2\epsilon$, and for plane strain $\Lambda = [(1 - \nu_1)/\mu_1 + (1 - \nu_2)/\mu_2] / (4\cosh^2 \pi\epsilon)$.

Different normalizations of the singular crack tip fields which result in stress intensity factors that differ by phase angles and scaling constants involving ϵ have appeared in the literature on interface cracks. Rice (1988) introduced the stress intensity factor K which is related to Q by

$$K = QL^{-i\epsilon}, |K| = |Q|, K\bar{K} = Q\bar{Q} \text{ and } \varphi = \phi - \epsilon \ln L \quad (8)$$

where φ is the phase of K . It is clear from (3) that K or $QL^{-i\epsilon}$ uniquely characterizes the crack tip fields. In other words, K fully accounts for the effects of both load and geometry on the crack tip field whereas Q and a characteristic length L are required for the same purpose. The merits of various definitions of stress intensity factors and possible approaches for recording and using fracture toughness data have been discussed by Rice (1988).

For the geometry depicted in Fig. 1 and stressed by remote traction $T(T = |T|e^{i\psi} = \sigma_{yy}^{\infty} + i\sigma_{xy}^{\infty})$, $Q = (1 + i2\epsilon)T\sqrt{\pi L/2}$ (Rice and Sih, 1965). The connection between the phase of Q and T is $\phi = \psi + \tan^{-1}2\epsilon$. Thus, changes in crack length at fixed

ψ (It is free to vary) do not change the phase of \mathbf{Q} . For later use, we note that $\varphi = -\epsilon \ln L + \psi + \tan^{-1} 2\epsilon$ for the geometry of Fig. 1.

A relation which will be of use later in the analysis is the energy release rate for the crack advancing along the interface (Malyshev and Salganik, 1965; Willis, 1971)

$$G = \Lambda \mathbf{Q} \bar{\mathbf{Q}} = \mathbf{A} \mathbf{K} \bar{\mathbf{K}} \quad (9)$$

where Λ is the parameter defined for (7).

The linear elasticity solution for the displacement jumps (7) predicts that overlapping of crack faces always occurs, though the zone of overlapping crack faces is very small compared to L for load states in the range $-45^\circ \leq \phi \leq 45^\circ$, i.e., $Q_1 > |Q_2|$. To redress this physically objectionable behavior, investigators have proposed various models and approaches. Comninou (1977a, b) and Comninou and Schmueser (1978) reformulated the linear elasticity boundary value problem to allow a zone of contact to develop at the crack tip. Solutions for a range of remote load combinations were obtained. Achenbach et al. (1979) introduced a Dugdale-Barenblatt strip yield zone at the crack tip which eliminated crack face overlapping as well as stress singularities altogether. Ortiz and Blume (1988) have obtained an inner solution, based on a zone of decohesion (and sliding) at the crack tip, which does not lead to interpenetrating crack faces in the region of dominance of this inner solution. Along similar lines of inquiry, Needleman (1987) has implemented a decohesion model in a finite element study of (rigid) inclusion debonding which takes account of finite geometry changes.

We take the view that while the elasticity solutions are invalid on the scale of the contact zone, they still provide an accurate description of the fields in an annular region surrounding the contact zone, as long as the size of the contact zone and plastic zone (if any) is small compared to the zone of dominance of the elastic fields given by (3). In this sense, crack face contact on a size scale which is much smaller than the crack length (or the relevant crack dimension) can be treated as a small-scale nonlinearity. Along this line of argument, Atkinson (1982) had used (3) as the outer solution and matched asymptotic expansions to derive an analytic contact zone solution for the Comninou (1977a) model. We will return to the issue of crack face contact following the discussion on the structure of the small-scale yielding fields.

2.2 Small-Scale Yielding Formulation. In the small-scale yielding formulation, the actual crack problem is replaced by a semi-infinite crack in an infinite media with the asymptotic boundary condition that at large r the field approaches that given by (3). The original derivation of the results to be discussed here is contained in an earlier publication (Shih and Asaro, 1988). It is elaborated upon here and contact is made with subsequent studies (and alternative approaches) which lead to results which are in agreement with our main conclusions.

Let σ_{01} and σ_{02} be the yield strengths of materials 1 and 2. It is convenient to designate the yield strength of the weaker solid by σ_0 , i.e., $\sigma_0 = \min(\sigma_{01}, \sigma_{02})$. Within the boundary layer formulation, the stresses depend on $\mathbf{Q}L^{-1/2}$ and σ_0 , and on dimensionless material parameters, e.g., σ_{02}/σ_0 , β_1 , β_2 , etc. By dimensional analysis,

$$\sigma_{ij} = \sigma_0 f_{ij} \left(\frac{r\sigma_0^2}{\mathbf{Q}\bar{\mathbf{Q}}}, \theta, \text{phase} \left\{ \mathbf{Q} \left(\frac{r}{L} \right)^{1/2} \right\}; \text{dimensionless material parameters} \right) \quad (10)$$

Here, f_{ij} is a dimensionless function of the dimensionless arguments and it may be noted that $\mathbf{Q}\bar{\mathbf{Q}}$ has dimensions of *square of stress times length*. Henceforth we will assume that the implicit dependence of f_{ij} on material parameters is understood.

Directing our attention to the dependence on σ_{ij} on \mathbf{Q} , L and distance from the crack tip we write

$$\sigma_{ij} = \sigma_0 f_{ij} \left(\frac{r\sigma_0^2}{\mathbf{Q}\bar{\mathbf{Q}}}, \theta, \phi + \epsilon \ln \left(\frac{r}{L} \right) \right) \quad (11)$$

where $\phi + \epsilon \ln(r/L)$ is the phase of $\mathbf{Q}(r/L)^{1/2}$. To reveal the structure of f_{ij} , it is advantageous to express the third argument as the sum of a constant phase angle and a variable phase angle which depends on distance r . To this end, the third argument is modified by incorporating a dependence on the first argument, viz.,

$$\phi + \epsilon \ln \left[\left(\frac{r}{L} \right) \left(\frac{\mathbf{Q}\bar{\mathbf{Q}}}{r\sigma_0^2} \right)^m \right] = \phi + \epsilon \ln \left(\frac{\mathbf{Q}\bar{\mathbf{Q}}}{L\sigma_0^2} \right) + (m-1)\epsilon \ln \left(\frac{\mathbf{Q}\bar{\mathbf{Q}}}{r\sigma_0^2} \right) \quad (12)$$

We should point out that the phase can depend on $\ln r$ in a manner which is more complex than that suggested by the last term in (12). In Part I we introduced a near-tip phase parameter, ξ , defined by

$$\xi = \phi + \epsilon \ln \left(\frac{\mathbf{Q}\bar{\mathbf{Q}}}{L\sigma_0^2} \right) \quad (13)$$

ξ varies linearly with ϕ , depends weakly on $\mathbf{Q}\bar{\mathbf{Q}}$ and L , and does not involve r . Making use of (13), the right-hand side of (12) can be written as

$$\xi + \text{phase} \left\{ \left(\frac{r\sigma_0^2}{\mathbf{Q}\bar{\mathbf{Q}}} \right)^{\Sigma} \right\} \quad (14)$$

where Σ is a dimensionless combination of material parameters yet to be determined. We use the latter result to restate (11) as

$$\sigma_{ij} = \sigma_0 f_{ij} \left(\frac{r\sigma_0^2}{\mathbf{Q}\bar{\mathbf{Q}}}, \theta, \text{phase} \left\{ \left(\frac{r\sigma_0^2}{\mathbf{Q}\bar{\mathbf{Q}}} \right)^{\Sigma} \right\}; \xi \right) \quad (15)$$

For the small-scale yielding analysis, it is convenient to phrase the remote load in terms of $|\mathbf{K}|$ (or $\mathbf{K}\bar{\mathbf{K}}/\sigma_0^2$) and its phase φ . Use (8) in (13) to obtain

$$\xi = \varphi + \epsilon \ln \left(\frac{\mathbf{K}\bar{\mathbf{K}}}{\sigma_0^2} \right) \quad (16)$$

The characteristic crack dimension, L , does not appear explicitly in the equation (16) for ξ , but has been absorbed in the phase of \mathbf{K} . Now, the general result in (15) has the alternative representation:

$$\sigma_{ij} = \sigma_0 f_{ij} \left(\frac{r\sigma_0^2}{\mathbf{K}\bar{\mathbf{K}}}, \theta, \text{phase} \left\{ \left(\frac{r\sigma_0^2}{\mathbf{K}\bar{\mathbf{K}}} \right)^{\Sigma} \right\}; \xi \right) \quad (17)$$

Since ξ is the phase angle of a complex quantity, f_{ij} has a periodicity of 2π with respect to the argument ξ , i.e.,

$$f_{ij}(\dots; \xi) = f_{ij}(\dots; \xi + m\pi) \quad m = 2, 4, 6. \quad (18)$$

Furthermore, due to the linearity of the equilibrium and strain-displacement equations

$$f_{ij}(\dots; \xi) = -f_{ij}(\dots; \xi + m\pi) \quad m = 1, 3, 5. \quad (19)$$

Thus, ξ serves as the phase parameter of the fields in the small-scale yielding formulation just as φ (or $\phi - \epsilon \ln L$) is the phase angle of the linear elastic singular fields. Using a different approach, Zywicki and Parks (1988) introduced a phase parameter ζ_0 which differs inconsequentially from (16) by a constant involving ϵ .

The mathematical structure of the fields expressed by (15), and (17)–(19) was derived without regard to contact between the crack faces. In fact, displacement jumps across the crack faces must have the form,

$$\Delta u_i = \epsilon_0 \frac{\mathbf{K}\bar{\mathbf{K}}}{\sigma_0^2} g_i \left(\frac{r\sigma_0^2}{\mathbf{K}\bar{\mathbf{K}}} \right), \text{ phase } \left\{ \left(\frac{r\sigma_0^2}{\mathbf{K}\bar{\mathbf{K}}} \right)^{1/2} \right\}; \xi \quad (20)$$

where ϵ_0 is a reference yield strain and the dimensionless function g_i has the periodic structure expressed by (18) and (19). In this paper our interest is restricted to the range of ξ where the crack faces are not in contact. The definition of an open crack will be introduced shortly and the validity of the proposed fields will be established in Section 4 in terms of the range of ξ . For the present, it is useful to examine the mathematical structure of the fields under the fictitious assumption that crack faces may overlap.

The effective stress σ_e ($\sigma_e^2 = 3s_{ij}s_{ij}/2$, where s_{ij} is the deviatoric stress), has the form

$$\sigma_e = \sigma_0 f_e \left(\frac{r\sigma_0^2}{\mathbf{K}\bar{\mathbf{K}}} \right), \theta, \text{ phase } \left\{ \left(\frac{r\sigma_0^2}{\mathbf{K}\bar{\mathbf{K}}} \right)^{1/2} \right\}; \xi \quad (21)$$

The elastic-plastic boundary in the weaker material is the locus of points where σ_e equals σ_0 . Substituting these values in (21) and rearranging leads immediately to the following results for the plastic zone (Shih and Asaro, 1988):

$$r_p(\theta) = \frac{\mathbf{K}\bar{\mathbf{K}}}{\sigma_0^2} R(\theta; \xi) \quad (22)$$

Here, $R(\theta; \xi)$ is a dimensionless angular function which depends on ξ and on dimensionless material parameters. Since σ_e is quadratic in the stress components which have periodicity expressed by (18) and (19), the angular function R has a periodicity of π with respect to ξ ,

$$R(\theta; \xi) = R(\theta; \xi + m\pi) \quad m = 1, 2, 3, \dots \quad (23)$$

Rice (1988) has derived the relation,

$$r_p = \frac{\mathbf{K}\bar{\mathbf{K}}}{\sigma_0^2} \tilde{R}(\phi - \epsilon \ln(L/r_p)) \quad (24)$$

by a similar dimensional analysis. In (24), r_p is a characteristic dimension of the plastic zone; for example, r_p can be taken to be the maximum extent of the plastic zone. Rice's implicit equation for r_p can be made explicit by replacing r_p in the argument by $\mathbf{K}\bar{\mathbf{K}}/\sigma_0^2$, whereupon a result similar to (22) is recovered.

The function $R(\theta; \xi)$ can be determined directly from plots of small-scale yielding plastic zones. This has been carried out for a range of phase angles ξ in Part I (Shih and Asaro, 1988) and for several material systems in this paper. Alternatively, an estimate of $R(\theta; \xi)$ can be obtained by approximating f_e in (21) by using the linear elasticity fields in (3). The latter procedure has been adopted by Zywicki and Parks (1988) to estimate plastic zone sizes and shapes.

2.3 Plausible Form of Asymptotic Fields. The size of the dominant plastic zone (which develops in the weaker material) is controlled by the yield strength of the weaker material σ_0 (see (22)). Over length scales which are comparable to the dominant plastic zone, the stress levels that can be achieved in both materials are set by σ_0 . On the other hand, we will argue that the form of the asymptotic crack tip fields is governed by the hardening characteristics of the material with the least hardening capacity.

We assume that each material of the material pair is characterized by a Ramberg-Osgood stress-strain relation where the uniaxial plastic strain is related to the stress by $\epsilon^p/\epsilon_0 = \alpha(\sigma/\sigma_0)^n$ where $\epsilon_0 = \sigma_0/E$. The plastic properties of material 1 (top material) are designated by α_1 , σ_{01} , and n_1 and those for material 2 are designated by α_2 , σ_{02} , and n_2 . The reference strains are defined by $\epsilon_{01} = \sigma_{01}/E_1$ and $\epsilon_{02} = \sigma_{02}/E_2$. We designate the larger of n_1 and n_2 by n , i.e., $n = \max(n_1, n_2)$. To avoid ambiguity in the discussions to follow, material 1

will be taken to be the lower hardening material and its elastic and plastic properties are designated by ν , E , α , σ_0 , ϵ_0 , and n .

Let E_{11} and E_{12} designate the tangent moduli of material 1 and 2, respectively. As $r \rightarrow 0$, and assuming that the stresses are singular, $E_{11}/E_{12} \rightarrow 0$. This suggests that, as $r \rightarrow 0$, the material system behaves increasingly like that of a plastically deforming material which is bonded to a rigid substrate. We will now argue that the form of the asymptotic fields is governed by the strain-hardening characteristics of material 1.

We assume that the response of the plastically deforming material is described by a J_2 deformation theory of plasticity. Path independence of the J -integral (Rice, 1968) is easily demonstrated for the interface crack once it is recognized that the contribution to the J -integral from the upper interface, $x_2 = 0^+$, is negated by the contribution from the lower interface, $x_2 = 0^-$. Now, take a circular contour centered at the tip and use path independence to shrink the contour onto the crack tip. Since J is nonzero, as it must be for a deformation theory solid (in this case the J -integral is precisely the energy release rate), we conclude that the strain energy density $W \sim 0(1/r)$ as $r \rightarrow 0$. This requires the product of stress and strain to have a $1/r$ singularity. If it is further assumed that the fields have a product dependence on the first argument of f_{ij} (17), then singular solutions, if they exist, would have the form

$$\sigma_{ij} = \sigma_0 \left(\frac{\mathbf{K}\bar{\mathbf{K}}}{\sigma_0^2} \right)^{1/(n+1)} \tilde{h}_{ij}(\theta, \text{phase } \{ \hat{r}^{1/2} \}; \xi) \quad (25)$$

where $\hat{r} = r/(\mathbf{K}\bar{\mathbf{K}}/\sigma_0^2)$, and the implicit dependence of \tilde{h}_{ij} on material parameters is understood.

The dimensionless function \tilde{h}_{ij} has a periodic dependence (with period 2π) on ξ , and the arguments leading to (25) require that \tilde{h}_{ij} be bounded. Though \tilde{h}_{ij} is a bounded function, it can nevertheless oscillate rapidly as $\hat{r} \rightarrow 0$. Under small-scale yielding, $J = \mathcal{G}$ (Rice, 1968) and noting the relation between \mathcal{G} and $\mathbf{K}\bar{\mathbf{K}}$ (9), the singular fields can be arranged in the form

$$\sigma_{ij} = \sigma_0 \left(\frac{J}{\alpha \sigma_0 \epsilon_0 r} \right)^{1/(n+1)} h_{ij}(\theta, \text{phase } \{ \hat{r}^{1/2} \}; \xi) \quad (26)$$

where $h_{ij} = (\alpha/\Lambda E)^{1/(n+1)} \tilde{h}_{ij}$ and Λ has been defined in connection with (7). It may be noted that (26) is consistent with the product form of the linear elastic fields (3) involving a bounded \tilde{h}_{ij} which depends on the phase $\{(r/L)^{1/2}\}$.

It is instructive to examine the dependence of h_{ij} on r for two special cases. Suppose that both materials are elastic and $\epsilon \neq 0$. At fixed θ , the stresses have the form $\sigma_{ij} \propto r^{-1/2} h_{ij}(\hat{r}; \xi, n)$. Comparing this form with (3), we conclude that the variation of h_{ij} with r is bounded but rapidly oscillatory as $r \rightarrow 0$. Now suppose that one material is rigid-perfectly plastic. Then, h_{ij} is again bounded and the term multiplying it, $r^{-1/(n+1)} (n \rightarrow \infty)$, is also bounded.

As a third example, we take materials 1 and 2 to be strain-hardening materials with $n_1 > n_2$. Then by (26), the stresses above the bond line ($\theta = 0^+$) are of the form $\sigma_{ij} \sim r^{-1/(n_1+1)} h_{ij}(\hat{r}; n_1)$. For the moment, suppose that the stresses below the bond line ($\theta = 0^-$) have the form $\sigma_{ij} \sim r^{-1/(n_2+1)} h_{ij}(\hat{r}; n_2)$. Continuity of traction across the bond line requires that $r^{-1/(n_1+1)} h_{2j}(\hat{r}; n_1) = r^{-1/(n_2+1)} h_{2j}(\hat{r}; n_2) = O(r^\lambda)$. For $n_1 \neq n_2$, the equality can be met only if h_{2j} is singular as $r \rightarrow 0$, which contradicts the original assumption that h_{ij} is bounded. In fact, if the stresses are assumed to have a power dependence on r such that traction is continuous across the bond line, i.e., $\sigma_{ij} \sim r^\lambda h_{ij}$ for both materials 1 and 2, then continuity of displacements across the bond line cannot be satisfied. Similarly, if the displacements are continuous across the bond line and are of the form $u_i \sim r^\lambda \tilde{u}_i$ for materials 1 and 2, then continuity of traction cannot be satisfied. However, if we assume that as $r \rightarrow 0$ the material system behaves like that of a plastically-deforming material bonded to a rigid substrate, then (26) proves to be an admissible form.

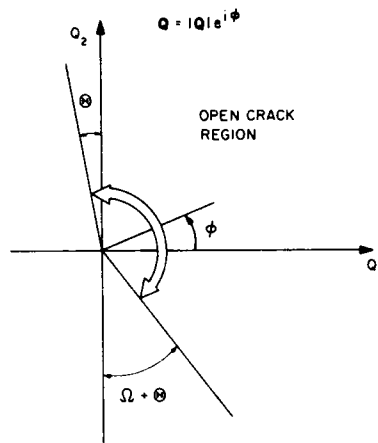


Fig. 2 Open crack domain in Q plane

It is convenient to write (26) in the form

$$\sigma_{ij} = \sigma_0 \left(\frac{J}{\alpha \sigma_0 \epsilon_0 r} \right)^{1/(n+1)} h_{ij}(\theta, \hat{r}; \xi, n) \quad (27)$$

where h_{ij} is a bounded function with respect to \hat{r} and

$$\xi = \phi + \epsilon \ln \left(\frac{Q\bar{Q}}{\sigma_0^2 L} \right) = \phi + \epsilon \ln \left(\frac{K\bar{K}}{\sigma_0^2} \right) = \phi + \epsilon \ln \left(\frac{J}{\Lambda \sigma_0^2} \right).$$

(28)

The form of the fields (27) has been corroborated by the numerical solutions of Section 4. These full field solutions also show that for load states in the range $-\pi/6 \leq \xi \leq \pi/6$, h_{ij} is a slowly varying function of \hat{r} over all physically-relevant length scales. Thus, the near tip fields nearly scale with $J^{1/(n+1)}$, since h_{ij} is only weakly dependent on J through the phase parameter ξ . Moreover, these near tip fields of an interface crack display strong similarities to mixed mode HRR fields.

When the plane ahead of the crack is stressed by tension and shear, the HRR singularity (Hutchinson, 1968; Rice and Rosengren, 1968) for homogeneous media has the form (Shih, 1974)

$$\sigma_{ij} = \sigma_0 \left(\frac{J}{\alpha \sigma_0 \epsilon_0 r} \right)^{1/(n+1)} \bar{\sigma}_{ij}(\theta; M^p, n). \quad (29)$$

Here, M^p is the mixity of the plastic singular fields defined by the relative magnitudes of $\sigma_{\theta\theta}$ and $\sigma_{r\theta}$ along the radial line $\theta = 0$ as $r \rightarrow 0$. The angular functions $\bar{\sigma}_{ij}$ for several values of M^p have been tabulated by Symington et al. (1988). Under small-scale yielding, the effects of load and geometry on the crack tip field of homogeneous media are characterized by J and M^p . The structure of the near tip fields (27) suggests that J and ξ are the characterization parameters of the near tip fields of cracks on bimaterial interfaces.

2.4 Range of ξ for an Open Crack. According to the linear elasticity solution, overlapping of crack faces will occur at some distance for all values of ϕ if $\epsilon \neq 0$. Nevertheless, for a range of ϕ the zone of interpenetration is confined to a distance from the crack tip that is smaller than physically relevant length scales. For this reason, we define a crack to be *open* if

$$\Delta u_2 \geq 0 \text{ for } r_c \leq r \leq L \quad (30)$$

where r_c is small compared to L . The size of the contact zone can be estimated by using the elasticity solution (7). From (7), the opening gap between the crack faces, Δu_2 is positive over distances r/L which satisfy

$$-\pi/2 \leq \phi + \epsilon \ln(r/L) - \Theta \leq \pi/2. \quad (31)$$

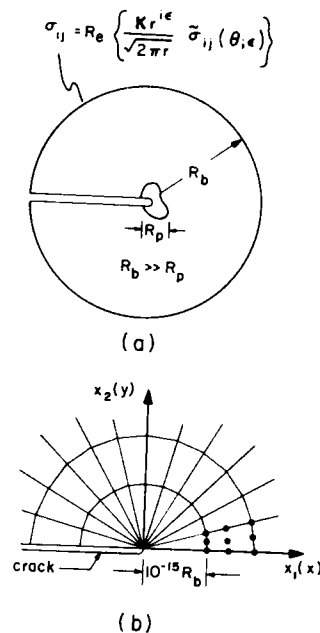


Fig. 3 (a) Small-scale yielding formulation and (b) finite element mesh of upper half of crack tip region and crack tip conventions

Table 1

ϵ	$\Theta(\text{deg})$	r/L	$\Omega(\text{deg})$
0.025	2.86	10^{-2}	6.6
		10^{-3}	9.89
		10^{-4}	13.2
		10^{-6}	19.8
0.050	5.71	10^{-2}	13.2
		10^{-3}	19.8
		10^{-4}	26.4
		10^{-6}	39.6
0.100	11.3	10^{-2}	26.4
		10^{-3}	39.6
		10^{-4}	52.8
		10^{-6}	79.2
0.175	19.3	10^{-2}	46.2
		10^{-3}	69.3
		10^{-4}	92.3
		10^{-6}	139.0

For the case $\epsilon = 0$, (31) states that the crack is open as long as the Mode I stress intensity factor is positive. Let $\Omega = -\epsilon \ln(r_c/L)$ and recall that $\Theta = \tan^{-1} 2\epsilon$. Then, by combining (30) and (31), the *open* crack range in terms of ϕ is

$$-\pi/2 + \Omega + \Theta \leq \phi \leq \pi/2 + \Theta. \quad (32)$$

Figure 2 depicts the *open* crack region in the Q plane. Values of Ω and Θ for four values of ϵ and four values of r_c/L are tabulated in Table 1. Since $\phi = \psi + \Theta$ for the geometry in Fig. 1, the range of phase angles of the remote load for an *open* right crack tip is

$$-\pi/2 + \Omega \leq \psi \leq \pi/2. \quad (33)$$

The characteristic length in the small-scale yielding formulation is $K\bar{K}/\sigma_0^2$ (or $Q\bar{Q}/\sigma_0^2$). Therefore, crack face contact under small-scale yielding must be phrased in terms of the normalized distance \hat{r} ($\equiv r/(K\bar{K}/\sigma_0^2) = r/(Q\bar{Q}/\sigma_0^2)$). The form of the desired result can be obtained with the help of the elasticity result (31). Using the plastic phase angle ξ , defined by (13), we rewrite (31) as

$$-\pi/2 \leq \xi + \epsilon \ln \hat{r} - \Theta \leq \pi/2. \quad (34)$$

Under small-scale yielding, the crack is *open* crack if

$$\Delta u_2 \geq 0 \text{ for } c_1 \leq \hat{r} \leq c_2 \quad (35)$$

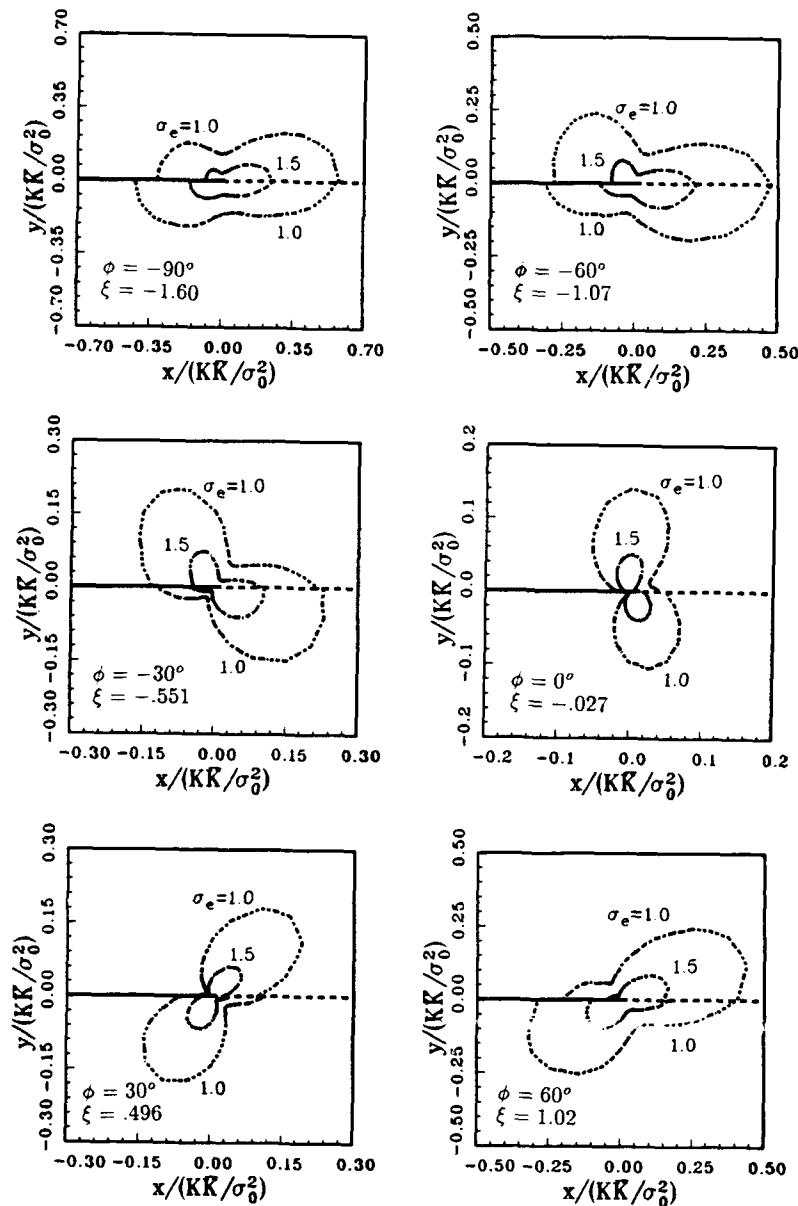


Fig. 4 Elastic-plastic material bonded onto elastic substrate—effective stress contours and plastic zones of six load states

where $c_1 \ll 1$ and $c_2 \gg 1$. Combining (34) and (35) and approximating Θ by 2ϵ , the range of ξ for an *open* crack is

$$-\pi/2 + \epsilon(2 - \ln c_1) \leq \xi \leq \pi/2 + \epsilon(2 - \ln c_2). \quad (36)$$

Suppose $\ln c_1 = -2$ and $\ln c_2 = 2$ ($c_2 = 1/c_1 = 7.5$), then (36) reduces to $-\pi/2 + 4\epsilon \leq \xi \leq \pi/2$. If $\ln c_1 = -4$ and $\ln c_2 = 4$ ($c_2 = 1/c_1 = 55$), the range is decreased by 4ϵ , $-\pi/2 + 6\epsilon \leq \xi \leq \pi/2 - 2\epsilon$. A more accurate estimate of the *open* crack range based on the small-scale yielding solutions is discussed in Section 4.

3 Problem Description and Numerical Procedures

3.1 Boundary Conditions and Mesh Design. Computations were performed in Part I for a full boundary value problem involving an interface crack lying on a bimaterial interface of the center-cracked-panel geometry, and for small-scale yielding fields produced by loading the crack tip with a *remote* \mathbf{K} stress field which is referred to as the boundary layer formulation.

The calculations to be discussed in Section 4 are all of the latter type, although contact will be made with the full boundary value problem presented in Part I. Loading is prescribed by imposing the stresses of the asymptotic linear elastic field, given by (3),

$$\sigma_{ij} = \text{Re} \left\{ \frac{\mathbf{K} r^{i\epsilon}}{\sqrt{2\pi r}} \bar{\sigma}_{ij}(\theta; \epsilon) \right\}, \quad (37)$$

on the remote boundary, R_b as depicted in Fig. 3(a).

The finite element mesh is constructed with 9-node biquadratic Lagrangian elements. An arrangement of wedge-shaped elements is employed at the crack tip; this innermost ring of elements has dimensions of $10^{-15} R_b$. The upper half of the crack tip mesh and the spatial coordinates are shown in Fig. 3(b). Accommodating the 15 orders of magnitude in element size while still preserving the aspect ratio of the element is accomplished by exponential scaling of element size in the

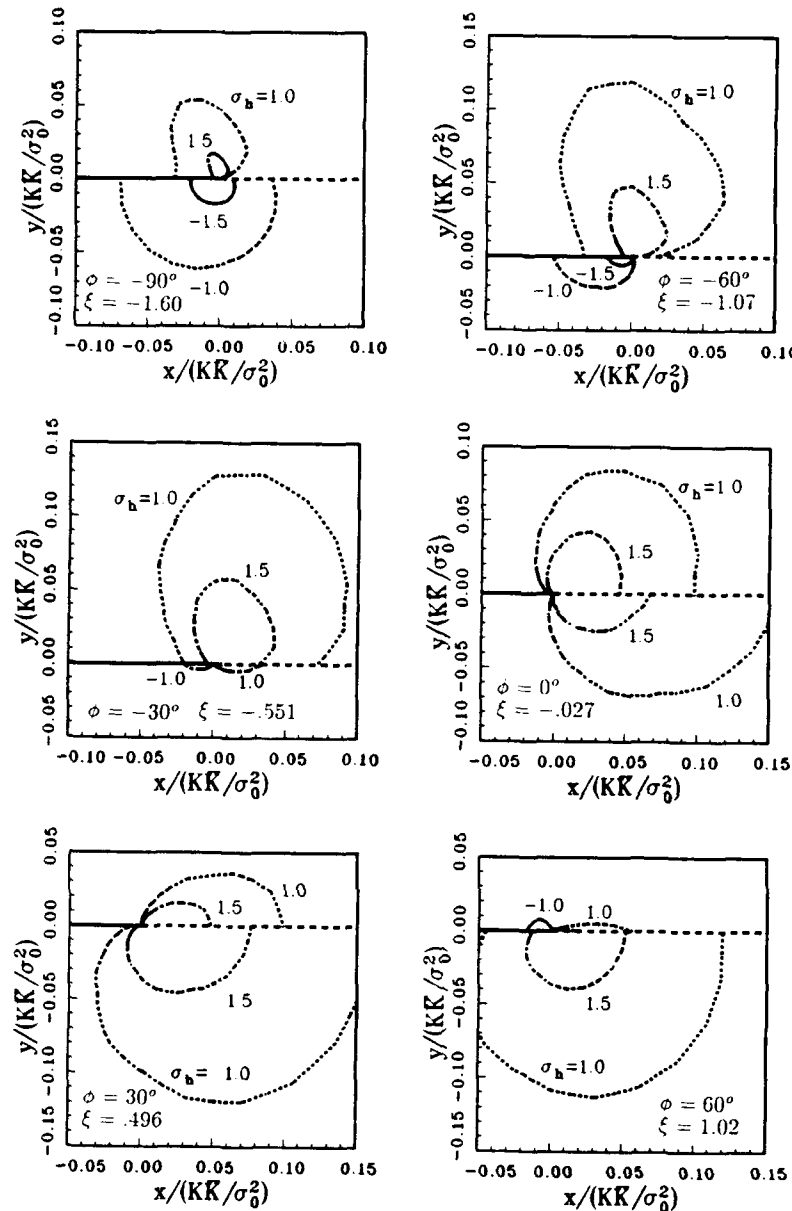


Fig. 5 Elastic-plastic material bonded onto elastic substrate—hydrostatic stress contours of six load states

radial direction. Each decade of radial distance is spanned by four annular strips of elements. In this manner, the domain between $10^{-15} R_b$ and R_b is spanned by 60 strips of elements. Within each strip, twelve equally-sized elements span the interval $-\pi \leq \theta \leq 0$ (the bottom material), and another twelve elements span the interval $0 \leq \theta \leq \pi$ (the top material). The mesh has a total of 1464 elements and 5980 nodes. A more complete description of a similar finite element mesh and the element arrangements has been given in Part I.

3.2 Material Laws. The deformable media are described by a J_2 deformation theory with a Ramberg-Osgood stress-strain behavior. In uniaxial tension the material deforms according to

$$\epsilon/\epsilon_0 = \sigma/\sigma_0 + \alpha(\sigma/\sigma_0)^n, \quad (38)$$

where σ_0 and ϵ_0 are the yield stress and strain, α is a material constant (taken to be 0.1), and n is the power-law strain-hardening exponent. Under multi-axial stress states the strain is given by

$$\epsilon_{ij} = \frac{1+\nu}{E} s_{ij} + \frac{1-2\nu}{3E} \sigma_{kk} \delta_{ij} + \frac{3}{2} \alpha \left(\frac{\sigma_e}{\sigma_0} \right)^{n-1} \frac{s_{ij}}{E}. \quad (39)$$

Here s_{ij} is the stress deviator, $\sigma_e = (3s_{ij}s_{ij}/2)^{1/2}$ is the effective stress, and ν and E are the isotropic elastic constants. In (38) the connection $\sigma_0 = E\epsilon_0$ was used. Numerical solutions for $n = 2$ through $n = 10$ have been obtained; in the present paper, however, only results for $n = 5$ and selected results for $n = 10$ are presented.

3.3 Numerical Procedure. The numerical procedure employed in this study is discussed in Part I. Only a summary of the procedures will be provided in this section. As noted in Section 3.2, the cracked body is modeled by 9-node Lagrangian quadrilateral elements. To avoid numerical difficulties which arise from nearly incompressible plastic deformation, the strain-displacement matrix, \mathbf{B} , is formed using the B -bar method (Hughes, 1980). The deviatoric part of \mathbf{B} , \mathbf{B}^{dev} , is evaluated at a 3×3 array of quadrature points, while the volumetric part,

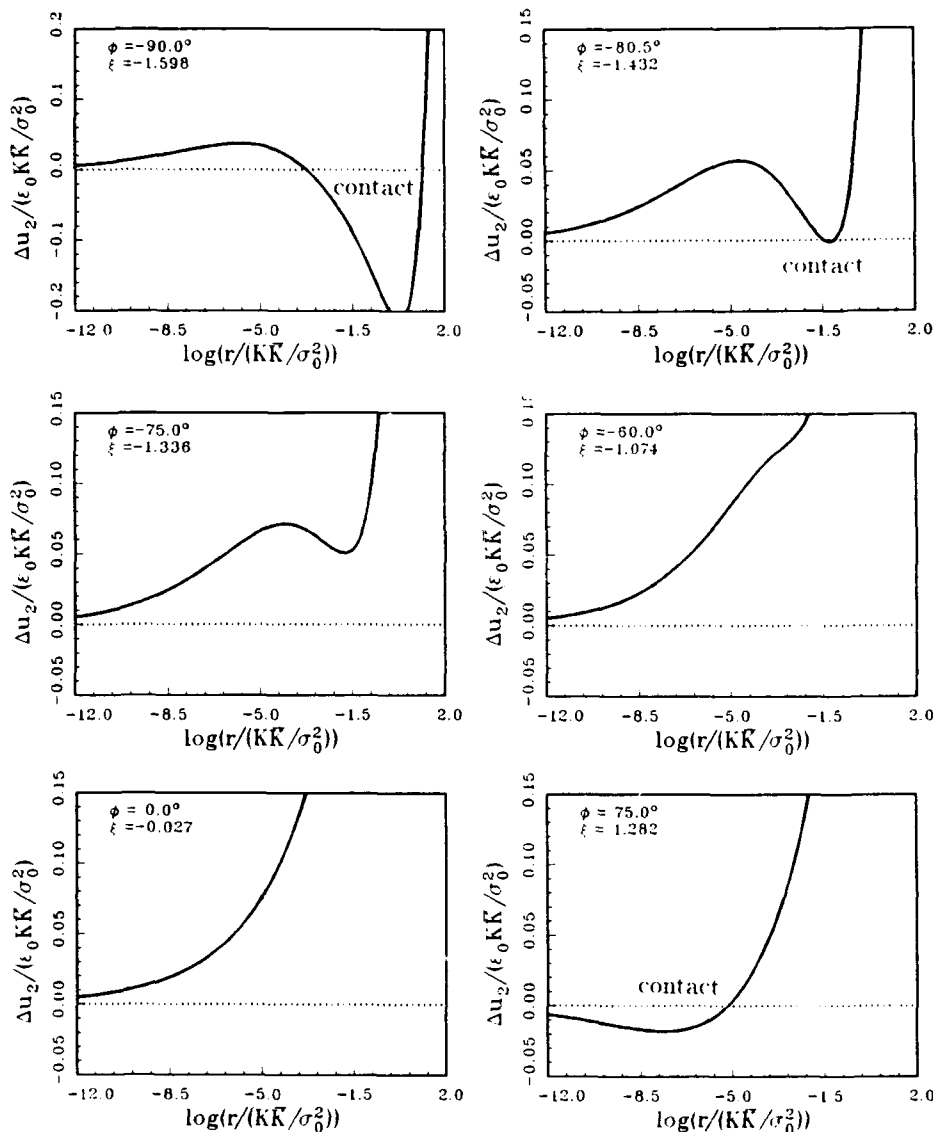


Fig. 6 Elastic-plastic material bonded onto elastic substrate—normal displacement jumps of six load states. Crack face contact (if any) is indicated.

\mathbf{B}^{vol} , is evaluated at a reduced array of 2×2 quadrature points. The desired matrix is given by

$$\bar{\mathbf{B}} = \mathbf{B}^{\text{dev}} + \bar{\mathbf{B}}^{\text{vol}} \quad (40)$$

where $\bar{\mathbf{B}}^{\text{vol}}$ is associated with the 3×3 quadrature points by a bilinear interpolation/extrapolation. The tangent stiffness matrix for an element is given by the sum of the inner products at each Gauss point, viz.,

$$\mathbf{k}^e = \sum_{p=1}^9 (\bar{\mathbf{B}} \mathbf{D} \bar{\mathbf{B}}) w_p \quad (41)$$

where \mathbf{D} is the matrix of material moduli evaluated at the 3×3 quadrature points and w_p is the appropriate weight.

The solution to the nonlinear boundary value problem is obtained by the Newton-Raphson method which is second-order convergent if a close initial estimate of the solution is available. Such an estimate is generated by parameter tracking (Shih and Needleman, 1984).

It is advantageous to work with area/domain integrals in finite element computations. In this regard it may be noted that with the help of a weighting function, a contour integral

(path-independent or not) can be restated as an area/domain integral (e.g., Moran and Shih, 1987). To this end consider the path-independent J -integral defined as in Eshelby (1956), or specifically for cracks as in Rice (1968), by

$$J = \int_{\Gamma} \left[W \delta_{ij} - \sigma_{ij} \frac{\partial u_i}{\partial x_j} \right] n_j d\Gamma. \quad (42)$$

Here, W is the strain energy density, σ_{ij} and $(\partial u_i / \partial x_j)$ are the stresses and displacement gradients, respectively, Γ is a contour beginning at the bottom crack face and ending on the top crack face, and \mathbf{n} is the outward pointing normal to Γ . A weighting function $q_1(x_1, x_2)$ is assigned a value of unity on the inner contour Γ , a value of zero on the outer contour C_0 and is a smooth (C^0) function in the domain bounded by Γ , C_0 , and the crack faces C_+ and C_- (these contours are shown in Fig. 4 of Part I). The integral in (42) can then be restated as an integral over a closed contour C , viz.,

$$J = \int_C \left[\sigma_{ij} \frac{\partial u_i}{\partial x_j} - W \delta_{ij} \right] m_j q_1 dC. \quad (43)$$

Here, \mathbf{m} is the unit normal to C pointing away from the en-

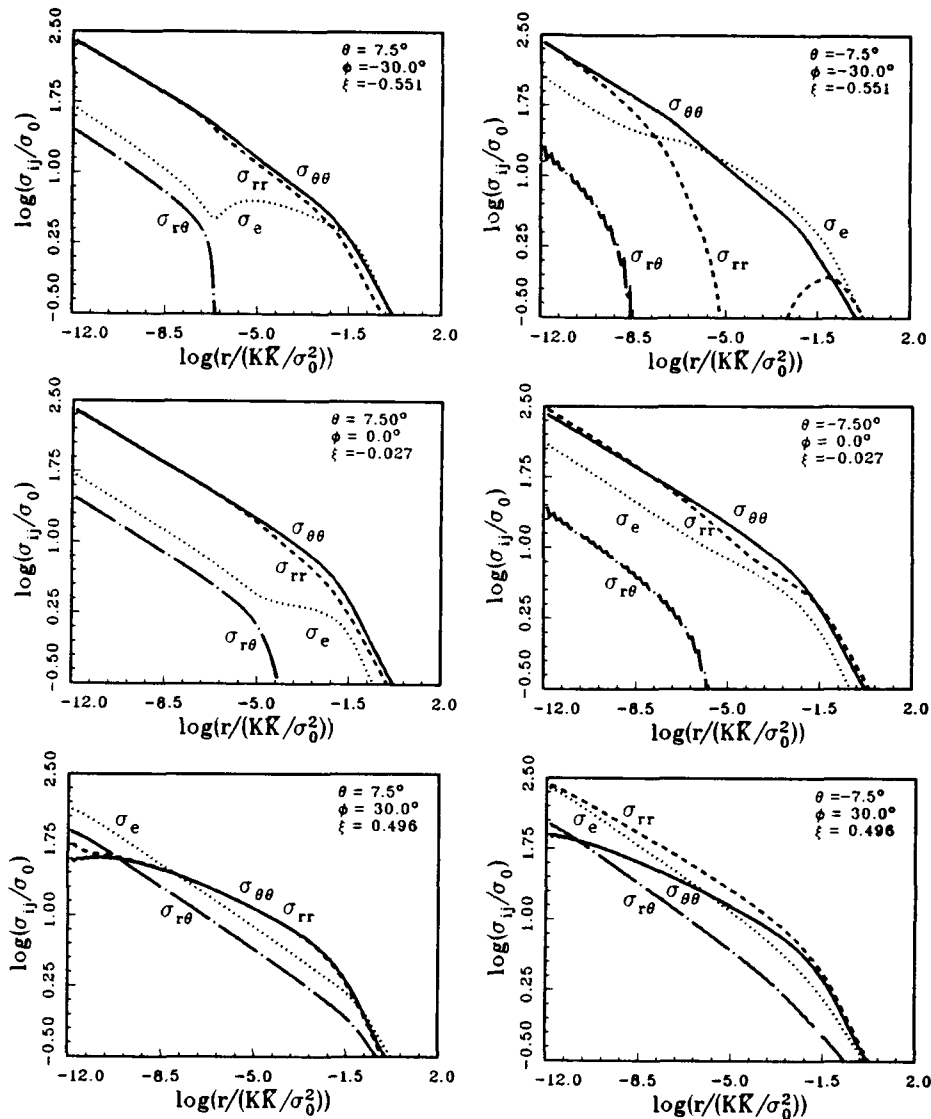


Fig. 7 Variation of normalized stresses with log of normalized distance in elastic-plastic material ($\theta = 7.5$ deg) and in elastic substrate ($\theta = -7.5$ deg) for three load states

closed area; on the contour, Γ , m points opposite to n . The derivation assumes that the crack faces are traction-free. Applying the divergence theorem to the integral in (43), and using the equations of equilibrium, the equivalent domain representation of (42) is

$$J = \int_A \left[\sigma_{ij} \frac{\partial u_i}{\partial x_j} - W \delta_{ij} \right] \frac{\partial q_1}{\partial x_j} dA \quad (44)$$

where A is the area enclosed by C . The finite element form of (44) is given in Part I.

4 Numerical Solutions for Small-Scale Yielding

Full field numerical solutions under plane-strain assumptions have been obtained for a range of bimaterial constants and different combinations of plastic properties for materials 1 and 2. In the interest of length, only two material combinations are discussed in this section.

4.1 Elastic-Plastic Material on Elastic Substrate. Material 1 is elastic-plastic while material 2 is linear elastic. The elastic properties are $\nu_1 = \nu_2 = 0.3$ and $E_2/E_1 = 2.5$; the values of

the Dundur's parameters are then $\beta_1 = -0.429$ and $\beta_2 = -0.122$, whereas $\epsilon = 0.039$. Plastic properties of the top material are characterized by yield stress σ_0 , strain-hardening exponent n which is equal to 5, and α which has a value of 0.1.

Numerical solutions are presented for seven states of remote load as defined by $K\bar{K}/\sigma_0^2 L = 0.5$, and the elastic phase parameter $\phi = -90$ deg, -60 deg, -30 deg, 0 deg, 30 deg, 60 deg, 90 deg. The small-scale yielding phase parameter, ξ , defined by (13), has these values: -1.60 , -1.07 , -0.551 , -0.027 , 0.496 , 1.02 , and 1.54 . Under small-scale yielding conditions,

$$J = G = \Lambda Q \bar{Q} = \Lambda K \bar{K} \quad (45)$$

where for plane strain, $\Lambda = [(1 - \nu_1)/\mu_1 + (1 - \nu_2)/\mu_2] / (4 \cosh^2 \pi \epsilon)$. The value of J was computed using (44) and a "plateau" weighting function. The J values, which were extracted from annular domains with mean radii that differed by up to fifteen orders of magnitude (10^{-15}), agreed to better than two significant digits with the exact result given by (45). The essentially exact path-independence of the numerically determined J and the excellent agreement with (45) is indicative of the quality of the numerical solutions.

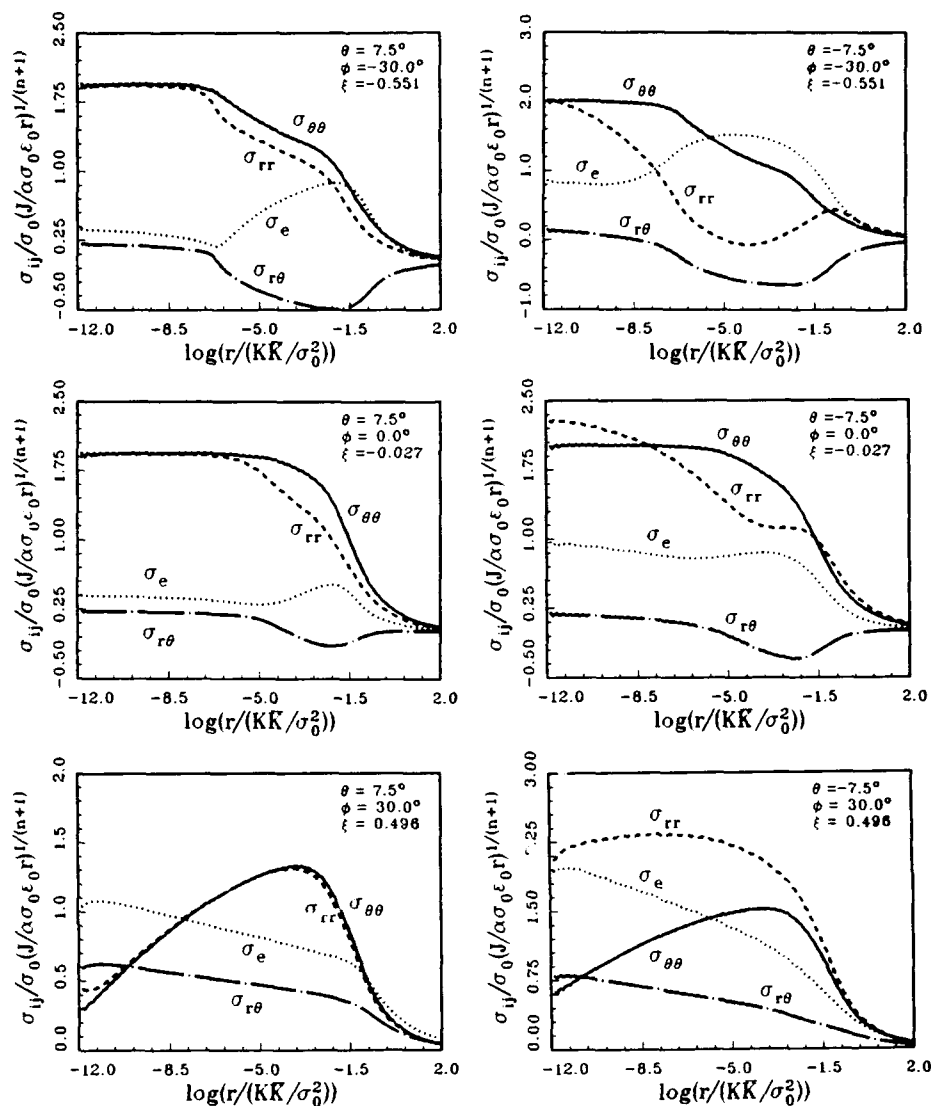


Fig. 8 Variation of stresses normalized by HRR form with log of normalized distance in elastic-plastic material ($\theta = 7.5$ deg) and in elastic substrate ($\theta = -7.5$ deg) for three load states

Plastic zones for six of the loading states, $\xi = -1.60, -1.07, -0.551, -0.027, 0.496, 1.02$ ($KK/\sigma_0^2 L = 0.5$, $\phi = -90$ deg, -60 deg, -30 deg, 0 deg, 30 deg, 60 deg) are shown in Fig. 4. Distances are normalized by KK/σ_0^2 in accordance with (22), and the stress levels indicated in the plots are normalized by σ_0 . The computed plastic zone for $\xi = -1.60$ is identical to that determined for $\xi = 1.54$ (as demanded by (23)) and the latter is therefore not shown. The material above the bond line is elastic-plastic and thus the contour labeled by $\sigma_e = 1.0$ is the elastic-plastic boundary; the contour labeled by $\sigma_e = 1.5$ is the contour for $\sigma_e = 1.5\sigma_0$. Maximum extent of the plastic zone, R_p , varies between $0.15KK/\sigma_0^2$ (for $\xi \approx 0$) and $0.6KK/\sigma_0^2$ (for $\xi \approx \pm 1.5$). Contours in the elastic substrate has no physical significance other than being indicative of the effective stress levels. It is noteworthy that despite the significant difference in the asymptotic linear elastic fields of cracks on bimaterial interfaces and cracks in homogeneous media, the overall size and shape of the plastic zones are similar to those found for the homogeneous medium subject to combined K_I and K_{II} loading (see Shih, 1974, for a discussion of these latter fields).

Hydrostatic stress contours for the six load states just discussed are shown in Fig. 5. The stress levels indicated in the

plots are normalized by σ_0 . Positive values correspond to hydrostatic tension while negative values correspond to hydrostatic compression. The stress contours for $\xi = -1.60$ are identical to those for $\xi = 1.54$; however, the sign of the stress levels have to be changed as required by (19). It may be noted that the hydrostatic stress in materials 1 and 2 are very dependent on the load phase even in the vicinity of $\xi = 0$. For $\xi = -0.551$, the top material endures high hydrostatic tension. The top and bottom materials are subjected to high hydrostatic tension for the cases $\xi = -0.027, 0.496$.

The solutions being discussed were obtained without taking into consideration contact of the crack faces if this should occur. In Section 2, the case was made that there is a range of load states where crack face contact does not occur over any physically-significant length scale. Within that range of load combinations we have explained that the bimaterial crack problem can be analyzed as an *open* crack. Based on the elasticity solution, the range of ξ for an *open* crack (36) was determined. An estimate of the *open* crack range based on the small-scale yielding solution is now given. The displacement jump, Δu_2 , normalized by $\epsilon_0 KK/\sigma_0^2$, is plotted against $\log \bar{r}$, ($\bar{r} \equiv r/(KK/\sigma_0^2)$), in Fig. 6. Six load states, $\xi = -1.60, -1.43, -1.34, -1.07, -0.027, 1.28$ ($KK/\sigma_0^2 L = 0.5$, $\phi = -90$ deg,

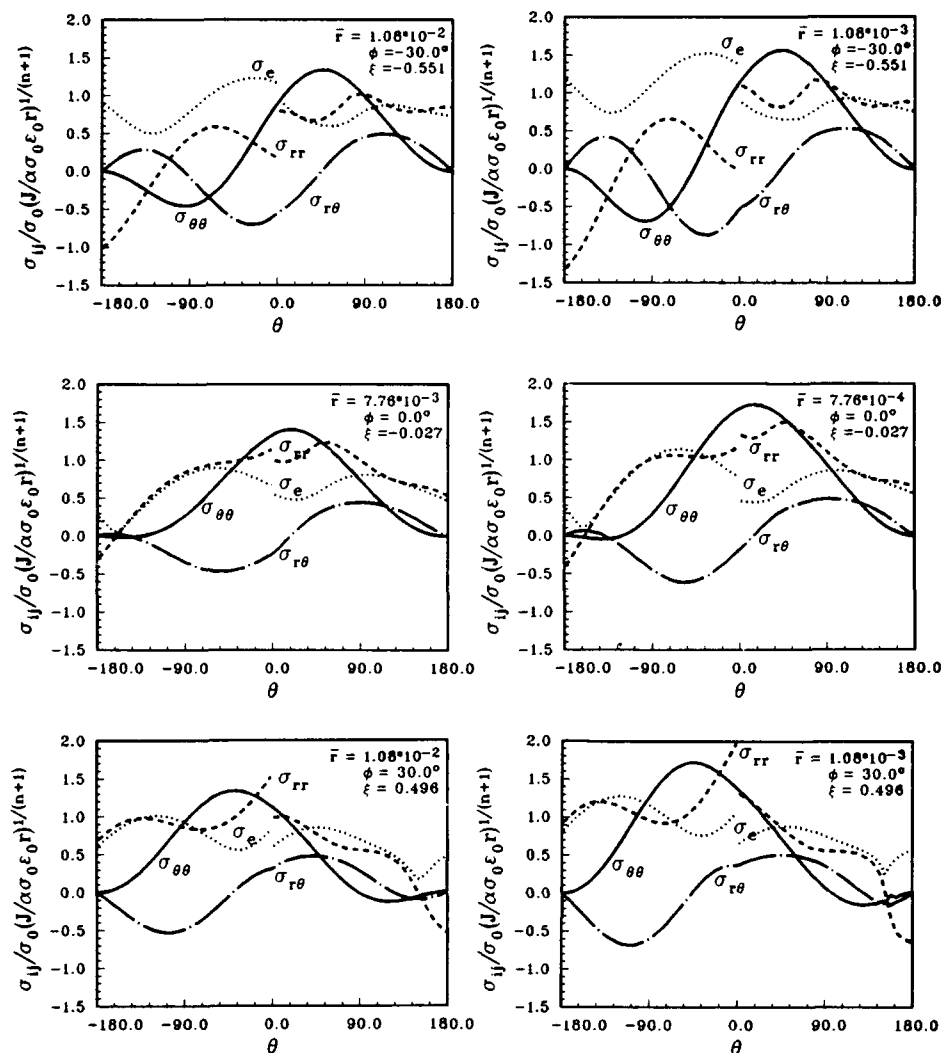


Fig. 9 Angular variation of stresses normalized by HRR form in elastic substrate ($-180 \text{ deg} \leq \theta \leq 0 \text{ deg}$) and in elastic-plastic material ($0 \text{ deg} \leq \theta \leq 180 \text{ deg}$) for three load states. For each load state, the radial distances correspond to 5 percent and 0.5 percent of the maximum plastic zone size.

-80.5 deg , -75 deg , -60 deg , 0 deg , 75 deg) are shown, and the zone of crack face contact (if any) is indicated.

In Section 2.4 a practical definition for an open crack (35) was introduced; however, values of c_1 and c_2 were not given. Appropriate values for c_1 and c_2 can be determined from plots of the plastic zone, $R_p/(\bar{K}\bar{K}/\sigma_0^2)$, varies between 0.15 to 0.6, depending on the phase ξ . Thus, a reasonable value for c_1 is 10^{-3} (this corresponds to a distance which is less than 10^{-2} of the plastic zone size), while c_2 is assigned a value much larger than unity. We examine the displacement jumps in Fig. 6. The range of ξ for which the crack is opened for distances $\bar{r} \geq 10^{-3}$ is estimated to be

$$-1.3 \leq \xi \leq 1.3. \quad (46)$$

The aforementioned estimate of the *open* crack range pertains to the particular material combination being investigated. However, crack face profiles for other material combinations have shown that the *open* crack range, when phrased in terms of ξ , is not strongly dependent on material combinations. We have completed a detailed study of an elastic-plastic material bonded onto a rigid foundation ($\epsilon \approx 0.1$). Materials charac-

terized by $n = 3, 5$, and 10 were considered. The *open* crack range differed from the range given in (46) by less than ten percent.

We have previously stated that for the present, our interest is restricted to the range of ξ in which the crack faces are not in contact. Hence, our examination of detailed behavior of the stresses is directed to load states where the crack is *open*. Stresses near the bond line are especially of interest because of the likelihood of crack propagation along the interface. The variation of stresses with radial distance from the crack tip in the elastic-plastic material (along $\theta = 7.5 \text{ deg}$) and in the elastic material (along $\theta = -7.5 \text{ deg}$) is detailed. In Fig. 7 $\log(\sigma_{ij}/\sigma_0)$ is plotted against $\log \bar{r}$ for three states of remote loads, $\xi = -0.551, -0.027, 0.496$ ($\bar{K}\bar{K}/\sigma_0^2 L = 0.5$, $\phi = -30 \text{ deg}, 0 \text{ deg}, 30 \text{ deg}$). Within distances that can be resolved by our mesh, $10^{-12} \leq \bar{r} \leq 10^3$, the crack faces are not in contact. The stresses in material 1 are shown in the left column of plots; two distinct slopes can be seen, a higher slope in the elastic region and a lower slope in the plastic region with the change in slope occurring near the elastic-plastic boundary. Plots on the right column show the stresses in material 2—similar trends are observed and it is apparent that the stress levels in the elastic material is limited by the stress levels achievable in the

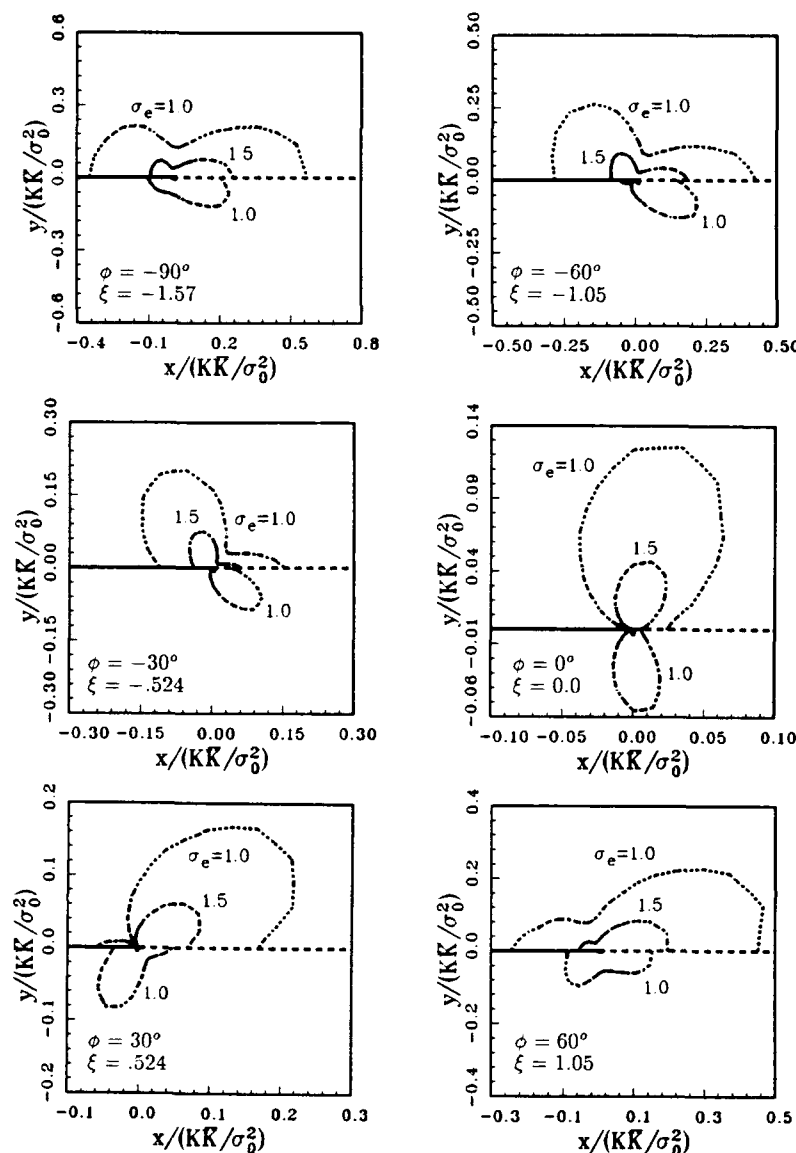


Fig. 10 (Weak) elastic-plastic material bonded onto (strong) elastic-plastic material—effective stress contours and plastic zones of six load states. Distances in the upper and lower half-planes are normalized by KK/σ_0^2 and KK/σ_0^2 , respectively.

elastic-plastic material. It may be noted that the behavior of the stresses along radial distances with other orientations (e.g., $\theta = \pm 67.7$ deg, ± 97.5 deg) are similar to those observed in Fig. 7. We should point out that the plotted stresses are the actual values evaluated at the Gauss points—no smoothing was applied to the data points in our plots of the numerically determined fields.

To examine if the actual fields are amenable to the representation given by (27), the numerically determined stresses are normalized as follows:

$$\hat{\sigma}_{ij} = \frac{\sigma_{ij}/\sigma_0}{(J/\alpha\sigma_0\epsilon_0)^{1/(n+1)}} \quad (47)$$

The plastic properties for the normalization pertain to material 1 (recall that material 2 is elastic). The variation of the normalized stresses, $\hat{\sigma}_{ij}$, with $\log \hat{r}$ is plotted in Fig. 8 for the three load states, $\xi = -0.551, -0.027, 0.496$ ($KK/\sigma_0^2 L = 0.5$, $\phi = -30$ deg, 0 deg, 30 deg). For the load states, $\xi = -0.551$ and -0.027 , the normalized stresses, $\hat{\sigma}_{ij}$, well within the plastic zone do not seem to vary with distance, i.e., the actual field support the proposed form (27) and the observation that h_{ij}

depends very weakly on distance. Consider the case $\xi = 0.496$ which displays the "strongest" variation with distance (bottom plots in Fig. 8). From Fig. 4, the maximum length of its plastic zone R_p is $0.2KK/\sigma_0^2$. Over the distances $10^{-4} < r/R_p < 10^{-1}$, which include all physically-relevant length scales, the deviation of $\hat{\sigma}_{ij}$ from its mean value is less than eight percent. It can also be seen that in every case the stress levels in the elastic substrate are set by the stresses in the elastic-plastic material (as they must by continuity of traction).

Angular variation of $\hat{\sigma}_{ij}$ at fixed radial distances equal to 5 and 0.5 percent of the maximum plastic zone size are shown in Fig. 9 for the three remote load states discussed previously. In the range -180 deg $\leq \theta \leq 0$ deg the material is elastic, while the material is elastic-plastic in the range 0 deg $\leq \theta \leq 180$ deg. For the case, $\xi = -0.551$, the hoop stress reaches its maximum in material 1. On the other hand, for $\xi = 0.496$, the hoop stress attains its maximum in material 2. In all cases, the stresses in both materials are comparable in magnitude and the normalized values are of order unity. More importantly, we point to the strong similarity of the stresses in the elastic-plastic material to the mixed-mode HRR fields for a homo-

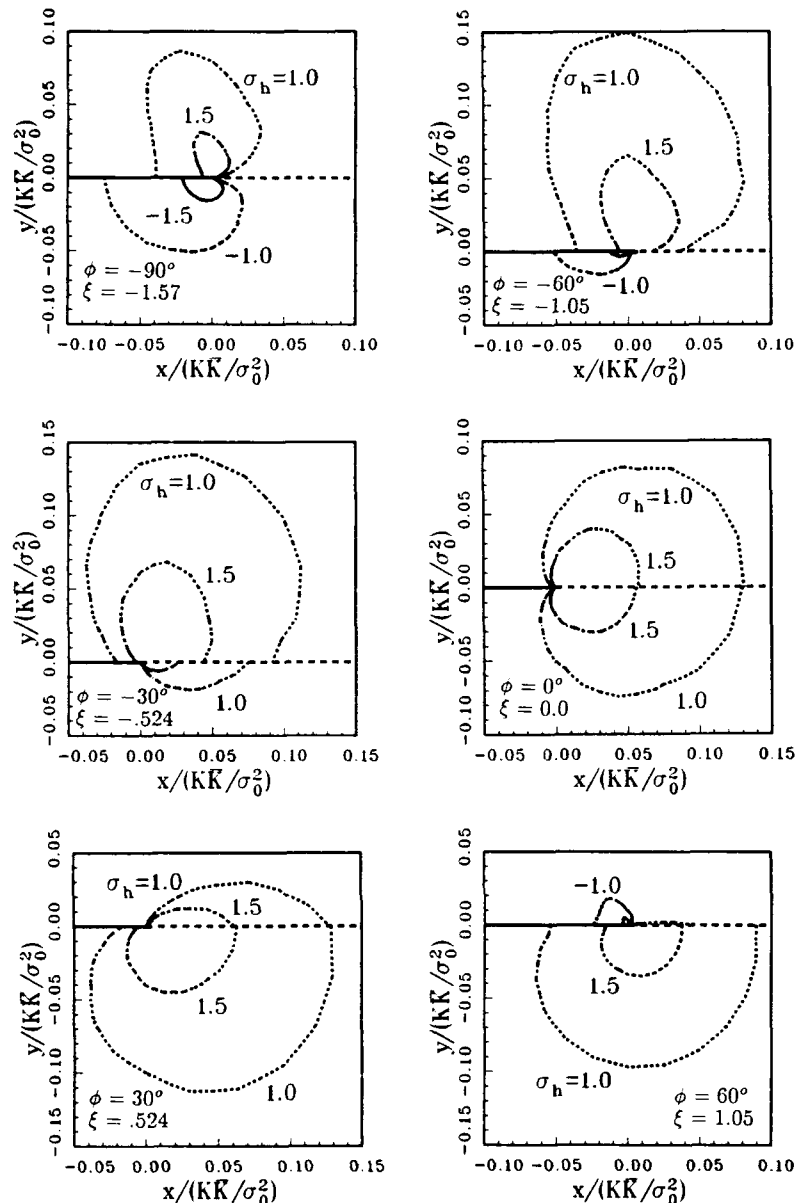


Fig. 11 (Weak) elastic-plastic material bonded onto (strong) elastic-plastic material—hydrostatic stress contours of six load states. Distances in the upper and lower half-planes are normalized by KK/σ_0^2 .

geneous medium characterized by the plastic properties of material 1. In fact, the radial and angular stress distributions in material 1 for $\xi = -0.027$ agreed closely with those for Mode I HRR fields. Stress distributions for $\xi = -0.551$ and $\xi = 0.496$ are in agreement with the mixed-mode HRR fields for $M^p = -0.95$ and $M^p = 0.78$, respectively (Symington et al., 1988). We defer the more detailed comparisons to Part III where the full field solutions in the small and finite strain regions are presented.

4.2 Two Bonded Elastic-Plastic Materials. For this analysis both materials are elastic-plastic. The elastic properties of materials 1 and 2 are identical, $E_2 = E_1$ and $\nu_1 = \nu_2 = 0.3$. Thus, Dundur's parameters $\beta_1 = \beta_2 = 0$ and ϵ also vanishes. The plastic properties of material 1 are characterized by yield stress σ_0 , strain-hardening exponent n of 5, and the material constant α equal to 0.1. Material 2 yields at σ_{02} , which is four times higher than the yield stress of material 1. The strain-

hardening exponent of material 2, n_2 , is 10 and α_2 is 0.1. The remote elastic fields are given by the standard K_I and K_{II} fields and $\xi = \phi$.

Numerical solutions were obtained for seven values of the elastic phase parameter, $\phi = -90^\circ, -60^\circ, -30^\circ, 0^\circ, 30^\circ, 60^\circ, 90^\circ$; the values of ξ are $-1.57, -1.05, -0.524, 0.0, 0.524, 1.05$, and 1.57 . J values were extracted from numerical fields using domains in which the mean radii differed by as much as nine orders of magnitude. These values agreed to better than two significant digits with the exact result (45).

Since the yield stress of material 2 is four times higher than the yield stress of material 1, the plastic zone in the (stronger) bottom material is small compared to the plastic zone in the top material. To facilitate the comparison of plastic zones in both materials, distances within material 2 are normalized by KK/σ_{02}^2 while distances within material 1 are normalized by KK/σ_0^2 . Plastic zones for six load states, $\xi = -1.57, -1.05,$

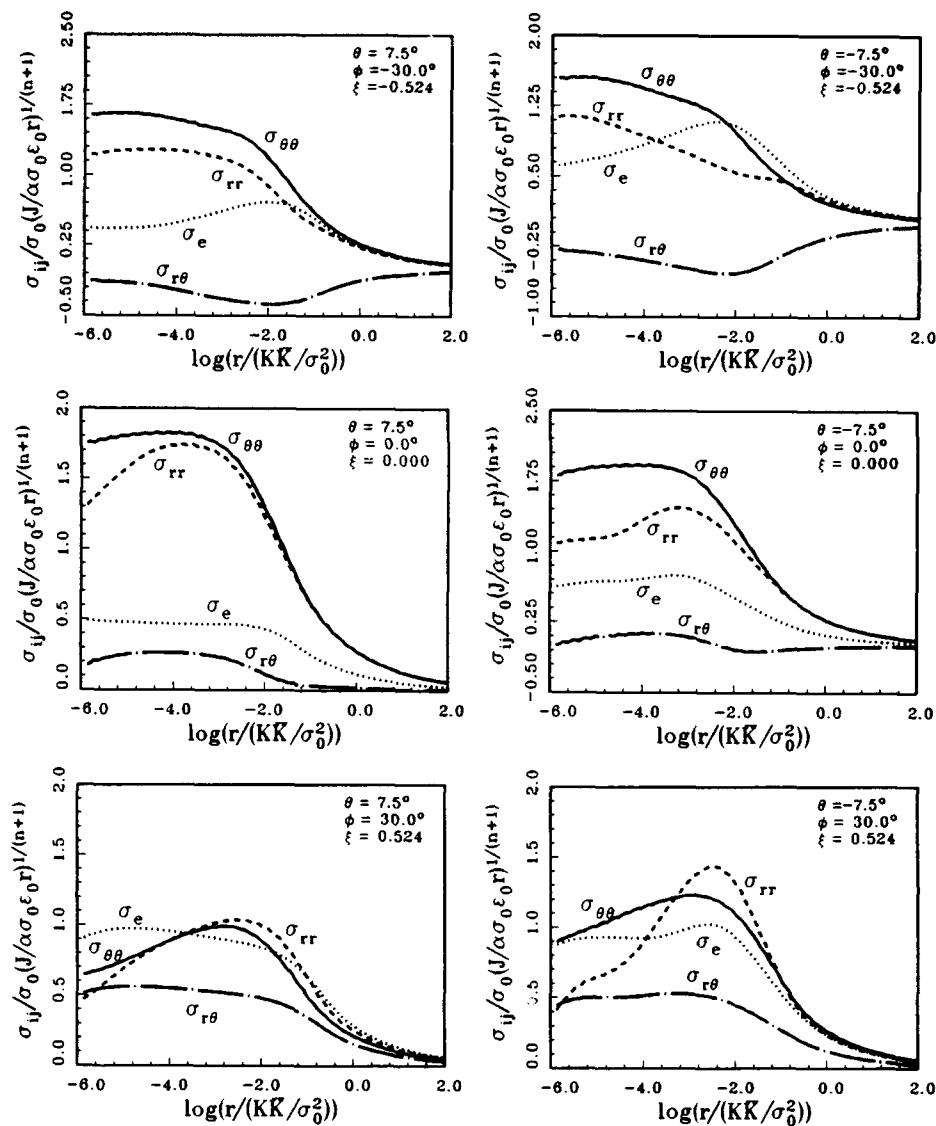


Fig. 12 Variation of normalized stresses with log of normalized distance in (weak) elastic-plastic material ($\theta = 7.5$ deg) and in (strong) elastic-plastic material ($\theta = -7.5$ deg) for three load states

$-0.524, 0.0, 0.524, 1.05$, ($\phi = -90$ deg, -60 deg, -30 deg, 0 deg, 30 deg, 60 deg) are shown in Fig. 10. (The computed plastic zone for $\xi = -1.57$ is identical to that for $\xi = 1.57$ and is not known.) The elastic-plastic boundaries in materials 1 and 2 are defined by the loci of $\sigma_e = \sigma_{01}$ and $\sigma_e = \sigma_{02}$, respectively. Since the stress levels in material 1 are normalized by σ_{01} , while those in material 2 are normalized by σ_{02} , contours labeled by $\sigma_e = 1.0$ are the elastic-plastic boundaries. The normalized plastic zone size, $R_{p1}/(KK/\sigma_{01}^2)$, for the weaker material varies between 0.15 and 0.6 and these values are rather similar to those found for the homogeneous medium subject to combined K_I and K_{II} loading (Shih, 1974). For the stronger material, $R_{p2}/(KK/\sigma_{02}^2)$ varies between 0.06 and 0.25. Thus the length of the plastic zone in the stronger material is about only 1/30 of that in the weaker material, i.e., the relative size of the plastic zones does not obey the ratio $(\sigma_{01}/\sigma_{02})^2$.

Hydrostatic stress contours for the six load states just discussed are plotted in Fig. 11. To permit a direct comparison of the stresses in both materials, the stress levels indicated in materials 1 and 2 are normalized by the same yield stress σ_{01} , and distances in both materials are normalized by the same length KK/σ_{01}^2 . The stress contours for $\xi = -1.57$ are identical

to those for $\xi = 1.57$; however, the sign of the stress levels have to be changed in accordance with (19). It is apparent that the magnitude of the hydrostatic stress in both materials vary with the load phase for moderate departures from $\xi = 0$ (compare plots for $\xi = -0.524, 0, 0.524$).

Because the plastic properties of materials 1 and 2 are different, the crack tip fields do not have a separable form of the HRR type (see discussion in Section 2). For remote load combinations in the vicinity of $\xi = \phi = \pm \pi/2$, (note that $\epsilon = 0$) our numerical results show crack face contact zones which are comparable to the size of the plastic zone. Subsequent discussions are therefore restricted to those cases where the crack faces are clearly not in contact.

Variation of the normalized stresses, $\hat{\sigma}_{ij}$, with $\log(r/(KK/\sigma_0^2))$ along $\theta = \pm 7.5$ deg, for $\xi = -0.524, 0.0, 0.524$ ($\phi = -30$ deg, 0 deg, 30 deg) is plotted in Fig. 12. The stresses in both materials are normalized by the yield stress and the hardening exponent for material 1 (the weaker material). It can be seen that the normalized stresses, $\hat{\sigma}_{ij}$, for the two states, $\xi = -0.524, 0$, are only slightly dependent on radial distance indicating that a form of the type (27) is a suitable representation over the radial distances considered in the figure. By contrast,

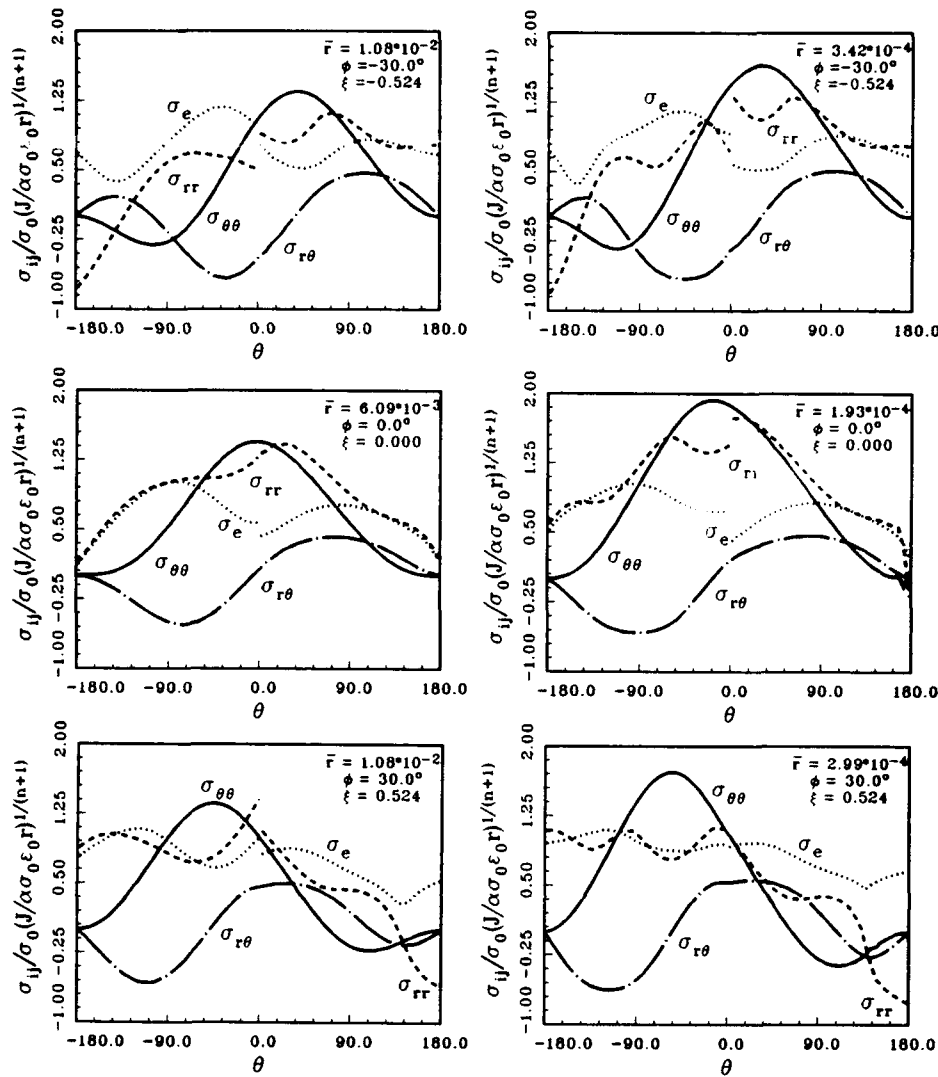


Fig. 13 Angular variation of normalized stresses in (strong) elastic-plastic material ($-180 \text{ deg} \leq \theta \leq 0 \text{ deg}$) and in (weak) elastic-plastic material ($0 \text{ deg} \leq \theta \leq 180 \text{ deg}$) for three load states. For each load state, the radial distances correspond to five percent of the maximum plastic zone size in the weak and in the strong elastic-plastic materials, respectively.

stresses normalized by the yield stress and hardening exponent for material 2 (the lower-hardening material) display stronger variation with \bar{r} over the distances considered in Fig. 12. However, over vanishingly small distances, $10^{-12} < \bar{r} < 10^{-4}$ (not shown in Fig. 12), these (latter) normalized stresses are nearly independent of \bar{r} . Such behavior is consistent with our observation that as $r \rightarrow 0$, the stresses are governed by the strain-hardening behavior of the lower-hardening material, namely, material 2 for the material system being considered. These aspects have been discussed by Shih and Asaro (1989).

The angular distribution of $\hat{\sigma}_{ij}$ (normalization based on the plastic properties of the $n = 5$ material) is plotted at two fixed radial distances for each of the load states, $\xi = -0.524, 0.0, 0.524$ ($\phi = -30 \text{ deg}, 0 \text{ deg}, 30 \text{ deg}$). The first distance is chosen to equal five percent of the maximum extent of the plastic zone in the (weaker) top material, and the other distance is chosen to equal five percent of the maximum extent of the plastic zone in the (stronger) bottom material. These angular distributions are shown in Fig. 13. For the case $\xi = -0.524$, the hoop stress reaches its maximum in material 1; it is at its maximum in material 2 for $\xi = 0.524$. It is noteworthy that the magnitude of $\hat{\sigma}_{ij}$ of both materials is of order unity. The

similarity between the angular variation of the stresses with the mixed-mode HRR fields for homogeneous medium is discussed in Part III.

5 Open Crack Range for Two Fracture Test Geometries

For arbitrary load histories, the validity of the solutions presented in this paper hinges, in part, on whether or not the crack faces make contact; if contact develops over physically-significant size scales, the solutions are invalid. We have shown that load states, where contact between the crack faces is excluded over sensible distances near and away from the crack tip, can be expressed by a range of ξ . We extend the discussion to the center-cracked-panel and confine attention to the case where the total crack length, L , is small compared to the width of the panel. Using the relation $\phi = \psi + \Theta$ in the linear elasticity prediction for an open crack (32), we observe that the right crack tip is open if ψ is in the range,

$$-\pi/2 + \Omega \leq \psi \leq \pi/2. \quad (48)$$

Both tips are open if

$$-\pi/2 + \Omega \leq \psi \leq \pi/2 - \Omega. \quad (49)$$

The open crack range under small-scale yielding is given by (46). Noting the connections $\phi = \psi + \Theta$ and $\mathbf{Q}\mathbf{Q} = \mathbf{K}\mathbf{K}$, approximating Θ by 2ϵ , and using the relation for ξ (13) in (46), we obtain

$$-1.3 - \epsilon \left(2 + \ln \frac{\mathbf{K}\mathbf{K}}{\sigma_0^2 L} \right) \leq \psi \leq 1.3 - \epsilon \left(2 + \ln \frac{\mathbf{K}\mathbf{K}}{\sigma_0^2 L} \right). \quad (50)$$

The open crack range given by (50) takes into consideration the effects of small-scale plasticity. The maximum radial extent of the plastic zone is

$$R_p = \left(\frac{1}{\gamma} \right) \frac{\mathbf{K}\mathbf{K}}{\sigma_0^2} \quad (51)$$

where γ varies between 6.5 (for $\xi \approx 0$) and 1.5 (for $\xi \approx \pm \pi/2$). Using (51) in (50) leads immediately to

$$-1.3 - \epsilon \left(2 + \ln \frac{\gamma R_p}{L} \right) \leq \psi \leq 1.3 - \epsilon \left(2 + \ln \frac{\gamma R_p}{L} \right). \quad (52)$$

Suppose the plastic zone in the center-cracked-panel is confined to a fraction of L , say, $\gamma R_p/L \approx 0.1$. According to (52), the crack tips are open if $-1.3 \leq \psi \leq 1.3$. On the other hand, the open crack range as determined by the linear elasticity solution is given by (48). Suppose that r_c/L is of order 10^{-3} and $\epsilon \approx 0.05$, then $\Omega (\equiv -\epsilon \ln(r_c/L))$ is approximately 0.3. For these values the predicted open crack range by linear elasticity is $-1.27 \leq \psi \leq \pi/2$, which is skewed about the state corresponding to pure remote tension. By contrast, crack tip plasticity results in an open crack range which is nearly symmetric about the pure tension state. Alternatively, our results indicate that states of loading corresponding to nearly remote shear may produce contact over a physically-significant size scale even with significant amounts of plastic yielding at the crack tip.

The aforementioned analysis can be extended to other specimen geometries. As an example, consider the specimen proposed by Charalambides et al. (1988) which has been analyzed by Suo and Hutchinson (1988). The beam-like specimen consists of a slender strip of thickness h which is partially bonded onto a thicker substrate. As shown by the latter authors, the specimen design is such that for a broad range of remote moment and axial loads, the loading mode at the crack tip corresponds to $\phi \approx \pi/4$ (note that the strip thickness h is the characteristic crack dimension designated by L in our formulation). To assess if the crack tip in this specimen would remain open under small-scale yielding, we use (46) in conjunction with (13) and (51) to get the following condition for an open crack:

$$-1.3 - \epsilon \ln \frac{\gamma R_p}{h} \leq \phi \leq 1.3 - \epsilon \ln \frac{\gamma R_p}{h}. \quad (53)$$

For the specimen under consideration, $\phi \approx \pi/4$, so that the condition for the crack to remain open is

$$-1.3 - \epsilon \ln \frac{\gamma R_p}{h} \leq \pi/4 \leq 1.3 - \epsilon \ln \frac{\gamma R_p}{h}. \quad (54)$$

This condition suggests that for nearly all physically reasonable values of interface fracture toughness, the crack tip would be open. For example, if $\epsilon = 0.04$ as in the case presented in Section 4.1, (54) would be violated only if $\gamma R_p/h \approx 4 \times 10^3$!

6 Concluding Remarks

In Part I, full field solutions for a complete boundary value problem were presented from which the near tip fields of interface cracks were extracted and characterized. The extent of validity of the small-scale yielding solutions in terms of the intensity of loading and resulting plastic zone size was identified for a center-cracked-panel geometry. For the most part

our results were obtained numerically, but they led nonetheless to a clear mathematical structure. In particular, it was found that a plastic phase angle, ξ defined by (28), characterizes the family of solutions for the small-scale yielding fields. In the present paper the structure of the crack tip fields under conditions of small scale yielding was explored in more detail using a boundary layer formulation.

Our numerical results show that the size of the dominant plastic zone is controlled by the yield strength of the weaker (lower yield strength) material and that over length scales comparable to the dominant plastic zone, the stress levels in both materials are set by σ_0 , the yield strength of the weaker material. Our results also show that the overall size and shape of the dominant plastic zones are similar to those found for the homogeneous medium subject to similar combined K_I and K_{II} loading (Shih, 1974).

We have observed that the form of the near tip fields is governed by the hardening characteristics of the material with the least hardening capacity. With the stress-strain behavior of both materials being given by piecewise linear elastic/power law plastic relations, our numerical solutions support an observation that as $r \rightarrow 0$, the asymptotic stress and strain fields in the lower hardening material approach those for the same material which is bonded to a rigid substrate. Indeed, the near-tip fields for the elastic-plastic material bonded to an elastic substrate (see Figs. 7, 8, and 9) are very similar to the fields presented in Part I for the same elastic-plastic material bonded to a rigid substrate. Furthermore, the present small-scale yielding solutions agreed remarkably well with the center-cracked-panel, small-scale plasticity solutions for the identical values of ξ .

For a range of ξ , the actual numerical fields appear to be nearly separable in an annular region well within the plastic zone. These near-tip fields closely resemble mixed-mode HRR fields and corroborate a proposed representation for the near-tip fields (27). Our results also show that the stresses in the higher hardening material are limited to those levels that can be attained in the lower hardening material. These aspects and the asymptotic form of near tip stress fields are elaborated upon in another publication (Shih and Asaro, 1989).

For selected geometries and three material characterizations, ($n = 5, 10, \infty$), solutions based on a small strain J_2 flow theory have recently been obtained. The plastic zones for the $n = 5$ and $n = 10$ materials and the hydrostatic stress fields are practically identical to those obtained for the corresponding deformation theory solutions. Near the interface, we did find small differences between the deformation and flow theory solutions. Away from the interface, the deformation and flow theory solutions are hardly distinguishable from one another.

Solutions which take into account finite geometry changes associated with blunting at the crack tip have also been obtained. In this case, an important length scale is the crack tip opening displacement δ_t . Within a distance of several δ_t 's ahead of the crack tip, the shear stresses near the interface are comparable to those determined by the small strain solutions, but are much smaller than the values predicted by the linear elasticity fields; in the finite strain region, the shear stresses rise slightly due to the asymmetrical blunting of the plastically deforming material. We find remarkable agreement between the full field numerical solutions and the Mode I HRR stresses over the distance $3\delta_t < r < 6\delta_t$ for tension-dominated load states, $-\pi/12 \leq \xi \leq \pi/12$. For remote load states which include moderate amounts of shear, there is good agreement between the full field solutions and the mixed-mode HRR fields, i.e., there is a range of load combinations in which the crack tip fields can be said to be characterized by J and ξ (or M^p). Furthermore, for load states in which $\sigma_{yy}^\infty > |\sigma_{xy}^\infty|$, the crack tip opens smoothly and the amount of opening scales nearly linearly with the J -integral. These aspects are discussed in Part III (Shih, Asaro, O'Dowd, 1989).

Acknowledgments

This investigation is supported by the Office of Naval Research through ONR Grant "Mechanics of Interface Cracks." The computations reported were performed on the CRAY-XMP at the Supercomputer Facility of the U.S. Naval Research Laboratory and on the Alliant Computer at the Computational Mechanics Facility of Brown University. The acquisition of the Alliant was made possible by grants from the U.S. National Science Foundation (Grant DMR-8714665), and the Office of Naval Research (Grant N00014-88-K-0119) and matching funds from Brown University.

References

- Achenbach, J. D., Keer, L. M., Khetan, R. P., and Chen, S. H., 1979, "Loss of Adhesion at the Tip of an Interface Crack," *Journal of Elasticity*, Vol. 9, pp. 397-409.
- Atkinson, C., 1981, "The Interface Crack with a Contact Zone (The Crack of Finite Length)," *International Journal of Fracture*, Vol. 19, pp. 131-138.
- Charalambides, P. G., Lund, J., Evans, A. G., and McMeeking, R. M., 1988, "A Test Specimen for Determining the Fracture Resistance of Bimaterial Interfaces," in press.
- Cherepanov, G. P., 1962, "The Stress State in a Heterogeneous Plate with Slits," (in Russian), *Izvestia AN SSSR, OTN, Mekhan. i Mashin.*, Vol. 1, pp. 131-137.
- Comninou, M., 1977a, "The Interface Crack," *ASME JOURNAL OF APPLIED MECHANICS*, Vol. 44, pp. 631-636.
- Comninou, M., 1977b, "Interface Crack with Friction in the Contact Zone," *ASME JOURNAL OF APPLIED MECHANICS*, Vol. 44, pp. 780-781.
- Comninou, M., and Schmueser, D., 1978, "The Interface Crack in a Combined Tension-Compression and Shear Field," *ASME JOURNAL OF APPLIED MECHANICS*, Vol. 46, pp. 345-348.
- Dundurs, J., 1969, "Edge-bonded Dissimilar Orthogonal Elastic Wedges Under Normal and Shear Loading," *ASME JOURNAL OF APPLIED MECHANICS*, Vol. 36, pp. 650-652.
- England, A. H., 1965, "A Crack Between Dissimilar Media," *ASME JOURNAL OF APPLIED MECHANICS*, Vol. 32, pp. 400-402.
- Erdogan, F., 1965, "Stress Distribution in Bonded Dissimilar Materials with Cracks," *ASME JOURNAL OF APPLIED MECHANICS*, Vol. 32, pp. 403-410.
- Eshelby, J. D., 1965, "The Continuum Theory of Lattice Defects," *Solid State Physics*, Vol. 3, Seitz and Turnbull, eds., pp. 79-144.
- Hughes, T. J. R., 1980, "Generalization of Selective Integration Procedures to Anisotropic and Nonlinear Materials," *International Journal for Numerical Methods in Engineering*, Vol. 15, pp. 1413-1418.
- Hutchinson, J. W., 1968, "Singular Behavior at the End of a Tensile Crack in a Hardening Material," *Journal of the Mechanics and Physics of Solids*, Vol. 16, pp. 13-31.
- Hutchinson, J. W., 1983, "Fundamentals of the Phenomenological Theory of Nonlinear Fracture Mechanics," *ASME JOURNAL OF APPLIED MECHANICS*, Vol. 50, pp. 1042-1051.
- Hutchinson, J. W., Mear, M., and Rice, J. R., 1987, "Crack Parallelizing an Interface between Dissimilar Materials," *ASME JOURNAL OF APPLIED MECHANICS*, Vol. 54, pp. 828-832.
- Knowles, J. K., and Sternberg, E., 1983, "Large Deformations Near a Tip of an Interface-Crack Between Two Neo-Hookean Sheets," *Journal of Elasticity*, Vol. 13, pp. 257-293.
- Malyshev, B. M., and Saigalik, R. L., 1965, "The Strength of Adhesive Joints using the Theory of Cracks," *International Journal of Fracture Mechanics*, Vol. 1, pp. 114-128.
- Moran, B., and Shih, C. F., 1987, "Crack Tip and Associated Domain Integrals from Momentum and Energy Balance," *Engineering Fracture Mechanics*, Vol. 27, pp. 615-642.
- Needleman, A., 1987, "A Continuum Model for Void Nucleation by Inclusion Debonding," *ASME JOURNAL OF APPLIED MECHANICS*, Vol. 54, pp. 525-531.
- Ortiz, M., and Blume, J. A., 1988, "Effect of Decohesion and Sliding on Bimaterial Crack-Tip Fields," Brown University Report, submitted for publication.
- Park, J. H., and Earmme, Y. Y., 1986, "Application of Conservation Integrals to Interfacial Crack Problems," *Mechanics of Materials*, Vol. 5, pp. 261-276.
- Rice, J. R., 1968, "A Path Independent Integral and the Approximate Analysis of Strain Concentration by Notches and Cracks," *ASME JOURNAL OF APPLIED MECHANICS*, Vol. 35, pp. 379-386.
- Rice, J. R., 1988, "Elastic Fracture Mechanics Concepts for Interfacial Cracks," *ASME JOURNAL OF APPLIED MECHANICS*, Vol. 55, pp. 98-103.
- Rice, J. R., and Rosengren, G. F., 1968, "Plane Strain Deformation Near a Crack Tip in a Power Law Hardening Material," *Journal of the Mechanics and Physics of Solids*, Vol. 16, pp. 1-12.
- Rice, J. R., and Sih, G. C., 1965, "Plane Problems of Cracks in Dissimilar Media," *ASME JOURNAL OF APPLIED MECHANICS*, Vol. 32, pp. 418-423.
- Shih, C. F., 1974, "Small-Scale Yielding Analysis of Mixed Plane-Strain Crack Problems," in *Fracture Analysis*, ASTM STP 560, pp. 187-210.
- Shih, C. F., and Needleman, A., 1984, "Fully Plastic Crack Problems: Part I—Solutions by a Penalty Method," *ASME JOURNAL OF APPLIED MECHANICS*, Vol. 51, pp. 48-56.
- Shih, C. F., and Asaro, R. J., 1988, "Elastic-Plastic Analysis of Cracks on Bimaterial Interfaces: Part I—Small Scale Yielding," *ASME JOURNAL OF APPLIED MECHANICS*, Vol. 55, pp. 299-316.
- Shih, C. F., and Asaro, R. J., 1989, "Elastic-Plastic and Asymptotic Fields of Interface Cracks," *International Journal of Fracture*, in press.
- Shih, C. F., Asaro, R. J., and O'Dowd, N. P., 1989, "Elastic-Plastic Analysis of Cracks on Bimaterial Interfaces: Part III—Finite Deformation and Large Scale Yielding Studies," in preparation.
- Symington, M., Shih, C. F., and Ortiz, M., 1988, "Tables of Plane Strain Mixed-Mode Plastic Crack Tip Fields," Brown University Report, MRG/DMR-8714665/1.
- Suo, Z., and Hutchinson, J. W., 1988, "Interface Crack between two Elastic Layers," Harvard University Report, Mech-118, to be published.
- Ting, T. C., 1986, "Explicit Solution and Invariance of the Singularities at an Interface Crack in Anisotropic Composites," *International Journal of Solids and Structures*, Vol. 22, pp. 965-983.
- Williams, M. L., 1959, "The Stresses Around a Fault or Crack in Dissimilar Media," *Bulletin of the Seismological Society of America*, Vol. 49, pp. 199-204.
- Willis, J. R., 1971, "Fracture Mechanics of Interfacial Cracks," *Journal of the Mechanics and Physics of Solids*, Vol. 19, pp. 353-368.
- Zywicz, E., and Parks, D. M., 1989, "Elastic Yield Zone around an Interfacial Crack Tip," *ASME JOURNAL OF APPLIED MECHANICS*, Vol. 56, pp. 577-584.

Failure of Bimaterial Interfaces

A. G. VARIAS and N. P. O'DOWD

Division of Engineering, Brown University, Providence, RI 02912 (U.S.A.)

R. J. ASARO

Department of Applied Mechanics and Engineering Science, University of California, San Diego, La Jolla, CA 92093 (U.S.A.)

C. F. SHIH

Division of Engineering, Brown University, Providence, RI 02912 (U.S.A.)

(Received April 21, 1989)

Abstract

The failure of bimaterial interfaces with periodic arrays of cracks or flaws is examined. An adhesive relation is prescribed for the interface which governs the normal and shear stress vs. normal and shear displacement response. These relations provide what amounts to a constitutive law for a thin interface layer which is envisaged to undergo a rupture process when subjected to combined tensile and shear forces. On the basis of these models, we examine the effect of geometry and interfacial properties on the fields of propagating cracks and flaws as well as on the ductility, toughness and failure modes of bimaterial interfaces. Both crystal plasticity and J_2 flow theory are used to model the plastic deformation of the materials on either side of the interface. In both descriptions, full account is taken of finite changes in geometry, large plastic strains and material strain rate sensitivity. Within the context of our adhesive models the interface properties are essentially described by three parameters, namely the interface strength σ_{\max} , the interface normal separation δ_c beyond which all adhesion is lost and the work φ_0 of pure tensile de-adhesion; these three are related through relations of the form $\varphi_0 = A\sigma_{\max}\delta_c$, where A depends on the particular functional form of the adhesive relations. Our results, performed for metals with only modest rate sensitivities, demonstrate the pivotal role that the value of the interface strength has in establishing the mechanisms of interface failure and, thereby, the toughness and ductility of the microstructures containing the interface. In addition, the effects of crack and flaw size on the stress-strain fields, and failure modes,

that develop at flawed interfaces are studied in a series of calculations involving flaw sizes in the range $15 \leq a_0/\delta_c \leq 1500$.

1. Introduction

Our previous work on interface failure has been concerned with detailed analyses of the mechanics of interface cracks, and in particular with the analysis of the stress and deformation fields at the tips of cracks lying on dissimilar material interfaces. Both asymptotic and full field analyses have been carried out, and from these the essential structure of the crack tip fields has been clarified. These analyses have assumed, however, that the interfaces possess infinite strength and thus were intended to provide a comprehensive picture of stress and strain fields at, and near, imperfect interfaces at stages leading up to crack growth. In the present work, analyses of interface debonding due to the propagation of flaws and cracks (*i.e.* long flaws) are carried out using an adhesive model for the interface which is also used in the work of Varias *et al.* [1] and McHugh *et al.* [2]. This adhesive model is motivated by the atomistic calculations of Rose *et al.* [3]. The adhesive relations in effect prescribe a separate constitutive relation for the interface which can be used to model the effects of interface structure and chemistry on bonding. These adhesive laws are phenomenological in nature and are meant to be able to describe the influence of interface strength, as affected by structure and chemistry, on the overall strength, ductility and toughness of microstructures.

In what follows, solutions for the elastic-plastic fields and growth of periodic distributions of interface cracks and flaws are presented. These defects are taken to be completely non-bonded segments of the interface whose dimensions are defined relative to the parameter δ_c which in the adhesive model measures the separation across the interface beyond which adhesion is completely lost. δ_c (or like parameters that enter the adhesive force laws) introduces physical length scales into the microstructural models that impart different behaviors to flaws of different sizes. For cases where defect lengths are large compared with δ_c , i.e. for cracks, the elastic-plastic fields are compared with those for stationary cracks as provided by Shih and Asaro [4-6]. When the defect lengths are only multiples of $(10-100)\delta_c$, however, the fields that develop at the flaw tips, and the mechanics of debonding, can be quite different from those for cracks. Details for both types of defect are presented in what follows.

For the specific cases presented here, the interface separates an elastic-plastic material and a rigid substrate; the crack tip field analyses of Shih and Asaro [4-6] have shown, however, that this provides a very good model for the case of an elastic substrate as well. Remote loading is essentially tensile and corresponds to remotely applied displacements normal to the plane of the interface. Cases are presented where finite-strain-rate-dependent J_2 flow theory and a more physically based crystal plasticity theory are used to model the behavior of the plastically deformable material. In both cases, full account is taken of finite strain and geometry change effects. All the analyses presented here are two dimensional and correspond to states of plane strain.

Within our adhesive laws, the interface is characterized by three parameters: σ_{\max} , the maximum pure tensile strength of the interface; δ_c , defined above; φ_0 , the work expended in completely separating the interface. These parameters are directly related via $\varphi_0 = A\sigma_{\max}\delta_c$, where the value of the constant A depends on the particular functional form of the adhesive laws. Our calculations indicate that σ_{\max} tends to dominate the interface behavior and thereby determines the mode of interface failure and the resulting toughness or ductility. δ_c and φ_0 themselves play important roles but these generally have a quantitative significance rather than the pivotal qualitative role that the σ_{\max} level has.

Examples are shown of the separation of flawed interfaces, where σ_{\max} controls the interface failure mode, which, in turn, strongly affects ductility; δ_c and φ_0 have significant roles in setting the values of strains at which failure occurs and thus the precise values of ductility. Other examples involving long cracks are presented, which demonstrate the role that σ_{\max} plays in establishing the value of toughness; these examples include the calculation of resistance curves for crack growth that illustrate the strong dependence of the J integral vs. crack extension relation on the value of σ_{\max} . It should be noted, however, that, although our material constitutive relations are strain rate dependent, the rate sensitivities are prescribed to be rather low, consistent with what is the case for f.c.c. metals deformed quasi-statically at near room temperature. The significance of this is that for rate-independent materials it is well known that continuum fields that develop at crack tips are self-similar; this, in turn, means that the maximum stress levels that develop ahead of the cracks are constant and are fixed in magnitude by the material's strain hardening properties and yield strength. It is then expected that interface failure will largely depend on achieving the stress levels, within the matrix, necessary to overcome the interface's strength. The interface strength is thus expected to dominate the failure behavior. Further details on the relationship of the adhesive properties to the mechanics of interface failure are described in Appendix A, which considers a simple example of a uniform block, subjected to one-dimensional tension, debonding from a rigid substrate. This analysis provides useful insight for interpreting our results on the failure of flawed interfaces presented in Sections 4 and 5.

The plan of the paper is as follows. In the next section, theoretical, numerical and modeling issues are discussed. In Section 3 the boundary value problem of an imperfect interface is described. In Section 4 the results for growing cracks and flaws on intercrystalline interfaces, i.e. where the deformable material is modeled using crystal plasticity, are described. In Section 5 the results for interface failure using J_2 flow theory are presented; these will include correlation of the elastic-plastic fields of growing cracks and flaws with those for stationary cracks as found by Shih and Asaro [4-6]. Section 6 contains discussion and conclusions. Finally, in Appendix A a solution to a simple boundary value problem of a

perfectly bonded interface is presented. This provides insight into the mechanics of the de-adhesion process.

Standard tensor notation is used throughout. Bold italic serif symbols are used to denote vectors and bold italic sans serif symbols to denote tensors, the orders of which will be clear in context. Products are indicated with dots and products containing no dots are dyadic products. Italic indices range from one to the number of spatial dimensions and repeated italic indices are always summed. Inverses, transposes and transposed inverses are denoted with a superscript -1 , T and $-T$ respectively, and superposed dots indicate differentiation with respect to time t . For instance,

$$\begin{aligned} \mathbf{A} \cdot \mathbf{B} &= A_{ik} B_{kj} \mathbf{b}_i \mathbf{b}_j & \mathbf{A} : \mathbf{B} &= A_{ik} B_{ik} \\ cd &= c_i c_i \mathbf{b}_i \mathbf{b}_i & \mathbf{c} \cdot \mathbf{d} &= c_i d_i \\ \mathbf{H} : \mathbf{A} &= H_{ijk} A_{ijk} \mathbf{b}_i \mathbf{b}_j \mathbf{b}_k & \mathbf{A} : \mathbf{H} &= A_{ijk} H_{ijk} \mathbf{b}_i \mathbf{b}_j \mathbf{b}_k \\ \dot{\mathbf{B}} &= \frac{\partial B_{ij}}{\partial t} \mathbf{b}_i \mathbf{b}_j & \mathbf{B} \cdot \mathbf{c} &= B_{ik} c_k \mathbf{b}_i \end{aligned}$$

where the base vectors \mathbf{b}_i are cartesian and independent of time. Greek indices are slip system identifiers and range from one to the number of available slip systems.

2. Theoretical and numerical considerations

2.1. Material constitutive relations

For both J_2 flow theory and the crystal plasticity theory used herein, the deformation gradient is taken to be multiplicatively decomposable into elastic and plastic parts, via

$$\mathbf{F} = \frac{\partial \mathbf{x}}{\partial \mathbf{X}} = \mathbf{F}^* \cdot \mathbf{F}^p \quad (1)$$

where \mathbf{x} is the current position of a material particle and \mathbf{X} is its position in a reference state. \mathbf{F}^p is the deformation due solely to the plastic flow and represents the aggregate effect of, for example, dislocation motion in a ductile crystalline material, which leaves the lattice structure unchanged. \mathbf{F}^* is the remaining contribution to \mathbf{F} associated with lattice distortion and any rigid rotation of the lattice and the material. For both theories, the kinematics in (1) lead to a velocity gradient of the form

$$\begin{aligned} \mathbf{L} &= \dot{\mathbf{F}} \cdot \mathbf{F}^{-1} \\ &= \dot{\mathbf{F}}^* \cdot (\mathbf{F}^*)^{-1} + \mathbf{F}^* \cdot \dot{\mathbf{F}}^p \cdot (\mathbf{F}^p)^{-1} \cdot (\mathbf{F}^*)^{-1} \end{aligned} \quad (2)$$

This leads to plastic and elastic parts of the rates of deformation \mathbf{D} and spin \mathbf{W} given by

$$\begin{aligned} \mathbf{D} &= \text{sym}(\mathbf{L}) \\ &= \mathbf{D}^p + \mathbf{D}^* \end{aligned}$$

and

$$\begin{aligned} \mathbf{W} &= \text{skew}(\mathbf{L}) \\ &= \mathbf{W}^p + \mathbf{W}^* \end{aligned}$$

The specific flow relations which describe crystalline plasticity and J_2 flow theory were developed, in detail, by Asaro [7] and Harren *et al.* [8] for the crystal theory used here, and by Moran *et al.* [9] for the J_2 flow theory. With these references in mind, only a brief statement of the material parameters used in the calculations presented here are given in Sections 2.1.1 and 2.1.2.

2.1.1. The crystal plasticity model

In crystal plasticity, plastic flow is assumed to occur by slip along discrete sets of crystallographic slip systems. Figure 1 shows the slip systems used in the present study of the de-adhesion problems: \mathbf{a}_i are the time-independent cartesian base vectors aligned with the crystal lattice in the reference configuration. These slip systems correspond to a two-dimensional close-packed lattice. Each slip system is defined in the reference configuration by its unit crystallo-

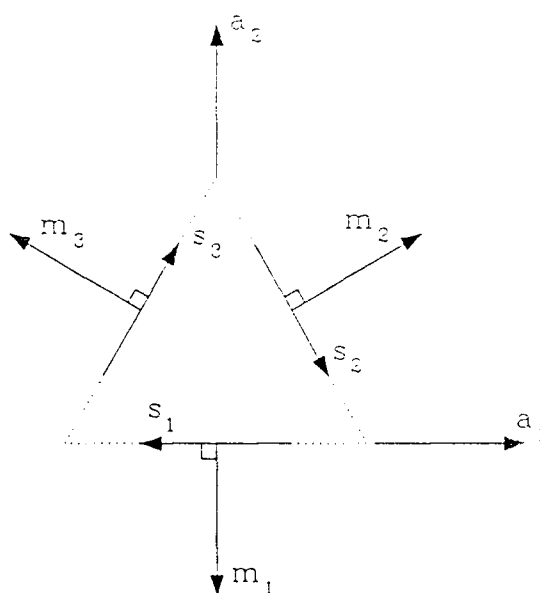


Fig. 1. Slip systems of a two-dimensional close-packed crystal. The lattice base vector \mathbf{a}_1 is parallel to the interface in the reference configuration.

graphic normal $m_{(a)}$, and a unit crystallographic slip direction lying in the slip plane $s_{(a)}$. With $\dot{\gamma}_{(a)}$ being the rate of shear on that system, the plastic part of the velocity gradient in (2) is given by

$$L^P = \dot{F}^P \cdot F^{P-1} \\ = \sum_a \dot{\gamma}_{(a)} s_{(a)} m_{(a)} \quad (3)$$

Here the sum is over all available slip systems and is explicitly indicated.

In our strain-rate-dependent formulation, the rate of shearing on each slip system is given as a function of the current state of stress and material state. The particular form used here is the adaptation of the Schmid rule, described by Asaro [7], i.e.

$$\dot{\gamma}_{(a)} = \dot{a}_{(a)} \operatorname{sgn}(\tau_{(a)}) \left(\frac{|\tau_{(a)}|}{g_{(a)}} \right)^{1/m} \quad (4)$$

where $\tau_{(a)} = s_{(a)}^* \cdot \tau \cdot m_{(a)}^*$ is the current value of the resolved shear stress. The Kirchhoff stress is given by $\tau = (\det F) \sigma$ where σ is the Cauchy stress and $s_{(a)}^* = F^* \cdot s_{(a)}$, $m_{(a)}^* = m_{(a)} \cdot (F^*)^{-1}$. $g_{(a)}$ is the current value of the slip system hardness, m is the rate sensitivity exponent and $\dot{a}_{(a)} > 0$ is a reference shear rate. The hardness of a particular slip system $g_{(a)}$ is obtained by the path-dependent integration of the evolution equation

$$\dot{g}_{(a)} = \sum_{\beta} h_{a\beta}(\dot{\gamma}_{\beta}) |\dot{\gamma}_{\beta}| \quad \gamma_a = \int_0^t \sum_{\alpha} |\dot{\gamma}_{\alpha}| dt \quad (5)$$

where $h_{a\beta}$ is a matrix of (non-negative) hardening moduli, which account for self-hardening and latent hardening among the slip systems, and γ_a is the accumulated slip. The initial condition for this evolution is specified as $g_{(a)}(\gamma_a = 0) = g_0$.

The strain-hardening function $h_{a\beta}$ is given by

$$h_{a\beta}(\dot{\gamma}_{\beta}) = \frac{dg(\gamma_{\beta})}{d\gamma_{\beta}} q_{a\beta} \quad (6a)$$

where

$$g(\gamma_a) = g_0 + h_{\infty} \gamma_a + (g_{\infty} - g_0) \tanh \left\{ \gamma_a \left(\frac{h_0 - h_{\infty}}{g_{\infty} - g_0} \right) \right\} \quad (6b)$$

Here h_0 and h_{∞} are the initial and asymptotic rate of hardening respectively. g_0 is the initial slip system hardness, and g_{∞} can be interpreted as the

saturation hardness when $h_{\infty} = 0$. $q_{a\beta}$ is a matrix of latent hardening ratios, taken to conform to Taylor's isotropic hardening model, i.e. $q_{a\beta} = 1$ for all α and β . The material parameters were determined by matching the relation (6b) to actual data for a copper single crystal [10]. The values are $h_0/g_0 = 3.5$, $g_{\infty}/g_0 = 1.55$ and $h_{\infty}/g_0 = 1$. We have also assumed that $\dot{a}_{(a)} = 10^{-3} s^{-1}$ and $m = 0.005$ which are fairly representative values for the range of quasi-static strain rates considered in this paper.

The description of the single crystal's constitutive behavior is completed by a specification of its elastic response, which is expressed in terms of the Green strain of the lattice given by $E^* = \frac{1}{2} \{ (F^*)^T \cdot F^* - I \}$ and the lattice-based second Piola-Kirchhoff stress $S^* = (F^*)^{-1} \cdot \tau \cdot (F^*)^{-T}$. The elastic response may be denoted as $S_{ij}^* = (\partial \Phi / \partial E_{ij}^*)$, where $S^* = S_{ij}^* a_i a_j$, $E^* = E_{ij}^* a_i a_j$, and $\Phi = \Phi(E_{ij}^*)$ is the Helmholtz potential energy of the lattice per unit reference volume. In rate form the elasticity relations are

$$\dot{S}^* = K : \dot{E}^* \\ K = K_{ijkl} a_i a_j a_k a_l \\ K_{ijkl} = \frac{\partial^2 \Phi}{\partial E_{ij}^* \partial E_{kl}^*} \quad (7)$$

In this study, the elastic potential Φ is taken as

$$\Phi = \frac{1}{2} \lambda_0 (E_{11}^* + E_{22}^*)^2 + \mu_0 (E_{11}^{*2} + E_{22}^{*2}) \\ + \frac{1}{2} \mu_0 (E_{12}^* + E_{21}^*)^2 \quad (8)$$

where the Lamé constants have the values $\lambda_0 = 2172.43 g_0$ and $\mu_0 = 993.83 g_0$.

Combining the kinematical relations contained in (1)-(3), we get

$$\dot{E}^* = (F^P)^{-T} \cdot \dot{E} \cdot (F^P)^{-1} - \sum_a \dot{\gamma}_{(a)} A_{(a)} \quad (9)$$

where

$$A_{(a)} = \operatorname{sym} \{ (F^*)^T \cdot F^* \cdot s_{(a)} m_{(a)} \} \quad (10)$$

and \dot{E} is the rate of the total Green strain $E = \frac{1}{2} (F^T \cdot F - I)$.

Making use of $S^* = F^P \cdot S \cdot (F^P)^T$, where $S = F^{-1} \cdot \tau \cdot F^{-T}$ is the second Piola-Kirchhoff stress on the undeformed configuration, and (3), we get

$$\dot{S}^* = F^P \cdot \dot{S} \cdot (F^P)^T + 2 \sum_a \dot{\gamma}_{(a)} B_{(a)} \quad (11)$$

where

$$B_{(a)} = \text{sym}(s_{(a)} m_{(a)} \cdot S^*) \quad (12)$$

Combining eqns. (7), (9) and (11) we obtain the complete constitutive relation in terms of E and S :

$$\dot{S} = L : \dot{E} - \sum_a \dot{\gamma}_{(a)} X_{(a)} \quad (13)$$

where

$$L = (F_{ik}^p)^{-1} (F_{jp}^p)^{-1} K_{klpq} (F_{rp}^p)^{-1} (F_{nq}^p)^{-1} a_i a_j a_r a_n \quad (14)$$

and

$$X_{(a)} = (F^p)^{-1} \cdot (K : A_{(a)} + 2B_{(a)}) \cdot (F^p)^{-T} \quad (15)$$

2.1.2. J_2 flow theory

Although phenomenological in nature, J_2 flow theory can be formulated along similar lines to the physical crystal theory described above. For isotropic polycrystals, it is assumed that the average value of the plastic spin W^{*p} among the individual grains vanishes, i.e. $W^{*p} = 0$. The flow rule for $D^{*p} = \text{sym}\{\dot{F}^p \cdot (F^p)^{-1}\}$ is taken to be

$$D^{*p} = \dot{\epsilon}^p \text{sym}(R^*) \quad (16a)$$

where

$$R^* = \frac{3}{2\bar{\sigma}} C^* \cdot S^{*'} \cdot C^* \quad (16b)$$

$\dot{\epsilon}^p$ is the effective plastic strain rate given by a flow law with strain hardening, and $S^{*'}$ is the deviatoric part of S^* defined by $S^{*' = S^* - \frac{1}{3}(S^* : C^*)(C^*)^{-1}}$. The effective stress $\bar{\sigma}$ is defined as

$$\bar{\sigma}^2 = \frac{3}{2} (S^{*' \cdot C^*}) : (S^{*' \cdot C^*})$$

In the present work, power law material strain rate sensitivity and strain hardening were assumed in the form

$$\dot{\epsilon}^p = \begin{cases} \dot{\epsilon}_0 \left[\left\{ \frac{\bar{\sigma}}{H(\bar{\epsilon}^p)} \right\}^{1/m} - 1 \right] & \bar{\sigma} \geq H(\bar{\epsilon}^p) \\ 0 & \bar{\sigma} \leq H(\bar{\epsilon}^p) \end{cases} \quad (17)$$

We assume that $H(\bar{\epsilon}^p)$ evolves according to an isotropic hardening relation

$$H(\bar{\epsilon}^p) = \sigma_0 \left(1 + \frac{\bar{\epsilon}^p}{\epsilon_0} \right)^{1/n} \quad (18)$$

where n is a hardening exponent, σ_0 is a reference stress, $\epsilon_0 (= \sigma_0/E)$ and $\dot{\epsilon}_0$ are a reference strain and strain rate respectively and m is the rate-sensitivity exponent. In this study, we have used $n = 5$ and $m = 0.005$.

The elastic response is formulated in terms of a hyperelastic potential defined on the intermediate configuration $W^*(C^*)$, where C^* is the elastic right Cauchy-Green tensor, $C^* = (F^*)^T \cdot F^*$. The intermediate configuration is thus obtained by applying the mapping F^p to the undeformed state. Thus S^* is given by

$$S^* = 2 \frac{\partial W^*}{\partial C^*} \equiv S^*(C^*) \quad (19)$$

and the elasticity tensor is given by the relation

$$K = 2 \frac{\partial S^*}{\partial C^*} = 4 \frac{\partial^2 W^*}{\partial C^* \partial C^*} \quad (20)$$

The elastic potential used is for a neo-hookean isotropic elastic material extended into the compressible range [11] and is given by

$$W^* = U(F^*) + \frac{\mu_0}{2} \text{tr}(C^*) \quad (21)$$

where $F^* = \det F^*$.

The function U represents the extension into the compressible range and is taken to be

$$U(F^*) = \frac{1}{2} \lambda_0 (\log F^*)^2 - \mu_0 \log F^* \quad (22)$$

Combining (19), (21) and (22), we obtain

$$S^* = \lambda_0 \log(F^*) (C^*)^{-1} + \mu_0 \{I - (C^*)^{-1}\} \quad (23)$$

The above relation reduces to Hooke's law with Lamé constants λ_0 and μ_0 , when the limit of infinitesimal strains is considered. In this study $\lambda_0 = 218.9\sigma_0$, and $\mu_0 = 112.8\sigma_0$, corresponding to Young's modulus E of $300\sigma_0$ and Poisson's ratio ν of 0.33.

2.2. The adhesive model

2.2.1. General considerations

The adhesive model used in the present work is motivated by the *ab initio* calculations of Rose *et al.* [3] and Ferrante and Smith [12]. These have led to a universal adhesive relation for bimetallic interfaces. They have found a scaled relation between the energy and interfacial separation of the form

$$E = -\Delta E (1 + \delta^*) \exp(-\delta^*) \quad (24)$$

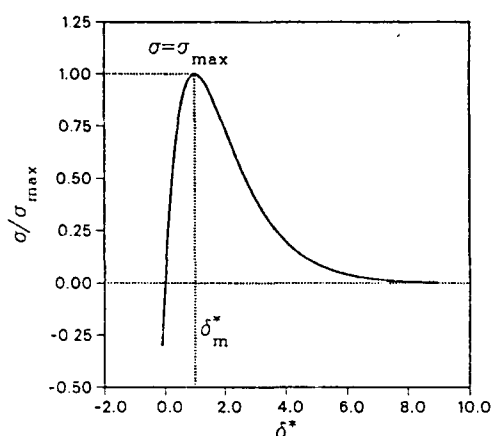


Fig. 2. Diagram of adhesive traction vs. interface displacement in the case of pure tensile straining.

where ΔE is the equilibrium adhesive energy, $\delta^* \equiv (\delta - \delta_{eq})/l$, δ and δ_{eq} are the actual and equilibrium interface separations respectively, and l is a scaling length, defined so that the second derivative of the scaled energy-distance curve is unity at equilibrium. When (24) is differentiated with respect to the interface separation a force-separation (per unit area of interface) relation of the form

$$\sigma_n = E_0 \frac{\delta_n}{\delta_{eq}} \exp\left(-\frac{\beta \delta_n}{\delta_{eq}}\right) \quad (25)$$

results. $E_0 \equiv \beta \Delta E/l$ is an initial modulus for one-dimensional tensile straining of the interface, $\beta = \delta_{eq}/l$ where l is of the order of the electronic screening length, and $\delta_n \equiv \delta - \delta_{eq}$.

The interface stress vs. separation relation is shown in Fig. 2 where several parameters of interest are illustrated. For example, the maximum stress attained from eqn. (25) is $\sigma_{max} = E_0(\beta e)^{-1}$. Still another important quantity obtained from (25) is the work of interfacial de-adhesion φ_0 , obtained by calculating the work to separate fully the interface, *i.e.*

$$\begin{aligned} \varphi_0 &= \int_0^\infty \sigma_n d\delta_n \\ &= \frac{E_0 \delta_{eq}}{\beta^2} \\ &= \frac{\sigma_{max}^2 \delta_{eq} e^2}{E_0} \\ &= \frac{\sigma_{max} \delta_{eq}}{\beta/e} \end{aligned} \quad (26)$$

The numerology is such that σ_{max} is of the order of a tenth of the elastic moduli; for example, if there is no initial interface, $E_0 \approx (1 + \nu)E$ where ν is Poisson's ratio and E is Young's modulus. In the more general case, φ_0 represents the work of creating two surfaces minus that which was needed to create the initial interface.

To explore the applicability of the above to a fracture theory further, it is instructive to apply it to one of the many adhesive models proposed for crack propagation in nominally elastic materials, as has been done by Rice and Wang [13]. Such models, *e.g.* those proposed by Dugdale [14], Barenblatt [15], or Bilby *et al.* [16], consider cracks in homogeneous elastic media which open smoothly at their tips under the action of restraining adhesive forces. Generally a force-displacement relation of the form shown in Fig. 2 is assumed. The elastic crack tip singular field is replaced by the adhesive zone whose length w is estimated to be

$$\begin{aligned} w &\approx \frac{\pi}{8(1-\nu^2)} \frac{E\varphi_0}{\sigma_{max}^2} \\ &\approx \frac{E\varphi_0}{2\sigma_{max}^2} \end{aligned} \quad (27)$$

Then, if the above relations for σ_{max} and φ_0 are substituted in (27), we obtain $w \approx (e^2/2)(E/E_0) \times \delta_{eq} \approx 3.7(E/E_0)\delta_{eq}$. If we now apply this to a homogeneous medium where $E_0 = (1 + \nu)E \approx 1.33E$ (with $\nu = 1/3$), we obtain $w \approx 2.8\delta_{eq}$ which is just a few atomic distances or so. For cases involving interface cracks, E/E_0 may be larger than unity as suggested by the work of Rice and Wang and the adhesive zone may be larger.

The specific intent here is to explore the implications of an adhesive theory such as outlined above to the fracture of interfaces when the materials on either side of the interface undergo arbitrary amounts of plastic deformation. In other words, we seek a continuum analog to the result in (25) which may be implemented within the framework of a continuum elastic-plastic description.

For this purpose we recall the experiments of Argon and coworkers [17, 18] and of Cialone and Asaro [19] which were concerned with estimating the critical interfacial stresses required to separate iron (ferrite)-Fe₃C interfaces. Conditions of general plasticity prevailed in the ductile iron matrices and the scale of observation (by scan-

ning electron microscopy) was typically of order $0.05 \mu\text{m}$ or so. When displacements of the ferrite from the carbide surface of some fraction of this resolution was observed, debonding was said to have occurred. Estimates of the average normal tensile stresses, i.e. those prevailing over the size scales of fractions of a micrometer, required to cause this were $3\sigma_0 \leq \sigma_{\text{crit}} \leq 4\sigma_0$, where σ_0 is the matrix yield strength. Within the context of atomistic studies, δ_{eq} is in the range $(3-4) \times 10^{-10} \text{ m}$. For continuum analysis of the kind considered in this investigation an appropriate value for δ_{eq} is of the order of $0.01 \mu\text{m}$, i.e. 10^{-8} m . To give the same work of separation, the resulting value for σ_{max} for a proposed continuum adhesion model is roughly 10^{-2} of that associated with the atomistic model. As a fraction of E_0 , σ_{max} is $3E_0/100\beta e$, which is approximately equal to $E_0/300$. This value is, in fact, a reasonable estimate of the yield strength of the ferrite matrices.

The picture then in our continuum analog is that of a thin atomistic layer, of order 100–200 Å thick that undergoes a rupture process involving normal displacements of 100 Å or so. Since inelastic processes are expected to occur within this layer, φ_0 should now be taken several times larger than the work required to create free surfaces. The cleavage energy of ferrite has been estimated to be about three to four times the interface bonding energy. Therefore, σ_{max} can be adjusted upwards to $3\sigma_0 \leq \sigma_{\text{max}} \leq 4\sigma_0$. This phenomenological version of the adhesive law is thus consistent with the experimental observations noted above.

We adopt the above model to describe continuum separation of interfaces and, in the example calculations to follow, the parameters σ_{max} and δ_{eq} take on values in the ranges quoted above. Further theoretical studies concerned with the atomistics of interface separation will hopefully provide further insight into the details of such laws as will experiment aimed at comparing the predictions of interface separation obtained from these models with observation. Two phenomenological versions of continuum separation relations are presented next.

2.2.2. Continuum adhesive relations

The adhesive Cauchy tractions are governed by relations of the type

$$\sigma_n = \begin{cases} F(\delta_n, \delta_t) & \text{if } \delta_n < \delta_c \\ 0 & \text{if } \delta_n \geq \delta_c \end{cases} \quad (28)$$

$$\sigma_t = \begin{cases} G(\delta_n, \delta_t) & \text{if } \delta_n < \delta_c \\ 0 & \text{if } \delta_n \geq \delta_c \end{cases} \quad (29)$$

where σ_n and δ_n are the normal traction and displacement, and σ_t and δ_t are the tangential traction and displacement defined with respect to the mean surface as shown in Fig. 3. δ_c serves as a critical normal separation beyond which all adhesion is lost. Thus the condition $\delta_n/\delta_c = 1$ provides a criterion for defining the current flaw tip position in the analyses of crack growth in the subsequent sections. For the type of interface described above, δ_c can be taken to be about $0.02 \mu\text{m}$. The function F attains its maximum value, designated by σ_{max} , at a value of δ_n within the interval $(0, \delta_c)$. Therefore the interface strength σ_{max} is the maximum normal traction that the interface can sustain. When $\delta_t = 0$, the variation in σ_n vs. δ_n is similar to that shown in Fig. 2.

We now use (24) to motivate a continuum adhesive relation for the normal tractions. To this end we restate the relation (24) in the form

$$\varphi = -A(1 + \eta\delta_n) \exp(-\eta\delta_n) \quad (30)$$

The relation between the normal stress and normal displacement given by $\sigma_n = A\eta^2\delta_n \times \exp(-\eta\delta_n)$ is derived by differentiating φ of (30) with respect to δ_n . The maximum stress occurs at $\delta_n = 1/\eta$ and it has the value $\sigma_{\text{max}} = A\eta/e$. It should be noted that the work of separation by

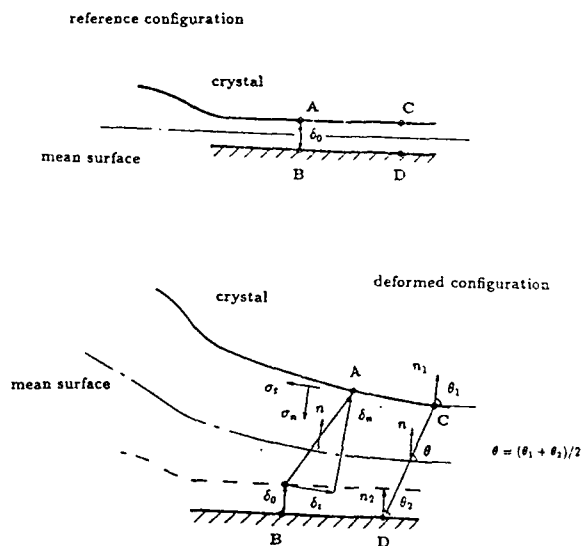


Fig. 3. Interface de-adhesion model for a deformable material bonded to a rigid substrate. ---, position of material interface boundary in the reference configuration. The de-adhesion process zone has initial thickness δ_0 , which is comparable with δ_c .

tension alone which has been defined in (26) is given by $\varphi_0 = e\sigma_{\max}/\eta$. In terms of the present parameters an equivalent expression for the normal stress is

$$\sigma_n = \frac{e^2 \sigma_{\max}^2}{\varphi_0} \delta_n \exp\left(-\frac{e\sigma_{\max}}{\varphi_0} \delta_n\right) \quad (31)$$

A phenomenological relation for the shear stresses which is consistent with (29) is given by

$$\sigma_t = \frac{e^2 \sigma_{\max}^2}{\varphi_0} \delta_t \left(1 - \frac{\delta_n}{\delta_c}\right) \quad (32)$$

where δ_c is defined as the normal displacement at which the work of separation under pure tension is equal to 95% of φ_0 . This is a practical definition of a characteristic length for total loss of adhesion which is consistent with the polynomial adhesive relation to be defined next. It should be noted that (32) has been scaled so that the initial shear stiffness is identical with the initial tensile stiffness in (31).

An alternative phenomenological form of a continuum adhesive relation can be obtained by expressing the functions F and G as polynomials in δ_n and δ_t . One version of such a relation is

$$F(\delta_n, \delta_t) = \frac{27}{4} \sigma_{\max} \frac{\delta_n}{\delta_c} \left\{ 1 - 2 \frac{\delta_n}{\delta_c} + \left(\frac{\delta_n}{\delta_c}\right)^2 \right\} + \frac{27}{4} \sigma_{\max} \left(\frac{\delta_t}{\delta_c}\right)^2 \left(-1 + \frac{\delta_n}{\delta_c} \right) \quad (33)$$

$$G(\delta_n, \delta_t) = \frac{27}{4} \sigma_{\max} \frac{\delta_t}{\delta_c} \left\{ 1 - 2 \frac{\delta_n}{\delta_c} + \left(\frac{\delta_n}{\delta_c}\right)^2 \right\} \quad (34)$$

As in the previous relations both F and G vanish for values of δ_n greater than δ_c . For the form in (33), F is maximum at $\delta_n = \delta_c/3$ and $\delta_t = 0$, i.e.

$$\sigma_{\max} = F\left(\frac{\delta_c}{3}, 0\right)$$

When $\delta_t = 0$ throughout the process of de-adhesion, the work of de-adhesion is simply given by

$$\varphi_0 = \frac{9}{16} \sigma_{\max} \delta_c$$

Equations (33) and (34), when interpreted as the nominal tractions, are those used by Needleman [20] for void nucleation.

The flaw and crack geometries considered in

this paper are loaded in remote tractions which are normal to the interface. Our detailed calculations show that the amount of interface shearing displacement is small compared with the normal displacement so that the actual work of de-adhesion is nearly equal to φ_0 which is the work of interfacial separation by tension alone.

2.3. Finite element implementation

2.3.1. Crystal plasticity

The rate constitutive relation (13) is implemented via the one-step explicit rate tangent method of Pierce *et al.* [21]. The time discrete form of the relations that result from the algorithm is

$$\mathbf{S}^t = \mathbf{L}^{\tan} : \dot{\mathbf{E}}^t - \dot{\mathbf{X}}^{\tan} \quad (35)$$

where \mathbf{L}^{\tan} and $\dot{\mathbf{X}}^{\tan}$ are determined explicitly from the state at time t .

To enforce equilibrium at the end of the time step $t + \Delta t$, the principle of virtual work is written in the reference configuration, i.e.

$$\int_V \mathbf{n}^{t+\Delta t} : \delta \mathbf{F} dV = \int_{S_t + S} \mathbf{t}^{t+\Delta t} \cdot \delta \mathbf{u} dS \quad (36)$$

Here, V is the reference volume, S_t is the boundary surface between the adjoining crystals where adhesive tractions are applied and S is the regular boundary over which tractions are imposed. $\mathbf{t} = \mathbf{N} \cdot \mathbf{n}$ is the nominal traction vector (\mathbf{N} is the outward unit normal to crystal surface), $\mathbf{n} = \mathbf{F}^{-1} \cdot \boldsymbol{\tau} = \mathbf{S} \cdot \mathbf{F}^T$ is the nominal stress and $\delta \mathbf{u}$ is an admissible variational displacement field that is compatible with the variational deformation gradient field $\delta \mathbf{F}$. The explicit difference relation $\mathbf{n}^{t+\Delta t} = \mathbf{n}^t + \dot{\mathbf{n}}^t \Delta t$ as well as

$$\mathbf{n}^t : \delta \mathbf{F} = \mathbf{S}^t : \delta \mathbf{E} \quad \delta \mathbf{E} = \text{sym}\{(\mathbf{F}^t)^T \cdot \delta \mathbf{F}\} \quad (37)$$

$$\dot{\mathbf{n}}^t : \delta \mathbf{F} = \dot{\mathbf{S}}^t : \delta \mathbf{E} + \{\mathbf{S}^t \cdot (\dot{\mathbf{F}}^t)^T\} : \delta \mathbf{F} \quad (38)$$

is substituted into (36) to obtain

$$\begin{aligned} & \int_V [\delta \mathbf{E} : \mathbf{L}^{\tan} : \dot{\mathbf{E}}^t + \{\mathbf{S}^t \cdot (\dot{\mathbf{F}}^t)^T\} : \delta \mathbf{F}] dV \\ & = \int_V \left(\dot{\mathbf{X}}^{\tan} - \frac{1}{\Delta t} \mathbf{S}^t \right) : \delta \mathbf{E} dV + \frac{1}{\Delta t} \int_{S_t + S} \mathbf{t}^{t+\Delta t} \cdot \delta \mathbf{u} dS \end{aligned} \quad (39)$$

The adhesive relations are given in terms of Cauchy tractions. In terms of Cauchy tractions

the integral over S_i is

$$\begin{aligned} \int_{S_i} \mathbf{t}^{t+\Delta t} \cdot \delta \mathbf{u} \, dS &= \int_{S_i^{t+\Delta t}} \boldsymbol{\sigma}^{t+\Delta t} \cdot \delta \mathbf{u} \, dS \\ &= \int_{S_i} \boldsymbol{\sigma}^t \cdot \delta \mathbf{u} \, dS + \frac{\partial}{\partial t} \left(\int_{S_i} \boldsymbol{\sigma}^t \cdot \delta \mathbf{u} \, dS \right) \Delta t \\ &= I_1 + I_2 \end{aligned} \quad (40)$$

where $\boldsymbol{\sigma}^t$ are the Cauchy tractions acting on the interface at time t , S_i^t in the current configuration. It should be noticed that, differentiating the last integral, one must take into account the change in the interface with respect to time. The I_1 term is what commonly describes the tractions acting on the crystal boundary. The term I_2 introduces new coefficients of the nodal velocities for the interface nodes, due to the dependence of the adhesive traction rates and the surface variation on the nodal velocities. It is therefore added to the global stiffness matrix, which is derived by the usual procedure. The time-discrete variational equation is written in cartesian index form on the reference orthonormal base vectors \mathbf{e}_i , which in this problem coincide with the lattice base vectors \mathbf{a}_i . Then the usual finite element interpolation and gradient operators are introduced to obtain a linear system of equations. After applying the appropriate rate boundary conditions and solving the resulting linear system of equations, the state at time t is updated to time $t + \Delta t$ in a manner that is consistent with the method of Pierce *et al.* The spatial discretization is accomplished by using quadrilateral elements which are made up of four cross-triangles.

2.3.2. J_2 flow theory

The starting point for the implementation adopted here is (36). Using the standard finite element discretization we get a system of nonlinear equations for the deformation mapping. This system of equations is solved using a Newton-Raphson iteration. The algorithm is explicit in the plastic flow direction \mathbf{R}^* and hardening moduli \mathbf{H} which remain fixed throughout the increment but fully implicit in the increment of effective plastic strain $\Delta \bar{\epsilon}^p$. The consistent tangent used in the Newton-Raphson procedure follows from linearization of (36) with respect to the deformation mapping. The linearized

equation is

$$\begin{aligned} \int_V \{ \mathcal{D} : \nabla_0^T(\Delta \mathbf{u}) \} : \delta \mathbf{F} \, dV + \int_{S_i} (\nabla \mathbf{t}^{t+\Delta t} \cdot \Delta \mathbf{u}) \cdot \delta \mathbf{u} \, dS \\ = \int_{S+S_i} \mathbf{t}^{t+\Delta t} \cdot \delta \mathbf{u} \, dS - \int_V \mathbf{n}^{t+\Delta t} : \delta \mathbf{F} \, dV \end{aligned} \quad (41)$$

Here $\Delta \mathbf{u}$ are the incremental displacements, ∇_0 is the gradient with respect to undeformed coordinates and ∇ represents the spatial gradient. \mathcal{D} is used to denote the gradient of \mathbf{n} with respect to \mathbf{F} at $t + \Delta t$, i.e.

$$\mathcal{D}(\mathbf{F}^{t+\Delta t}) = \frac{\partial \mathbf{n}^{t+\Delta t}}{\partial \mathbf{F}^{t+\Delta t}} \quad (42)$$

The first term on the left-hand side of (41) gives the usual contribution to the stiffness matrix. \mathcal{D} plays the role of an effective elastic-plastic tangent on the reference configuration. Full details on the derivation of the elastic-plastic tangents are given in Moran *et al.* [9]. The second term on the left-hand side takes into account the dependence of the interface tractions on the deformation through (33) and (34). As discussed earlier, the adhesive relation is expressed in terms of the Cauchy traction; so the second integral on the left-hand side of (41) is rewritten as

$$\begin{aligned} \int_{S_i} (\nabla \mathbf{t}^{t+\Delta t} \cdot \Delta \mathbf{u}) \cdot \delta \mathbf{u} \, dS \\ = \int_{S_i} \left\{ \nabla \left(\frac{|d\mathbf{x}|}{|d\mathbf{X}|} \boldsymbol{\sigma}^{t+\Delta t} \right) \cdot \Delta \mathbf{u} \right\} \cdot \delta \mathbf{u} \, dS \end{aligned} \quad (43)$$

where $\boldsymbol{\sigma}$ is the adhesive Cauchy traction, and $|d\mathbf{x}|/|d\mathbf{X}|$ is the ratio of the current arc length to the original length. This additional stiffness term, due to the interface tractions, can be obtained in closed form and is added to the usual stiffness matrix.

In this implementation the body is discretized using four node isoparametric elements. Numerical difficulties may be encountered with this element for nearly incompressible deformations. To overcome these numerical difficulties, we use an assumed strain method which is essentially a generalization of Hughes [22], \bar{B} method to finite deformations. The deformation gradient \mathbf{F} is decomposed into volumetric and deviatoric parts

$$\mathbf{F} = \mathbf{F}^{\text{vol}} \mathbf{F}^{\text{dev}} = \mathbf{F}^{\text{dev}} \mathbf{F}^{\text{vol}}$$

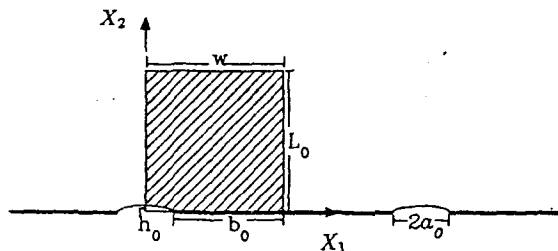


Fig. 4. A periodic array of flaws lying on an interface between a deformable body and a rigid substrate. Because of the conditions of periodicity and symmetry, only the shaded part of the body is required for the analysis.

where

$$F^{vol} = F^{1/3} I \quad F^{dev} = F^{-1/3} F$$

The volumetric part F of the deformation gradient \mathbf{F} is then extrapolated from the reduced quadrature points. The resulting volumetric deformation field incorporates fewer deformation modes and the element performs well in the presence of near incompressibility.

3. Model boundary value problems

Figure 4 depicts the geometry of the periodic array of cracks and flaws. Meshes spanning up to six orders of magnitude in mesh size were used to resolve the elastic-plastic fields at the tips of flaws and cracks and along the interface. Symmetry, along with the constraint of the rigid substrate, leads to the boundary conditions, $\dot{u}_1 = 0$ on $X_1 = 0$ and $X_1 = w$, corresponding to uniaxial straining in the X_2 direction. On the top boundary, i.e. $X_2 = L_0$, \dot{u}_2 is prescribed. The crack or flaw face is traction free whereas, on the interface, tractions are prescribed in accordance with (31) and (32) or (33) and (34). The shear tractions are taken equal to zero on the sides $X_1 = 0$ and $X_1 = w$ and on the top boundary $X_2 = L_0$. These geometry and boundary conditions lead to very high triaxial stress states as the deformation progresses into the fully yielded regime. Since deformation and stress fields near notch tips are strongly affected by triaxial stress states, this aspect of the boundary value problem must be kept in mind.

Three types of defect are considered: long flaws, $a_0/\delta_c \approx 1500$, which behave like cracks; short flaws where $a_0/\delta_c \approx 15$; intermediate-size flaws where $a_0/\delta_c \approx 150$. Most of our analyses are carried out for these three ratios and some additional results are presented for short flaws with

$a_0/\delta_c < 50$. In all cases examined, the ratio a_0/b_0 of the initial flaw length to the initial ligament is fixed at $\frac{1}{2}$, and the block height L_0 is $1.25 b_0$.

To provide perspective for the subsequent discussions, we note that for a long flaw there exists an annular zone near the flaw tip in which the stress and deformation state are controlled by an asymptotic crack tip field. Specifically the effects of load and crack geometry on the deformation within this annular zone are transmitted through the stress intensity factor K when non-linear effects at the crack tip are confined to a fraction of its length. Under so-called contained or large-scale plasticity, these effects are transmitted by the J integral. In this context, we speak of an autonomous K - or J -dominated crack tip zone where the asymptotic fields are a good approximation to the actual fields over distances that extend approximately $0.05a_0$ – $0.1a_0$. In other words, a flaw can be treated as a crack if the fracture process zone (or δ_c in this work) is embedded within the annular K - or J -dominated zone. Specifically, flaws of the type $a_0/\delta_c \approx 1500$ turn out to behave like cracks. On the contrary, flaws where $a_0/\delta_c \approx 15$ cannot be treated as cracks since δ_c is not small compared with the size of the K - or J -dominated zone. For flaws characterized by $a_0/\delta_c \approx 150$ the behavior depends upon the strength of the interface and on the sharpness of the flaw's tip during its growth.

Calculations were performed using both the exponential and the polynomial phenomenological adhesive relations described above. Most of what is described in the following, however, are results obtained using the polynomial relation in (33) and (34).

Figure 5 is a representative mesh of a crack-like flaw. Two types of notch geometry are employed: an elliptical notch tip (Fig. 5(a)) and a circular notch tip (Fig. 5(b)). A representative mesh of short flaws is shown in Fig. 6. The bulk of our results are for flaws having elliptical tips although selected results for flaws with rounded notch tips are also discussed.

4. Results using crystal plasticity theory

4.1. Long flaws

The ratio a_0/h_0 of the initial flaw length to its opening for the crack geometry (i.e. long flaw) is 500. The ratio of the flaw length to the separation length δ_c is approximately 1500. Analyses were

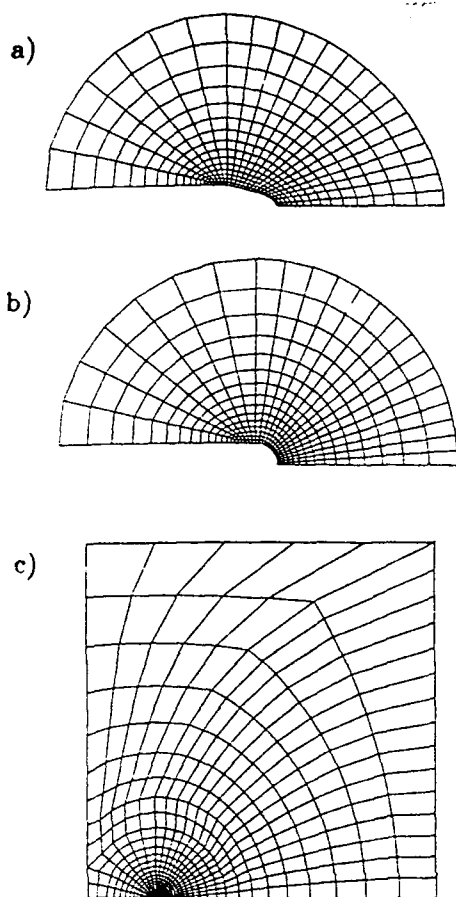


Fig. 5. Finite element meshes used in the study of interfaces containing long or intermediate-size flaws ($a_0/\delta_c \approx 1500$ or 150): (a) notch with elliptical tip; (b) notch with circular tip; (c) remote mesh.

performed for interface strength σ_{\max} of $5g_0$, $6g_0$ and $7g_0$.

For all three levels of interfacial strength, the process of de-adhesion begins at the notch tip and continues as the remote load increases; the remote load is indicated by the level of remote tensile stress σ^∞ . This failure mode for all three cases of σ_{\max} is shown in Figs. 7(a), 7(b) and 7(c), where the interface profiles are presented at various levels of remote nominal stress defined as the total applied load divided by the reference cross-sectional area. The interface displacements increase rapidly as the distance to the crack tip decreases. From this plot, we locate the current crack tip, as noted previously, by the position where the normal opening displacement equals δ_c . For the same load states, the distribution of the normal stress along the interface is shown in Figs. 7(d), 7(e) and 7(f). The stresses increase

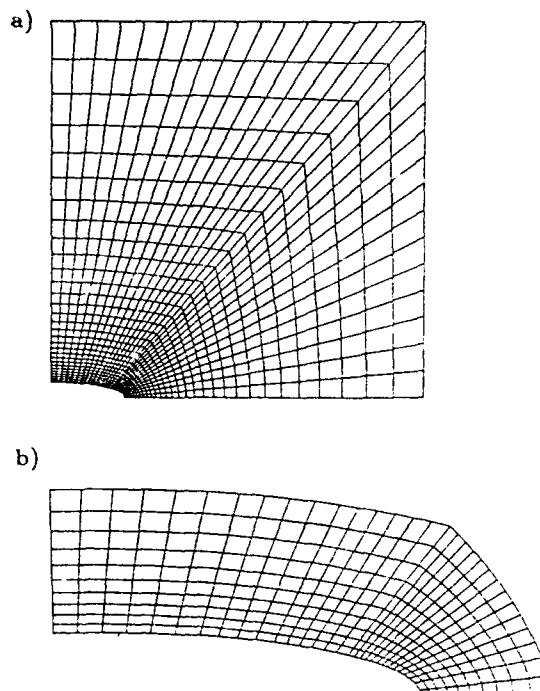


Fig. 6. Finite element mesh used in the study of interfaces with short flaws ($a_0/\delta_c < 50$): (a) remote mesh; (b) near-tip mesh.

rapidly as the distance to the crack tip decreases and attain a maximum at a distance in excess of $10\delta_c$ ahead of the current notch tip. At closer distances, the stresses decrease very rapidly and vanish in the debonded interface. As the crack advances, the zone of peak stress translates with the crack tip; however, the high stress gradient associated with the initial process of crack growth begins to weaken. This behavior has a ready explanation. A weaker stress gradient is a well-known consequence of crack growth [23] and the process of crack growth can only be maintained by the attainment of a peak stress of σ_{\max} as required by the adhesive relation. It is apparent from our results in Fig. 7 that higher stress gradients develop along the stronger interface. The effect of σ_{\max} on stress gradient is clearly shown in Fig. 8(a), where the stress distribution for approximately the same amount of crack growth and normalized by the respective σ_{\max} is plotted. From this and preceding plots, it is apparent that a high normal stress extends over a larger zone as the strength of the interface decreases. The hydrostatic stress along the interface behaves in a similar manner and it is not plotted. The deformed notch tip and the interface profile are

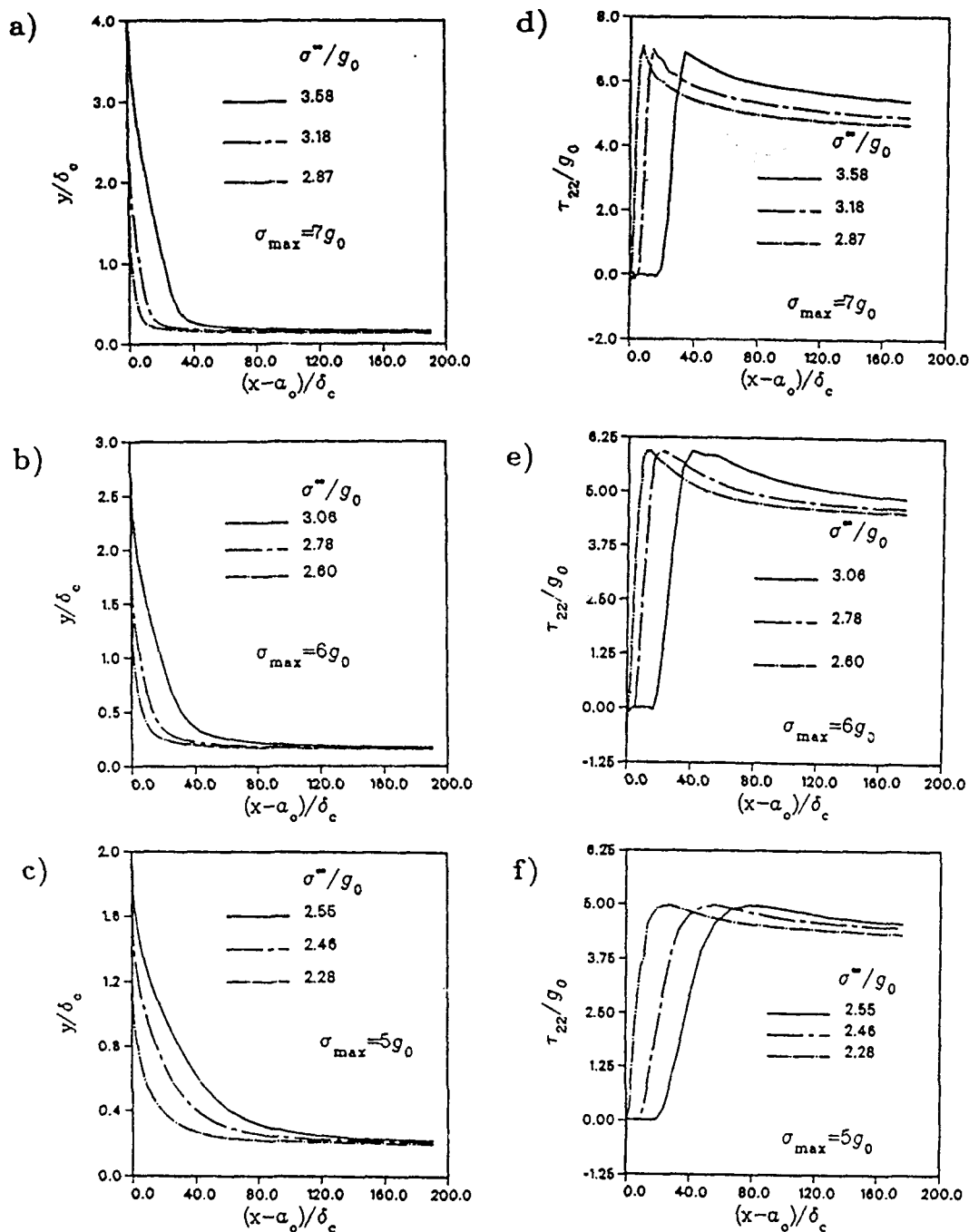


Fig. 7. Interface profiles and τ_{22} Kirchhoff stress distributions along the interface for $a_0/\delta_c \approx 1500$. (x, y) are the cartesian coordinates measured with respect to the reference coordinate system depicted in Fig. 4.

shown in Fig. 8(b); it can be seen that the interface displacement gradient also decreases with decreasing interface strength.

The accumulated slip γ_a is also strongly dependent on the interface strength. This can be

seen by the contour of the accumulated slip at $\gamma_a = 0.001$ shown in Fig. 9(a) for the three different σ_{max} values and at the same amount of crack growth ($\Delta a \approx 20\delta_c$). The region enclosed by the contour ($\gamma_a = 0.001$) is effectively the plastic zone;

Fig. 8
interf
interf
crack

the p
the p
stre
slip
slip
notch
growth
growth
comp
less
growth
with
the p
for ex
0.4 f
 $\sigma_{max} =$
 $\sigma_{th} = 4$
and 7
amount

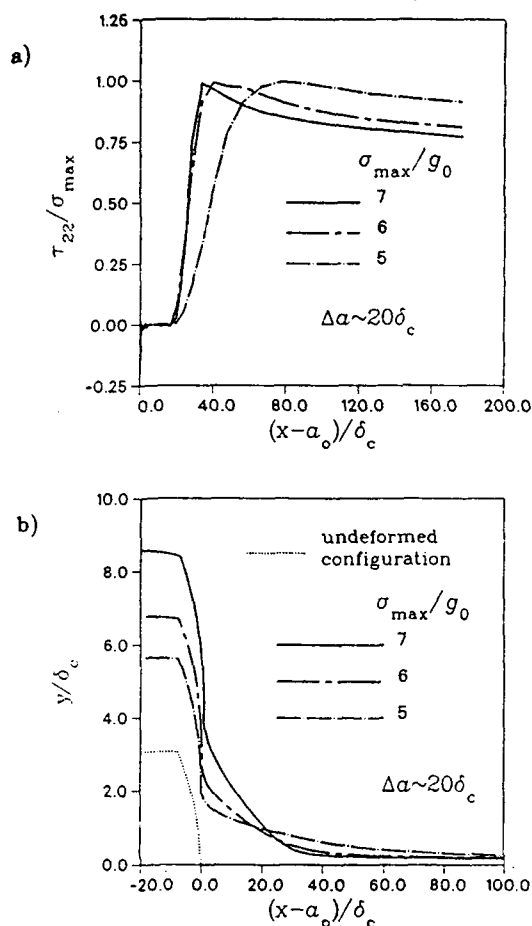


Fig. 8. (a) Distributions of τ_{22} Kirchhoff stresses, along the interface, normalized by the strength of the interface; (b) interface profiles. For each case considered the amount of crack growth is approximately $20\delta_c$.

the plot demonstrates the substantial increase in the plastic zone with increase in interfacial strength. We have observed that the accumulated slip (ahead of the notch tip) during the process of notch blunting and the initial stages of crack growth is in excess of 0.1. After an amount of growth of about $5\delta_c$ the accumulated slip at a comparable distance ahead of the tip decreases to less than a quarter of the value at initiation of growth and thereafter remains nearly constant with additional crack growth. The magnitude of the plastic strains is strongly affected by σ_{max} ; for example, γ_a at the initiation of growth is about 0.4 for $\sigma_{max} = 7g_0$ while it is less than 0.2 for $\sigma_{max} = 5g_0$. Hydrostatic stress contours of $\tau_h = 4.0g_0$ for two interfacial strengths $\sigma_{max} = 6g_0$ and $7g_0$ are shown in Fig. 9(b) for the same amount of crack growth as in the previous plots.

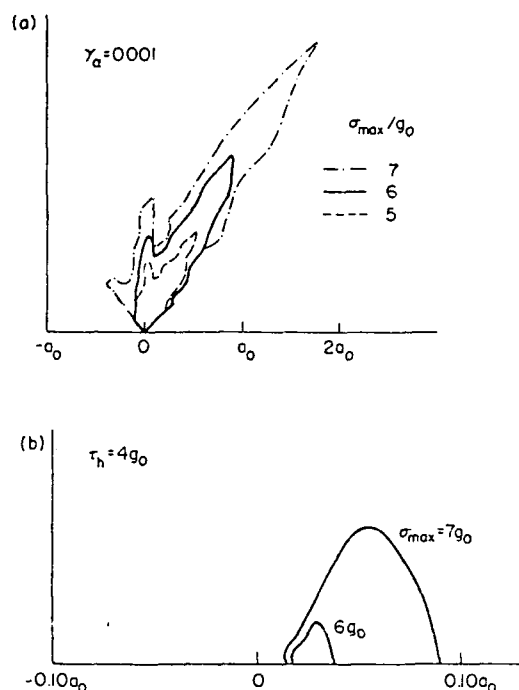


Fig. 9. (a) Accumulated slip contours of $\gamma_a = 0.001$ for three values of interface strength; (b) hydrostatic stress contours of $\tau_h = 4g_0$ for two values of interface strength. The amount of crack growth is approximately $20\delta_c$ in each case.

Hydrostatic stresses as large as $4g_0$ are not achieved in the case $\sigma_{max} = 5g_0$. It is apparent from Figs. 9(a) and 9(b) that the interface strength has a major effect on the size of both the plastic zone and the zone of high hydrostatic stress and therefore it is expected to play a prominent role in process of crack growth.

The results that have been presented thus far are based on the polynomial adhesive relation, described in Section 2.2.2. Calculations were also performed using the exponential adhesive relations (31) and (32). In these calculations, the interface strength and the work of de-adhesion were prescribed to have the same values as in the cases analyzed using the polynomial relation. Two values of interface strength $\sigma_{max} = 5g_0$ and $6g_0$ were selected. The initial slope of the exponential adhesive relation is higher than that of the polynomial relation so that the adhesive stress of the former reaches σ_{max} at a smaller interface displacement. Since the loss of adhesion begins at smaller interface displacement, the interface appears to be more brittle when this exponential relation governs the de-adhesion process. This behavior has been verified by our calculations and will be elaborated upon next.

The J integral was evaluated on paths near the growing crack tip and remote from it. Near the crack tip the value of J was path dependent. On contours remote from the tip (paths whose characteristic radius exceeds a_0) the value of J is essentially independent of path. The value of J in the remote region can be viewed as the macroscopic or global load parameter. With this viewpoint, we employ J as a load parameter for correlating the process of crack growth. For this purpose the average of the J values in the remote region is referred to as the J value.

The J resistance curves corresponding to all three interface strength levels and the two adhesive relations are shown in Fig. 10. The trend is clear. In all cases the onset of crack growth occurs at J values slightly in excess of φ_0 and the resistance curves rise rapidly for small amounts of growth. The curves for $\sigma_{\max} = 5g_0$ level off after growth of about $20\delta_c$. In contrast the resistance curve for $\sigma_{\max} = 7g_0$ continues to rise rapidly. The behaviors of the curves for $\sigma_{\max} = 6g_0$ fall between the two extremes. For interface strengths less than about $5g_0$ the resistance curve is controlled by φ_0 . These curves demonstrate the strong role of interface strength which is consistent with its role in establishing the stress distribution shown in Fig. 8(a) and the plastic zone size shown in Fig. 9(a). It can also be seen that the interface governed by the exponential relation exhibits a faster rate of growth. This behavior is consistent with the loss of adhesion being achieved at a smaller interface displacement for the exponential relation as has been noted previously. Nevertheless we point out that it is σ_{\max} that plays a

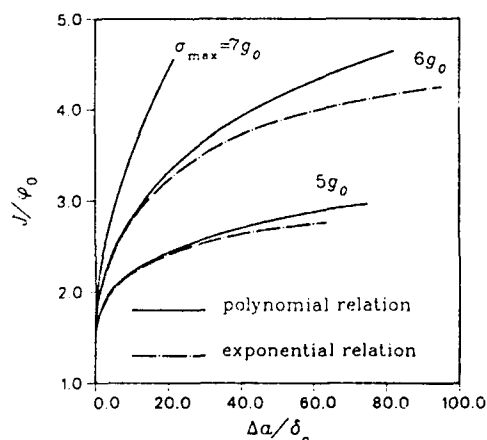


Fig. 10. J normalized by φ_0 vs. crack extension for three interface strengths based on exponential and polynomial adhesive relations.

more important role in determining the crack growth resistance.

4.2. Intermediate-size flaws

Intermediate-size flaws are defined by the ratios $a_0/h_0 \approx 50$ and $a_0/\delta_c \approx 150$. In this section we present the results using elliptical notch tips for $\sigma_{\max} = 7g_0$ although we have also performed a series of calculations for a range of σ_{\max} and circular notch tip geometry. Interface profiles are shown in Fig. 11(a) at various levels of nominal strain ϵ_{nom} , defined as the applied displacement on the top boundary divided by the initial height of the crystal. This measure of the stretch of the system includes contributions from the bulk material as well as the adhesive layer. Loss of adhesion begins at the notch tip which advances along the interface with increasing remote nominal strain. Figure 11(b) shows the distribution of the normal stress along the interface at the same

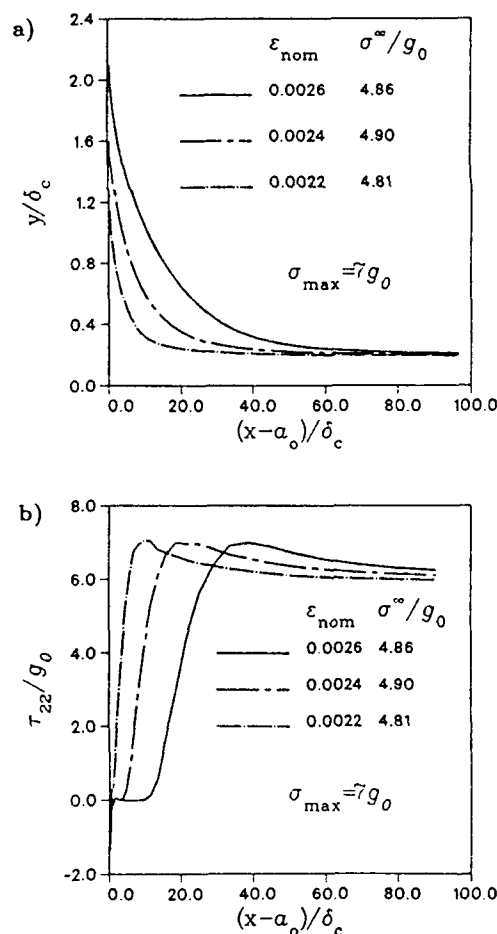


Fig. 11. (a) Interface profiles and (b) τ_{22} Kirchhoff stress distributions along the interface for intermediate-size flaws ($a_0/\delta_c \approx 150$; $\sigma_{\max} = 7g_0$).

Fig.
value

level
max
tip
from

c)

y/δc

Fig 1

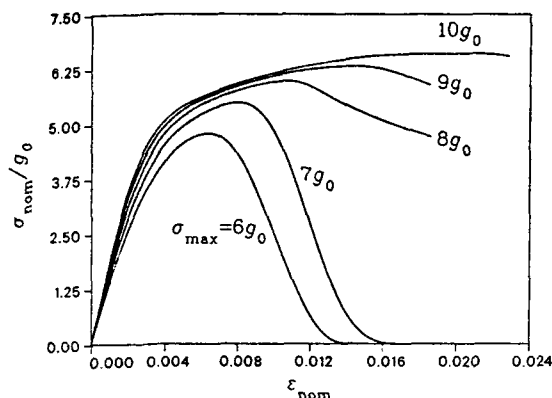


Fig. 12. Nominal stress vs. nominal strain curves for five values of σ_{max} for short flaws ($a_0/\delta_c \approx 15$).

levels of nominal strain. The stresses reach a maximum at a short distance ahead of the current tip and then gradually decrease as the distance from the flaw tip increases. It should be noted

that the stress gradients are much smaller than those of the long flaw ($a_0/\delta_c \approx 1500$).

4.3. Short flaws

Defects whose ratios a_0/h_0 are about 5 and a_0/δ_c less than about 50 are considered as short flaws. For these, the role of interface strength σ_{max} in the material's ductility and failure mode is discussed first. Values of σ_{max} in the range $6g_0$ – $10g_0$ were considered. We begin with the case where $a_0/h_0 = 5$ and $a_0/\delta_c \approx 15$. Figure 12 shows the variation in the nominal stress with nominal strain for different strengths of the interface. In all cases the nominal stress increases monotonically to a maximum and then decreases when a sizable fraction of the interface has failed.

The plot shown in Fig. 12 reveals an interesting phenomenon. There is a substantial loss of ductility when the interface strength decreases from $8g_0$ to $7g_0$. This dramatic change in the

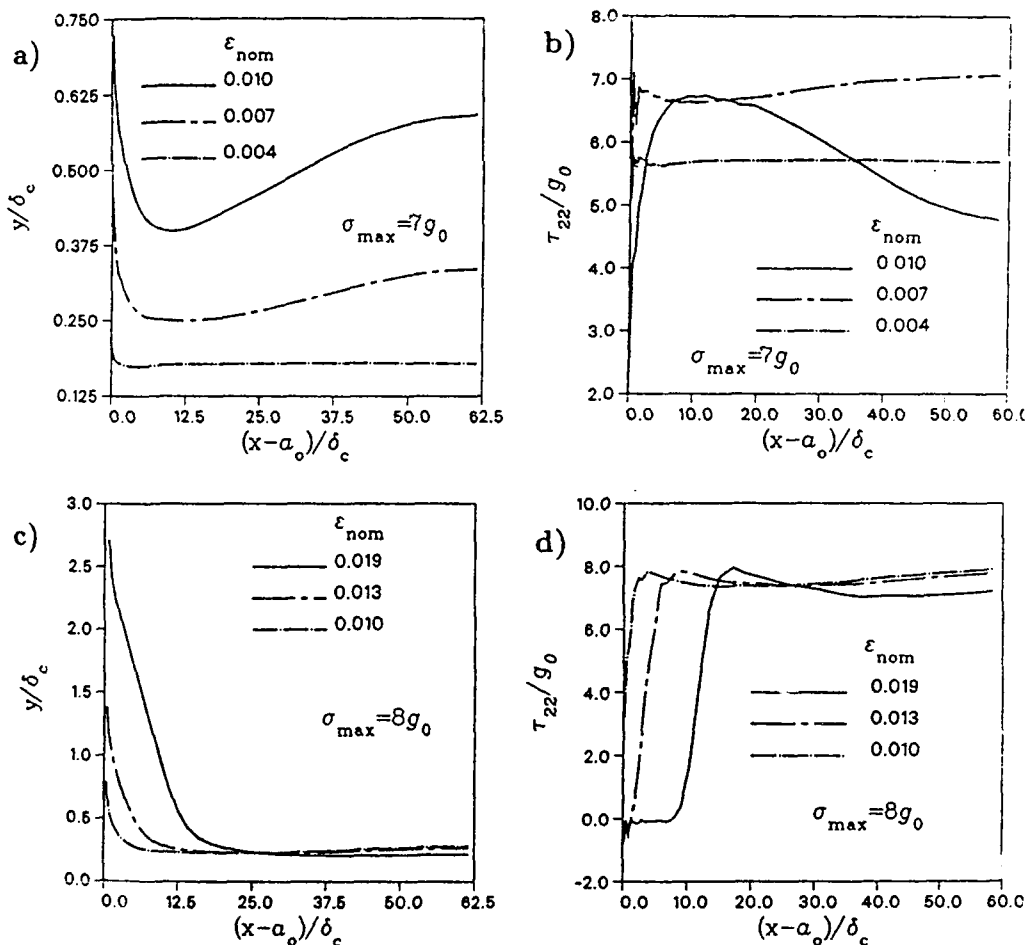


Fig. 13. Interface profiles and τ_{22} Kirchhoff stress distributions for short flaw: (a), (b) $\sigma_{max} = 7g_0$; (c), (d) $\sigma_{max} = 8g_0$.

ductility is due to a change in the failure mode. For interface strengths less than $8g_0$ the initial loss of adhesion occurs at the flaw tip which advances slowly with increasing remote strain. As the remote strain increases, a zone of high hydrostatic stress develops at the midligament (the zone midway between two neighboring flaws) which leads to a second site of debonding. In this region the normal stress is nearly uniform and very nearly equal to σ_{\max} and the plastic strain is negligibly small. This stress-strain state is unstable and indeed relatively rapid loss of adhesion proceeds from this site and advances towards the notch tip. This process is explained through the results shown in Figs. 13(a) and 13(b). Figure 13(a) shows the interface profile for $\sigma_{\max} = 7g_0$ at various levels of nominal strain. The interface displacement in the vicinity of the midligament is uniformly large and increases substantially with increasing nominal strain. Figure 13(b) shows the distribution of the normal stresses along the interface at the same levels of the nominal strain. The stresses along the greater part of the ligament are uniformly high before debonding and at the early stages of debonding. This stress pattern is in sharp contrast with the distribution for the long and intermediate flaw discussed in the preceding sections. The rapid advance of the debonded region towards the notch tip is evident from the loss of normal stress shown by the curve for $\epsilon_{\text{nom}} = 0.01$. It is note worthy that, in the case of the weaker interface, $\sigma_{\max} \leq 7g_0$, the total nominal strain at complete debonding of the crystal from the rigid substrate is not significantly affected by interface strength. The total ϵ_{nom} is about equal to δ_c/L_0 . This is not surprising since the crystal develops small plastic strains throughout the process of debonding. This latter aspect is discussed in some detail in connection with the perfect interface problem in Appendix A.

For interfacial strengths greater than $7g_0$ there is only one site of debonding. This occurs only at the tip of the flaw and advances towards the midligament in a gradual manner. This process is responsible for the gradual decrease of the nominal stress for $\sigma_{\max} = 8g_0$, $9g_0$ and $10g_0$ as shown in Fig. 12. The process of debonding for $\sigma_{\max} = 8g_0$ is shown in detail in Fig. 13(c) where the interface profiles at three levels of nominal strain are plotted. The distribution of the normal stresses along the interface, for the same levels of nominal strain, are shown in Fig. 13(d). The normal stresses exhibit a weak maximum near the

current flaw tip which is in contrast with the stress pattern in Fig. 13(b). It may be noted that the plastic strain of the crystal is much larger for interfacial strengths in excess of $7g_0$ and this results in higher ductility.

We have investigated the effects caused by varying σ_{\max} with δ_c fixed. Changing σ_{\max} under constant δ_c results in a change of the de-adhesion energy φ_0 . The effects of varying σ_{\max} and δ_c but

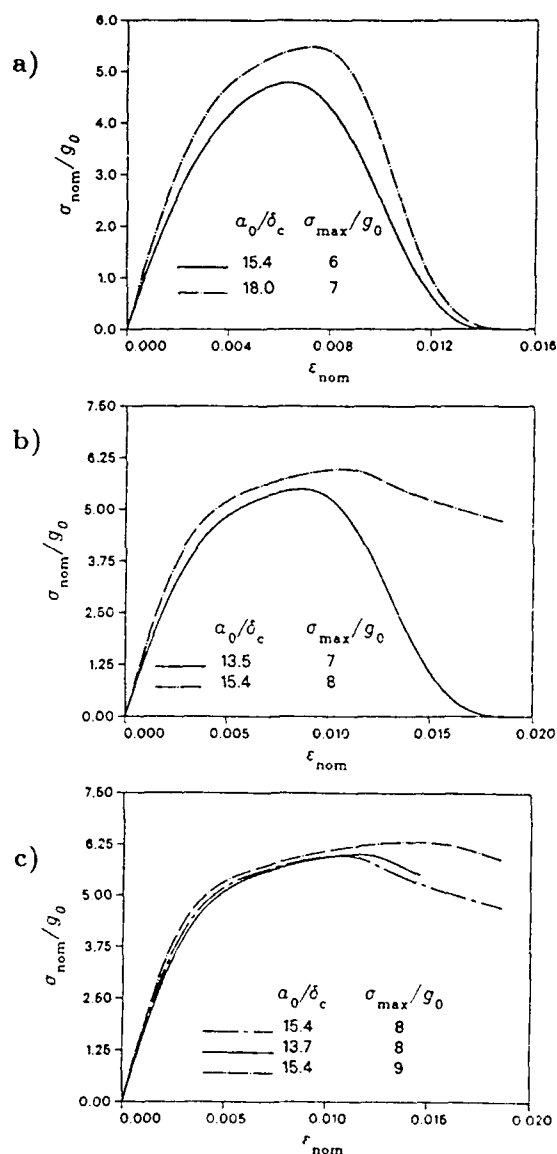


Fig. 14. Nominal stress vs. nominal strain for short flaws: (a) $\varphi_0 = 0.22a_0g_0$; (b) $\varphi_0 = 0.29a_0g_0$; (c) the interfaces with parameters $a_0/\delta_c \approx 13.7$, $\sigma_{\max} = 8g_0$ and $a_0/\delta_c \approx 15.4$, $\sigma_{\max} = 9g_0$ have the same energy of de-adhesion ($\varphi_0 = 0.33a_0g_0$). These interfaces have strengths that differ 11.8% with respect to their average value. The interfaces with the same strength have energies of de-adhesion that differ 11.8% with respect to their average value.

holding φ_0 constant are discussed next. Figure 14(a) show the effects of varying σ_{\max} and δ_c so as to keep φ_0 at the fixed value of $0.22a_0g_0$. The values $\sigma_{\max} = 6g_0$ and $7g_0$ were chosen so that the same failure mode (debonding at the notch tip and at the midligament) develops in both cases. For these cases, the ductility as measured by the work or by the nominal strain to total separation are nearly equal. In Fig. 14(b) we compare two cases where $\sigma_{\max} = 7g_0$ and $8g_0$. The lower interface strength produces debonding at two sites while the higher strength causes debonding at the notch tip only. The values of δ_c are such as to maintain $\varphi_0 = 0.29a_0g_0$. Very different ductilities between the two cases are seen although the work φ_0 for interfacial separation is the same. Three cases, which produce de-adhesion only at the notch tip, are shown in Fig. 14(c). Two cases correspond to $\sigma_{\max} = 8g_0$, $a_0/\delta_c \approx 13.7$ and $\sigma_{\max} = 9g_0$, $a_0/\delta_c \approx 15.4$; these have the same energy of de-adhesion, i.e. $\varphi_0 = 0.33a_0g_0$. The interface strengths differ by 11.8%. The third case with $\sigma_{\max} = 8g_0$, $a_0/\delta_c \approx 15.4$ has a smaller value of φ_0 which is 11.8% smaller than that of the two preceding cases. It can be seen that ductility is more greatly affected by changing σ_{\max} (keeping φ_0 constant) than by changing φ_0 (keeping σ_{\max} constant).

We may conclude from this series of calculations that the ductility is strongly affected by the interface strength when de-adhesion is accompanied by large-scale plastic deformation. In the context of the present model, large-scale plasticity can be said to occur when the nominal plastic strain of the matrix (or crystal) is comparable with δ_c/L_0 . In contrast, if little plastic deformation develops during the process of de-adhesion, then the energy of interfacial separation appears to dominate the overall response of the material.

The third series of calculations was aimed at sorting size effects (geometrically similar notches), relative to the fracture process zone, on ductility and failure mode. With the aspect ratio a_0/h_0 of the flaw fixed at 5, we carried out calculations for $\sigma_{\max} = 7g_0$ and a_0/δ_c approximately equal to 15, 23 and 46. Plots of nominal stress vs. nominal strain for the three a_0/δ_c ratios are shown in Fig. 15. It is apparent that the ductility decreases as the fracture process zone size decreases (relative to the defect size), since the fracture process zone size is scaled by the work of de-adhesion (for fixed σ_{\max}). For the two ratios

$a_0/\delta_c \approx 15$ and 23, debonding initiates at the notch tip and the midligament, as indicated by the results in Fig. 16(a) for $a_0/\delta_c \approx 23$. For this failure mode the amount of plastic flow that develops with interfacial de-adhesion is small and this

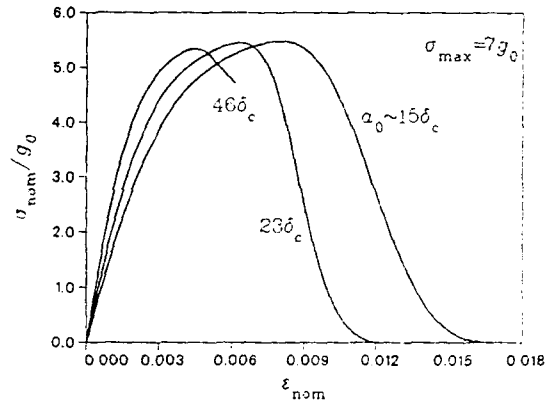


Fig. 15. Nominal stress vs. nominal strain for short flaws. The interfaces have the same strength and different a_0/δ_c and h_0/δ_c ratios ($\sigma_{\max} = 7g_0$; $a_0/h_0 = 5$).

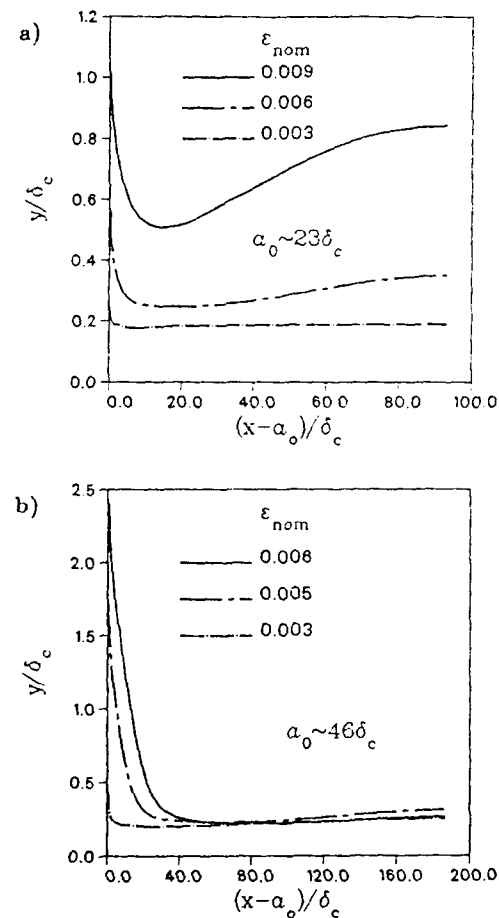


Fig. 16. Interface profiles for short flaws ($\sigma_{\max} = 7g_0$; $a_0/h_0 = 5$): (a) $a_0/\delta_c \approx 23$; (b) $a_0/\delta_c \approx 46$.

thereby leads to the rapid drop in the nominal stress. In contrast, debonding initiates at the notch tip of the larger flaw ($a_0/\delta_c \approx 46$) and the failure process proceeds from this site as indicated by the results in Fig. 16(b). Thus, while the maximum load is reached at a smaller nominal strain, the drop in the nominal stress may be more gradual than those for the two smaller flaws since larger amounts of plastic flow are expected to develop as the debonding process of the larger flaw continues.

It is clear, based on the nominal stress-strain curves presented in this section, that the initial

stiffness of the system increases with increase in the interface strength and in the ratio a_0/δ_c . A quantification of the above effect is presented in Appendix A, where an expression for the initial stiffness of a crystal perfectly bonded on a rigid substrate is given.

5. Results using J_2 flow theory

5.1. Long flaws

As in the crystal plasticity calculations the geometry of the long flaw is described by the ratios $a_0/h_0 = 500$ and $a_0/\delta_c \approx 1500$. We present

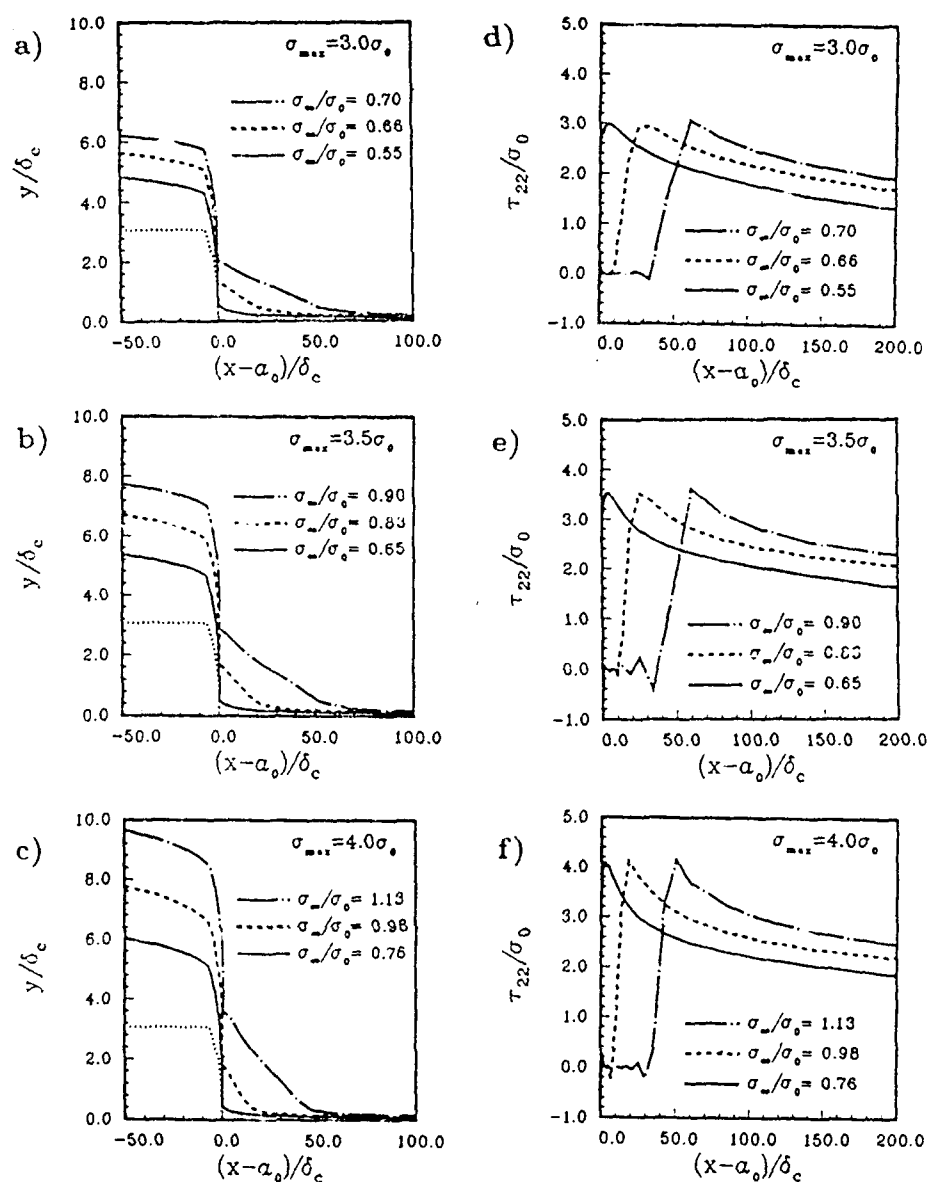


Fig. 17. (a)-(c) Crack-opening profiles and (d)-(f) τ_{22} Kirchhoff stress distributions along the interface, for three interface strengths. In each case, $a_0/h_0 \approx 1500$.

results for three different interface strengths $\sigma_{\max} = 3.0\sigma_0$, $3.5\sigma_0$ and $4.0\sigma_0$. These values roughly correspond to $\sigma_{\max} = 6.0g_0$, $7.0g_0$ and $8.0g_0$ in terms of the hardness parameter used in crystal plasticity.

The deformation produces an essentially tensile opening mode at the crack tip. Figures 17(a), 17(b) and 17(c) show the crack profiles at various stages of remote loading for the cases where $\sigma_{\max} = 3.0\sigma_0$, $3.5\sigma_0$ and $4.0\sigma_0$. Such profiles are similar for all three cases of interface strength and indicate that the cracks continue to open, and to debond, in a primarily tensile mode. As was

noted previously, a normal displacement $\delta_n = \delta_c$ corresponds to a complete loss of adhesion and this is our criterion for defining the current crack tip position. De-adhesion starts at a lower remote stress for the lower interface strength $\sigma_{\max} = 3\sigma_0$ and proceeds at a considerably faster rate. The crack-opening process was found to be smooth in all three cases examined and continued to occur only at the crack tip as the remote displacement increases. It may be noted that the amount of crack tip blunting increases with increasing interface strength. Figures 17(d), 17(e) and 17(f) show the normal traction along the bond line for the

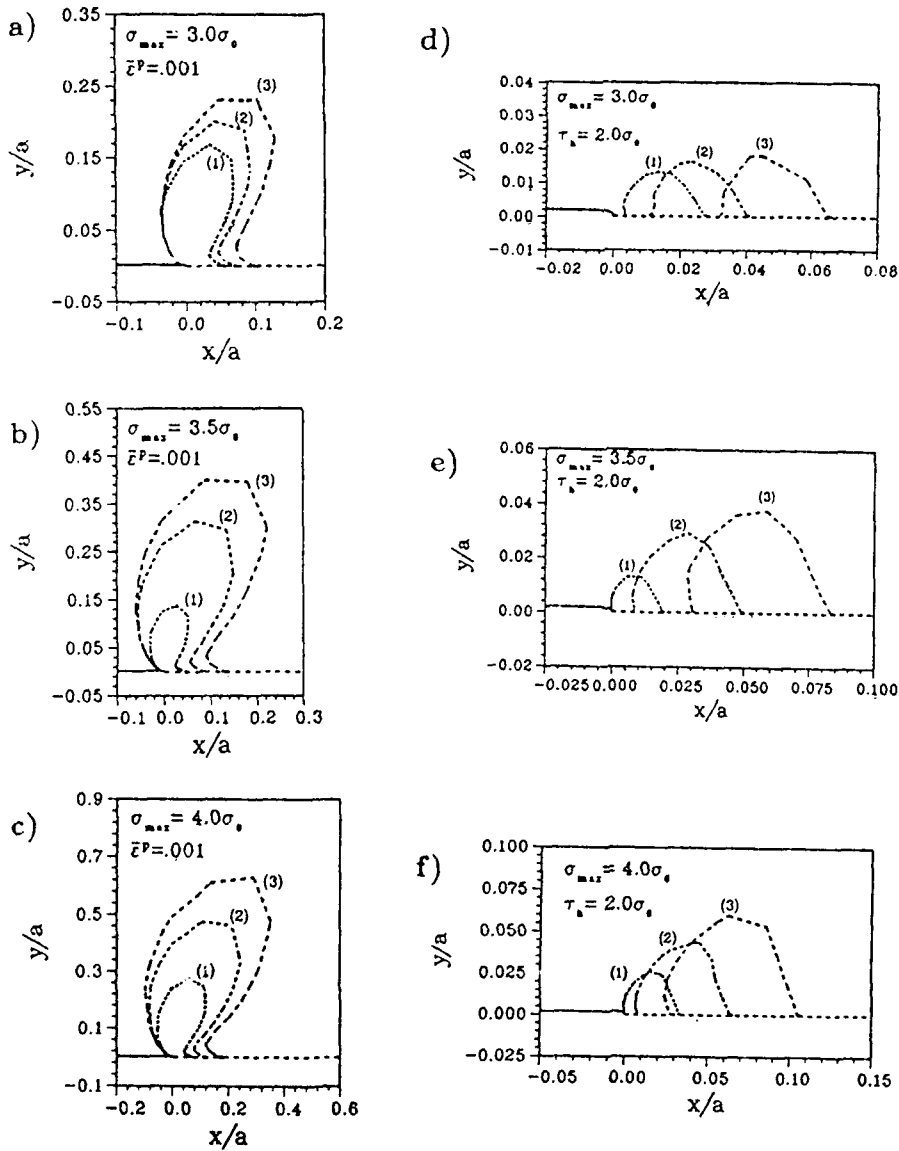


Fig. 18. (a)–(c) Contours of effective plastic strain $\bar{\epsilon}^p = 0.001$; (d)–(f) hydrostatic stress contours of $\tau_n = 2.0\sigma_0$ for different values of interface strength. The amount of crack growth is approximately the same for all three values of σ_{\max} : curve (1) $\Delta a = 0$; curve (2) $\Delta a \approx 10\delta_c$; curve (3) $\Delta a \approx 45\delta_c$.

remote stress levels corresponding to those in Figs. 17(a), 17(b) and 17(c). It is seen that the stress fields essentially translate with the moving crack tip and that the peak stress is maintained at σ_{\max} (as it must for crack growth to continue). For these interface strengths the stress gradients increase slightly as σ_{\max} increases.

Figure 18 shows effective plastic strain contours at $\bar{\epsilon}^p = 0.001$ for three different levels of remote stress. This contour is effectively the elastic-plastic boundary. The amount of crack growth is roughly the same for each interface strength considered. In all cases, yielding is confined to a fraction of the ligament although the deformation is clearly outside the range of small-scale yielding. It can be seen that for the same amount of crack growth the plastic zone for the strongest interface is nearly three times larger than that for the weakest interface. The development of a mode-I-like crack tip field is evident and the leading edge of the plastic zone essentially translates with the moving crack tip.

Figure 18 also shows contours of hydrostatic stress for the same amount of crack growth for the three interface strengths. The zone enclosed by the hydrostatic tension contour given by $\tau_h = 2\sigma_0$ translates with the crack tip. For the weak strength interfaces the contour size increases slightly. In contrast, the contour size increases substantially for the stronger interface strengths. The translation and expansion of the contour are a result of the stress redistributing from a high gradient stationary crack tip field to a field of weaker stress gradient.

The shape of the plastic zones for a growing crack suggests that, at least for these modest levels of crack growth, a mode-I-like crack tip field is maintained which scales approximately with the level of the J integral. To explore this, the value of J was computed at each numerically obtained crack growth solution using a finite deformation implementation of the domain integral method [24]. For each solution, J values were extracted from annular domains whose mean radii range from δ_c to $10^3\delta_c$. J values from domains comparable in size with δ_c and the crack tip opening showed strong path dependence as they must. Beyond these near-tip domains, J is essentially path independent, the variation in values being less than 1%. In subsequent discussions the J value referred to is the average of these nearly path-independent values, and this can serve as a load parameter.

Figure 19 shows the radial variation in Kirchhoff stress τ_{22}/σ_0 along the bond line for the levels of remote loading indicated. Also shown on these plots for $\sigma_{\max} = 3.0\sigma_0$, $3.5\sigma_0$ and $4.0\sigma_0$ are the Hutchinson-Rice-Rosengren (HRR) fields of mixity 0.97, 0.98 and 1.0 respectively. A mixity of 1.0 corresponds to pure mode I and departure from unity indicates deviation from pure mode I conditions. Thus the above mixities indicate that the near-tip fields become more mode I like as the interface strength increases. This

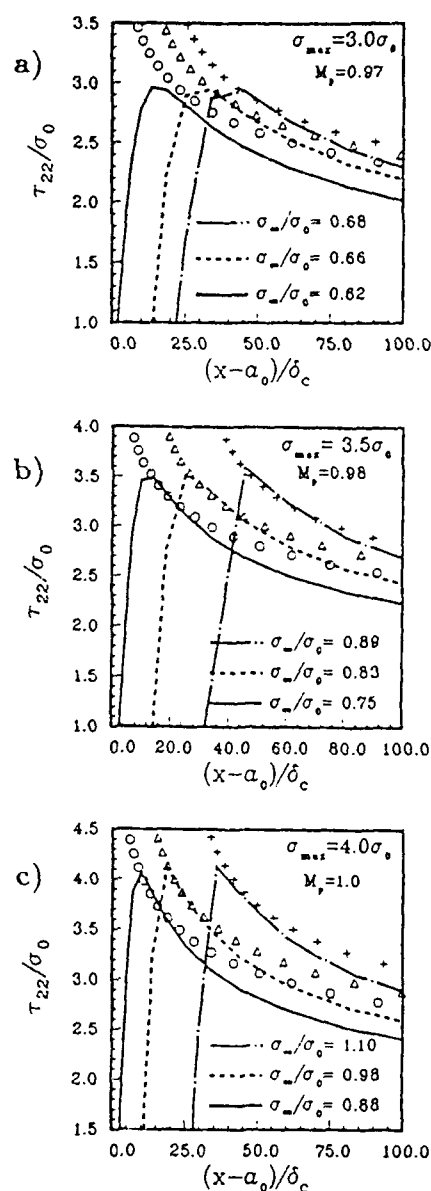


Fig. 19. Comparison of near-tip fields with mixed-mode HRR fields for three interface strengths. (a) $\sigma_{\max} = 3\sigma_0$, $M_I = 0.97$; (b) $\sigma_{\max} = 3.5\sigma_0$, $M_I = 0.98$; (c) $\sigma_{\max} = 4\sigma_0$, $M_I = 1.0$.

behavior is expected since the amount of plastic yielding increases substantially with interface strength and this promotes mode-I-like conditions. The values for the mixities are suggested by the small-scale yielding analysis discussed by Shih and Asaro [5, 6] and Shih *et al.* [24]. In plotting the HRR fields for a particular extension we have

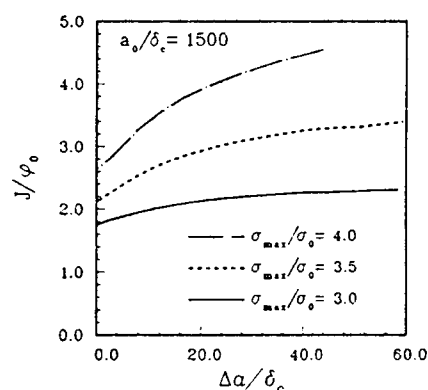


Fig. 20. J resistance curves for a long flaw for three interface strengths.

used the J value calculated from the numerical fields for that particular crack extension and we have repositioned the HRR stresses along the axis of the interface line by a distance corresponding to that amount of crack extension. We can see the good agreement between the growing-crack full field solution and the HRR stresses over distances large compared with the fracture process zone size as scaled by δ_c . This agreement suggests that the remote J value which is essentially path independent is an appropriate load characterization parameter for the near-tip fields, at least for modest amounts of crack extension and for the interface strengths considered.

The crack grows stably under rising remote displacement for the levels of interface strength considered in this section. To examine the effect of σ_{rx} (the adhesive strength) and crack tip plasticity on fracture toughness, we have plotted the computed J values vs. crack growth in Fig. 20 for the three levels of σ_{max} considered. Since J is normalized by the respective ϕ_0 , differences in

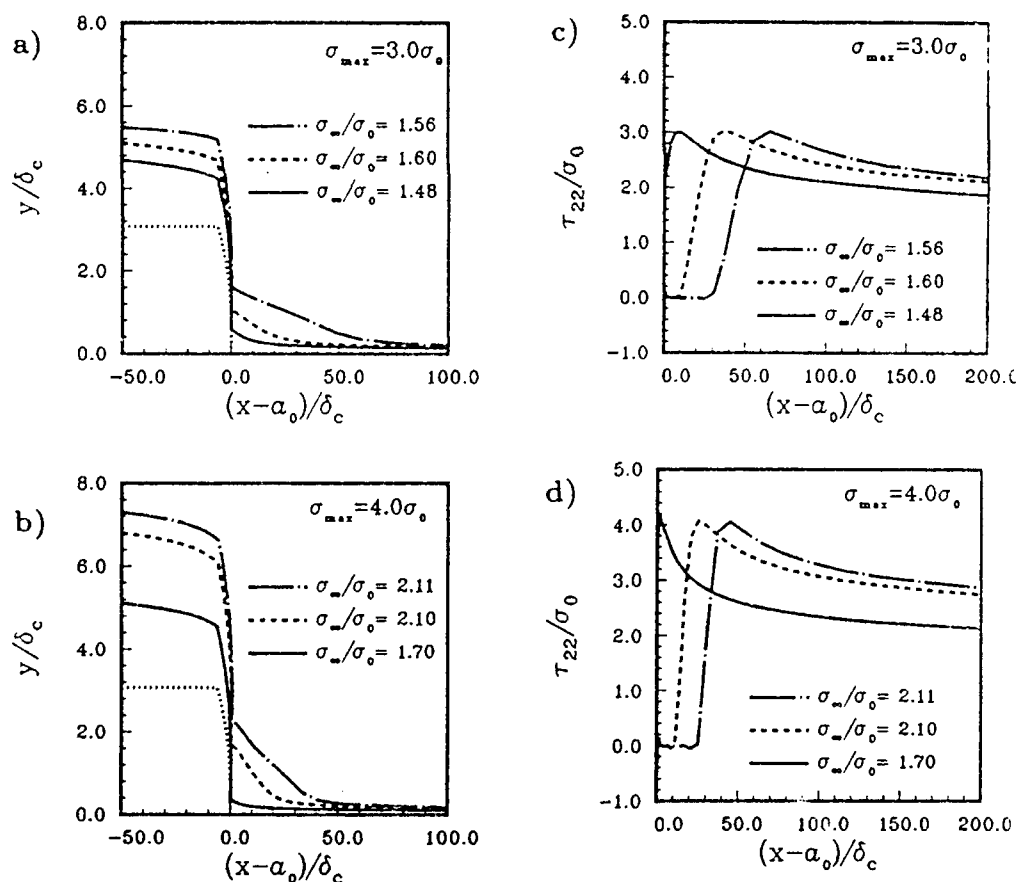


Fig. 21. (a), (b) Flaw-opening profiles and (c), (d) normal Kirchhoff stress distributions along the interface, for two interface strengths. In each case, $a_0/\delta_c \approx 150$.

the resistance curves are primarily due to plasticity. For example for $\sigma_{\max} = 3.0\sigma_0$ the value J_i of J at the onset of growth, is close to φ_0 . The computed J values rise moderately to a steady state value of about $2.0\varphi_0$ as the crack grows. This behavior is indeed suggested by the plastic zone size shown in Fig. 18(a). For the $\sigma_{\max} = 3.5\sigma_0$ case, J_i is about twice φ_0 ; however, the J required for further crack growth rises more rapidly. For the strongest case considered ($\sigma_{\max} = 4.0\sigma_0$), $J_i \approx 2.5\varphi_0$, which is larger than those for the other two cases. Moreover the J required for further crack growth rises more rapidly than that for the $\sigma_{\max} = 3.5\sigma_0$ case. The behavior of the resistance curve for the strongest interface is also suggested by the large increase in plastic zone size shown in Fig. 18(c). The behavior of J_i and the J_R curve are thus strongly affected by crack tip plasticity, which depends on σ_{\max} .

The calculations which led to the above results used the elliptical notch tip mesh shown in Fig. 5(a). Similar calculations were carried out using

the circular notch tip mesh shown in Fig. 5(b). The differences in the stress and deformation fields and J resistance curves between the two series of calculations were not significant, suggesting that notch acuity is not an important geometric factor for long flaws.

5.2. Intermediate-size flaws

Calculations were carried out for an intermediate-size defect, where $a_0/h_0 = 50$ and $a_0/\delta_c \approx 150$ with interface strengths of $\sigma_{\max} = 3\sigma_0$ and $4\sigma_0$. Figure 21 shows the flaw tip opening profiles, along with the normal stresses developed ahead of the flaw tip, at three remote levels of tensile stress. It is clear from these figures that the flaws open smoothly and quickly develop sharp profiles much like those characteristic of long flaws as discussed in the previous section. The stress fields take on forms that resemble those of the long flaws described above, with the stress concentration refocusing ahead of the current flaw tip. However, it may be noted that the stress

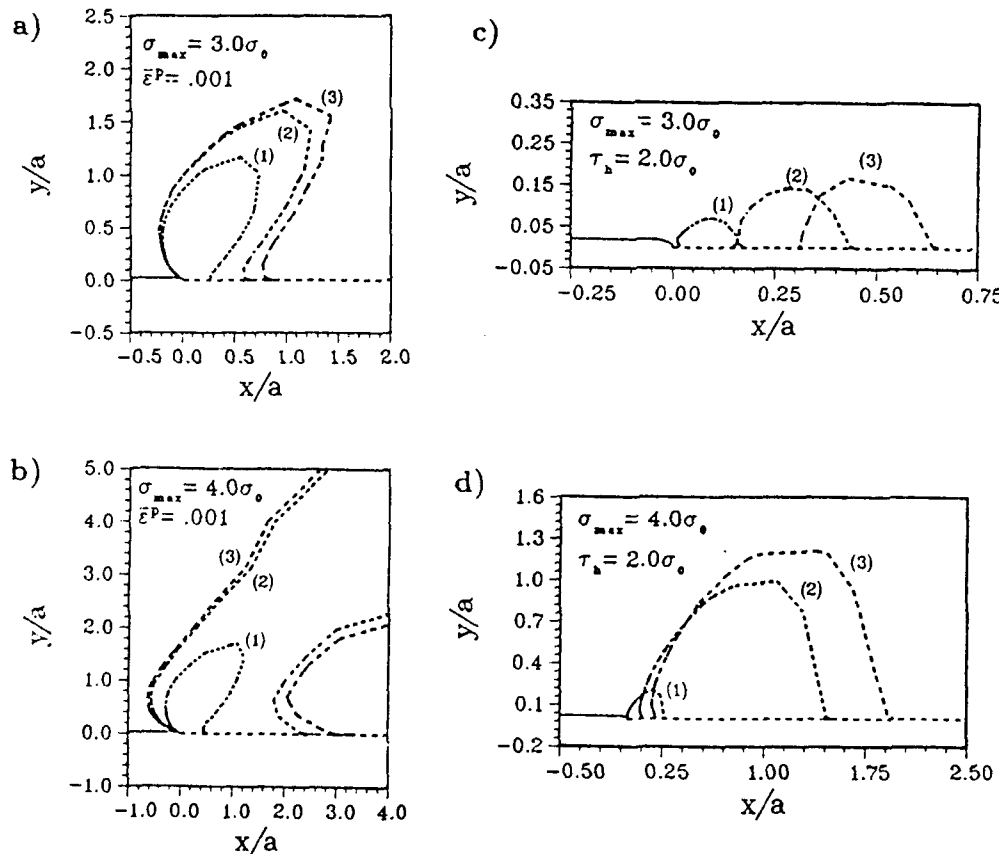


Fig. 22. (a), (b) Contours of effective plastic strain, $\epsilon^P = 0.001$, for different values of interface strength and (c), (d) hydrostatic stress contours of $\tau_h = 2\sigma_0$ for different values of interface strength at the same amount of flaw growth: curve (1) $\Delta a = 0$; curve (2) $\Delta a \approx 15\delta_c$; curve (3) $\Delta a \approx 30\delta_c$.

Fig. 23.
fields
 $\sigma_{\max} = 4$

gradients are weaker than those for the long flaw ($a_0/\delta_c \approx 1500$). Figure 22 shows contours of effective plastic strain and hydrostatic stress at three stages of flaw growth. We see that for the $\sigma_{\max} = 3\sigma_0$ case we have contained yielding although for the $\sigma_{\max} = 4\sigma_0$ case the ligament has fully yielded before any significant flaw growth takes place. Again we see that the hydrostatic stress contours translate with the flaw tip and increase in size as the flaw advances.

The J integral was again found to be path independent to within 1% for remote paths and again we address the question of J dominance by comparison with HRR fields. The comparison is shown in Fig. 23. We have used mode I HRR fields for the comparisons since the size of the plastic zone is comparable with or larger than flaw length. For the $\sigma_{\max} = 3\sigma_0$ case the flaw grows under contained yielding and the agreement between the numerical fields and the HRR fields seems to improve after moderate amounts

of flaw growth. This result is in contrast with the case for the stronger interface. Initially the agreement between HRR fields and numerical fields is good and the agreement deteriorates as the flaw advances. We observe that the large discrepancy between the flaw tip fields for the stronger interface and the HRR fields develops as the ligament becomes fully yielded.

The J resistance curves for both interface strengths are shown in Fig. 24. These are similar in form to the case of a long flaw. A relatively flat resistance curve for the weak interface, with J_i close to φ_0 because of the small amount of plasticity and a rising resistance curve with $J_i \approx 2.5\varphi_0$ for $\sigma_{\max} = 4\sigma_0$.

Similar calculations for an intermediate-size flaw were carried out using the circular notch tip mesh in Fig. 5(b). For the weak interface, no significant differences between the stress and deformation fields were seen. However, for the stronger interface ($\sigma_{\max} = 4\sigma_0$) debonding initiates slightly ahead of the notch tip and propagates towards the midligament. This suggests that notch acuity may be an important geometric factor for intermediate-size flaws. Notch acuity also has a strong effect on the behavior of short flaws and this has been studied by Varias *et al.* [25].

5.3. Short flaws

Figure 25 shows the opening profiles and normal stresses along the bond line for a short flaw, where $a_0/h_0 = 5$, $a_0/\delta_c \approx 15$ and $\sigma_{\max} = 3\sigma_0$ and $4\sigma_0$. It can be seen that the stress fields do not resemble the fields ahead of a sharp crack. There is very little stress concentration at the tip of the flaw and the normal stress is nearly uniform along the ligament and its magnitude is

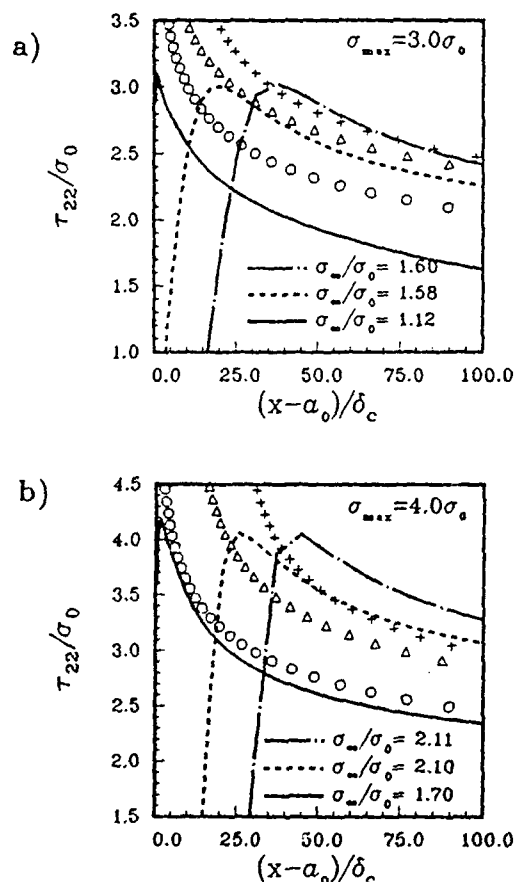


Fig. 23. Comparison of near tip fields with mode I HRR fields for two interface strengths: (a) $\sigma_{\max} = 3\sigma_0$; (b) $\sigma_{\max} = 4\sigma_0$.

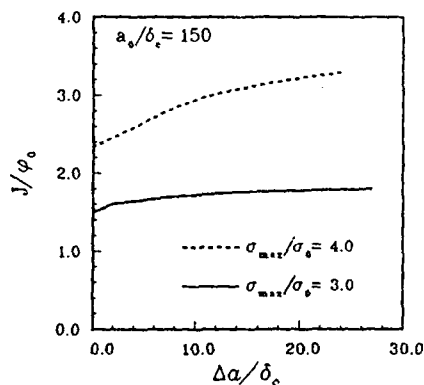


Fig. 24. J resistance curves for an intermediate-size flaw for two interface strengths.

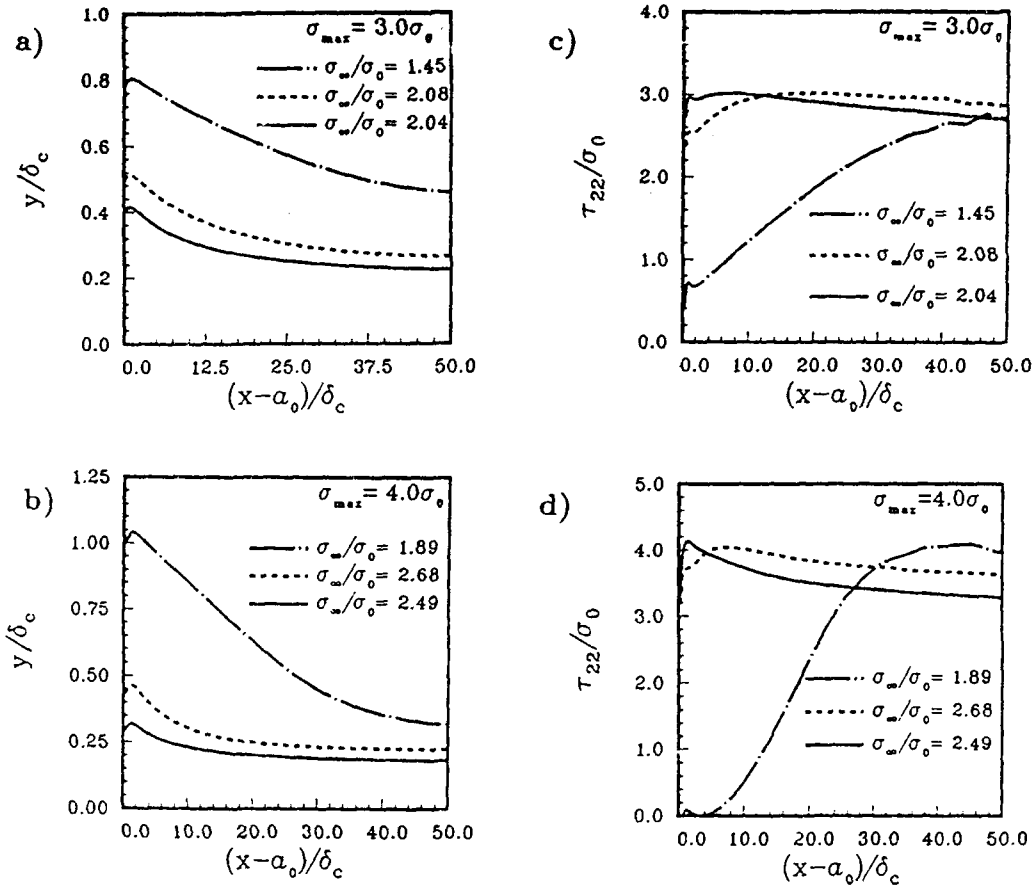


Fig. 25. (a, b) Interface profiles and (c), (d) normal Kirchhoff stress distributions along the interface, for two interface strengths. In each case, $a_0/\delta_c \approx 15$.

close to σ_{\max} . Furthermore the J integral is strongly path dependent. This behavior is true for both interface strengths considered. It can be seen from the interface profiles that, while debonding initiates at the flaw tip, further de-adhesion is not confined to the tip. When maximum load is reached, the entire interface has undergone significant de-adhesion and the remote load then drops abruptly. We conclude that the short flaw does not behave like a crack.

6. Discussion and conclusions

The adhesive relation of the exponential and polynomial type is completely specified by the de-adhesion energy φ_0 and the interface strength σ_{\max} . The adhesive relation has a characteristic length δ_c which is determined by φ_0 and σ_{\max} . For example, δ_c is given by $16\varphi_0/9\sigma_{\max}$ for the polynomial relation. Thus, δ_c and σ_{\max} also specify the adhesive relation. To varying degrees, all three

parameters affect the ductility and the failure modes of the system. For example, in the case of the homogeneous block debonding from a rigid substrate, as discussed in Appendix A, the level of matrix plastic strains that are achieved during debonding compared with δ_c/L_0 determines how the adhesive parameters control ductility. When the nominal strain ϵ_{nom} of the system at separation is comparable with δ_c/L_0 , ductility is controlled by φ_0 . For stronger interfaces, where ϵ_{nom} becomes large compared with δ_c/L_0 , σ_{\max} plays the dominant role. This example has direct relevance to the more complex cases involving the separation of interfaces containing periodic arrays of short flaws with a_0/h_0 approximately 5 as discussed in Section 4.3. In these cases, both the process of failure (i.e. the failure mode) and the resulting toughness as measured by the total work expended on the flawed body can be affected. We have shown that, when σ_{\max} is large relative to the material's yield strength or when

the flaw size is large compared with δ_c , the process of de-adhesion initiates and proceeds from a single site which is the tip of the flaw. On the contrary, when the relative flaw size a_0/δ_c is smaller than 40, and σ_{max} is small, de-adhesion can occur at two sites: at the flaw tip and at the midligament. For even blunter short flaws, de-adhesion may initiate only at the midligament [25].

In the case of long flaws the plastic strains well within the flaw tip plastic zone are large and the failure behavior is then controlled by the plastic zone size relative to δ_c . For example, the fracture toughness and the growth resistance are controlled primarily by φ_0 when the plastic zone size during the process of flaw growth is comparable with δ_c . However, when the interface is sufficiently strong that the plastic zone that develops at the onset of flaw growth is large compared with δ_c , it is the interface strength σ_{max} that controls the initiation toughness and flaw growth resistance curve. Such behavior under large-scale plasticity can be clearly seen in Fig. 10 for the case of crystal plasticity and in Fig. 20 where the material is modeled by J_2 flow theory.

We observe that the long flaw ($a_0/\delta_c \approx 1500$) behaves like a crack for the range of interface strengths and load levels considered for both material characterizations. For certain interface strengths and load levels, the fields of the intermediate-size flaw ($a_0/\delta_c \approx 150$) have some crack-like features. In the case of the short flaw ($a_0/\delta_c < 50$), crack-like behavior was not observed for any interface strength or load level. We reached these conclusions through direct comparisons of the full field solutions for stationary and growing flaw with singular fields of the HRR type. Specifically, the stationary interface long flaw fields in the annular zone, which encompass the finite strain zone and the fracture process zone, are well approximated by mixed-mode HRR fields. Furthermore, the annular zone of high stresses essentially translates with the moving long flaw tip and the fields remain in agreement with the HRR fields for limited amounts of growth. Such observations allow us to conclude that the near-tip state is characterized by J and the mode mixity. Recent results of Needleman [26] are consistent with our results described above. For example in his studies of de-adhesion along an imperfect interface he observes the transition from a more or less uniform separation profile to crack-like profiles as the ratio of defect length to

the characteristic dimension δ_c increases. For the longest defect considered, i.e. $a_0/\delta_c = 7500$, the shape of his plastic zone contour is consistent with the tension-dominated plastic zone contour given by Shih and Asaro [4].

We must point out that the boundary value problem dealt with in this paper gives rise to very high triaxial stress states over the entire ligament as the deformation progresses into the fully yielded state. Such stress states may not be typical of load states encountered in actual systems. Investigations for a plastically deformable material on an elastic substrate using boundary conditions which lead to less severe triaxiality are in progress.

Acknowledgments

This study is supported by the Office of Naval Research through a grant "Mechanics of Interface Cracks". The computations were performed at the San Diego Supercomputer Center and on the Alliant Computer system in the Brown University Computational Mechanics Facility; the latter facility was established with the support of the National Science Foundation and Defense Advanced Research Projects Agency.

References

- 1 A. G. Varias, N. P. O'Dowd, R. J. Asaro and C. F. Shih, *Proc. Acta Metall.-Scr. Metall. Conf. on Debonding, Structure, and Mechanical Properties of Metal-Ceramic Interfaces*, in the press.
- 2 P. E. McHugh, A. G. Varias, R. J. Asaro and C. F. Shih, *Future Generation Computer Systems*, 5 (1989) 295.
- 3 J. H. Rose, J. Ferrante and J. R. Smith, *Phys. Rev. Lett.*, 47 (1981) 675.
- 4 C. F. Shih and R. J. Asaro, *J. Appl. Mech.*, 55 (1988) 299.
- 5 C. F. Shih and R. J. Asaro, *J. Appl. Mech.*, in the press.
- 6 C. F. Shih and R. J. Asaro, *Mater. Sci. Eng.*, A107 (1989) 145.
- 7 R. J. Asaro, *J. Appl. Mech.*, 50 (1983) 921.
- 8 S. V. Harren, H. E. Deve and R. J. Asaro, *Acta Metall.*, 36 (1988) 2435.
- 9 B. Moran, M. Ortiz and C. F. Shih, *Int. J. Numer. Methods Eng.*, in the press.
- 10 A. W. Thompson, *Metall. Trans.*, 5 (1974) 39.
- 11 J. C. Simo and M. Ortiz, *Comput. Methods Appl. Mech. Eng.*, 49 (1985) 221.
- 12 J. Ferrante and J. R. Smith, *Phys. Rev. B*, 31 (1985) 3427.
- 13 J. R. Rice and J. S. Wang, *Mater. Sci. Eng.*, A107 (1989) 23.
- 14 D. S. Dugdale, *J. Mech. Phys. Solids*, 8 (1960) 100.
- 15 G. I. Barenblatt, *Adv. Appl. Mech.*, 7 (1962) 56.
- 16 B. A. Bilby, A. H. Cottrell and K. H. Swinden, *Proc. R. Soc. (London), Ser. A*, 285 (1963) 23.

- 17 A. S. Argon and J. Im, *Metall. Trans. A*, 6 (1975) 839.
- 18 A. S. Argon, J. Im and A. Needleman, *Metall. Trans. A*, 6 (1975) 815.
- 19 H. Cialone and R. J. Asaro, *Metall. Trans. A*, 12 (1981) 1373.
- 20 A. Needleman, *J. Appl. Mech.*, 54 (1987) 525.
- 21 D. Pierce, R. J. Asaro and A. Needleman, *Acta Metall.*, 31 (1983) 1951.
- 22 T. J. R. Hughes, *Int. J. Numer. Methods Eng.*, 15 (1980) 1413.
- 23 J. R. Rice, W. J. Drugan and T. L. Sham, *Proc. 12th Natl. Conf. on Fracture Mechanics*, in *ASTM Spec. Tech. Publ.* 700 (1980) p. 189.
- 24 C. F. Shih, R. J. Asaro and N. P. O'Dowd, *Proc. Acta Metall.-Scr. Metall. Conf. on Debonding, Structure, and Mechanical Properties of Metal-Ceramic Interfaces*, in the press.
- 25 A. G. Varias, R. J. Asaro and C. F. Shih, to be published.
- 26 A. Needleman, *Int. J. Fract.*, in the press.

Appendix A

A1. Failure of a perfect interface

Insight into the debonding process can be gained by examining a deformable crystal which is perfectly bonded on a rigid substrate. We consider a rectangular block which is perfectly bonded at its bottom edge to a rigid substrate and subject to the boundary conditions shown in Fig. A1. The block deforms under plane strain conditions. As indicated in the figure, the crystal has two slip systems, which are symmetric with respect to the direction of the applied load. Because of the boundary conditions imposed, a slip system with direction along the X_1 axis (see

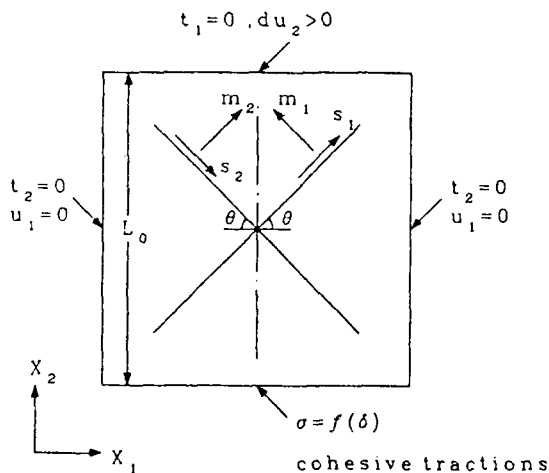


Fig. A1. Boundary value problem of a perfect interface. u_i and t_i are the components of the displacements and tractions respectively.

Fig. 1) cannot operate. To make the analysis tractable, we assume a rate-independent plastic response where slip is possible when the resolved shear stress $\tau_{(a)}$ reaches a critical value, which is equal to the hardness $g(\gamma_a)$ of the crystal. The results that we present are not particular to the details of the constitutive response and they are representative of the rate-dependent material response of the type considered in the main sections of this paper. The elastic response of the crystal is assumed to be isotropic.

The boundary conditions that are applied to the deformable block are similar to those applied to the model boundary value problem shown in Fig. 4. The displacement of the top boundary is monotonically increasing while the left and the right boundaries are held fixed. These three boundaries are free of tangential tractions. The bottom boundary is held to the rigid substrate by adhesive tractions. Since the displacement along the X_1 direction is zero, only normal adhesive tractions act across the interface, which obey the general relation $\sigma_n = f(\delta)$, where δ is the normal displacement of the bottom boundary. The analytic solution for infinitesimal strains is discussed.

The initial stiffness of the system is given by the relation

$$\left. \frac{d\sigma}{d(u/L_0)} \right|_{u=0} = \left\{ \frac{1}{E} \left(\frac{1-\nu-2\nu^2}{1-\nu} \right) + \frac{1}{L_0 f'(0)} \right\}^{-1} \quad (\text{A1})$$

where E and ν are Young's modulus and Poisson's ratio respectively, and $f'(0)$ is the slope of the adhesive relation at zero displacement. If the product $L_0 f'(0)$ of the height of the block and the initial stiffness is large compared with E , the system responds as if the adhesion is infinitely strong. Since $f'(0)$ scales with the ratio σ_{\max}/δ_c , an increase in the interface strength or decrease in the ratio δ_c/L_0 results in a stiffer initial response of the system. This behavior is also observed in the short-flaw problem.

Owing to the symmetry conditions, the resolved shear stress of both slip systems has the same absolute value and so does plastic slip along the two slip directions. Initial yielding occurs when $\tau_{(a)}$ reaches the initial hardness g_0 of the crystal, or equivalently when the stress $\sigma (= \sigma_{22})$ reaches the value σ_0 , i.e.

$$\sigma = \sigma_0 = \frac{2(1-\nu)}{(1-2\nu)} \frac{g_0}{\sin 2\theta}$$

The total strain increment is

$$\begin{aligned} d\epsilon_{ij} &= d\epsilon_{ij}^e + d\epsilon_{ij}^p \\ &= d\epsilon_{ij}^e + \sum_a d\gamma_{(a)} [m_i^{(a)} s_j^{(a)} + m_j^{(a)} s_i^{(a)}] \end{aligned}$$

where

$$d\epsilon_{22} = \frac{du - d\delta}{L_0} = d\epsilon_{22}^e + d\gamma \sin 2\theta$$

$$d\epsilon_{11} = 0 = d\epsilon_{11}^e - d\gamma \sin 2\theta$$

$$d\epsilon_{33} = d\epsilon_{33}^e = d\epsilon_{33}^p = 0$$

$$d\gamma_1 = -d\gamma_2 = d\gamma$$

It should be noted that the shearing strains are zero. The resolved shear stress on the first slip system is given by

$$\tau_1 = g(\gamma_a) = g(2\gamma) = \frac{1}{2}(\sigma - \sigma_{11}) \sin 2\theta$$

A similar relation holds for τ_2 . To determine the stresses, the above relations must be supplemented by the elastic stress-strain relations.

Combining the above relations and integrating the resulting expression, we get the relation for the stress σ as a function of the slip of the first system γ , i.e.

$$\sigma = \frac{E}{1-\nu-2\nu^2} \gamma \sin 2\theta + \frac{2(1-\nu)}{1-2\nu} \frac{g(2\gamma)}{\sin 2\theta} \quad (A2)$$

The crystal stress σ reaches a peak value of σ_{\max} (which is the strength of the interface). At this point the plastic slip γ also reaches its maximum value designated by γ_{\max} . Thereafter its value remains constant. Under the assumption that γ_{\max} is comparable with the elastic strains, we obtain the result

$$\begin{aligned} \gamma_{\max} &\approx \left\{ \frac{1-\nu-2\nu^2}{\sin 2\theta} \frac{\sigma_{\max}}{E} - \frac{2(1-\nu^2)}{(\sin 2\theta)^2} \frac{g_0}{E} \right\} \\ &\times \left\{ 1 + \frac{4(1-\nu^2)}{(\sin 2\theta)^2} \frac{h_0}{E} \right\}^{-1} \quad (A3) \end{aligned}$$

The above relation is obtained by assuming that $g(\gamma_a)$ is given by eqn. (5b) and taking the asymptotic expansion for small γ_a . A numerical solution of (A2) has shown that (A3) is rather accurate. This is not surprising because of the character of the highly constrained deformation caused by the prescribed boundary conditions.

At the peak stress σ_{\max} , the nominal strain ϵ_{nom}

of the system is given by

$$\begin{aligned} \frac{u}{L_0} \Big|_{\delta=\delta_m} &= \frac{\delta_m}{L_0} + \frac{1-\nu-2\nu^2}{1-\nu} \frac{\sigma_{\max}}{E} \\ &+ \frac{1-2\nu}{1-\nu} \gamma_{\max} \sin 2\theta \quad (A4) \end{aligned}$$

where u is the displacement of the top boundary of the crystal and δ_m is the normal interface displacement when the normal adhesive traction is at its maximum value of σ_{\max} . The above relations show that the nominal strain at the peak stress decreases when σ_{\max} or δ_m/L_0 decreases.

After reaching the peak stress the crystal unloads elastically as the process of de-adhesion proceeds. The crystal is completely debonded from the substrate when its bottom boundary displacement δ reaches a value equal to δ_c . The residual stress upon complete debonding is given by the difference between the elastic and the elastic-plastic solutions for the system when the applied stress is of magnitude σ_{\max} . The total engineering strain at complete debonding is determined by the permanent plastic strain and the elastic strain associated with the residual stress, i.e.

$$\frac{u}{L_0} \Big|_{\delta=\delta_c} = \frac{\delta_c}{L_0} + \gamma_{\max} \sin 2\theta - \frac{\nu}{1-\nu} \gamma_{\max} \sin 2\theta \quad (A5)$$

The first term on the right-hand side of (A5) is the contribution of the adhesive relation. The second term is due to the plastic deformation of the crystal along the X_2 direction and the third term is the elastic strain due to the σ_{11} and σ_{33} residual stresses. The last two terms vanish when the interface strength is smaller than the constrained yield strength σ_0 of the crystal. Thus, when the plastic deformation of the crystal is small, the engineering strain u/L_0 of the system at complete debonding is nearly given by δ_c/L_0 . This result was observed in the short-defect problem where the interface strength is smaller than $8g_0$.

At complete debonding, the work done by the applied load is

$$\begin{aligned} W &= \int_0^{\delta_c} f(\delta) d\delta + L_0 \int_0^{\gamma_{\max}} g(\gamma_a) d\gamma_a \\ &+ \frac{EL_0}{2(1-\nu^2)} (\gamma_{\max} \sin 2\theta)^2 \quad (A6) \end{aligned}$$

where

$$\frac{W_p}{L_0} = \int_0^{2\gamma_{\max}} g(\gamma_a) d\gamma_a \approx 2g_0\gamma_{\max} \quad (A7)$$

The above relation for the plastic work is valid for plastic slip which is comparable with the elastic strain.

Equation (A6) shows that the work done by the applied load is the sum of the work of de-adhesion, the work of plastic deformation of the crystal and the elastic energy stored in the crystal (due to the residual stresses). The last two terms vanish when the crystal deforms only elastically so that the work of the applied load is totally spent in the de-adhesion process. Therefore the ductility of the system is controlled by the work of de-adhesion, when the plastic strain of the crystal is small. In contrast, the ductility depends on both the work of de-adhesion and the work of plastic deformation, when the plastic strain of the crystal is comparable with δ_c/L_0 . The plastic work at system failure depends primarily on interface strength. In fact the interface strength is the only parameter of the adhesive relation governing the plastic work to failure in this problem. In other words, the ductility depends on interface strength. This simple problem is similar in some respects with the short-defect problems discussed in Section 4.3 and provides insight into those problems. It also explains the observations with regard to the mechanical response of a system containing a planar interface populated by a periodic array of cavities [A1].

The solution to the present boundary value problem assumes an even simpler form when J_2 flow theory is used. In this theory, the material hardens according to $\bar{\sigma} = H(\bar{\epsilon}^p)$. Initial yielding occurs when $\bar{\sigma} = \sigma_0$, i.e. when the applied stress is given by

$$\sigma = \frac{1-\nu}{1-2\nu} \sigma_0$$

After yielding has occurred, the strain increments are given by the relations

$$d\epsilon_{22} = \frac{du - d\delta}{L_0} = d\epsilon_{22}^e + d\bar{\epsilon}^p$$

$$d\epsilon_{11} = d\epsilon_{33} = 0 = d\epsilon_{11}^e - \frac{1}{2}d\bar{\epsilon}^p$$

$$d\epsilon_{11}^e = d\epsilon_{33}^e$$

It should be noted that all shear strains vanish. We also have the relation

$$\bar{\sigma} = \sigma - \sigma_{11} = H(\bar{\epsilon}^p)$$

Combining the above relations and integrating the resulting expression, we obtain

$$\sigma = \frac{1}{1-2\nu} \{ \frac{1}{2}E\bar{\epsilon}^p + (1-\nu)H(\bar{\epsilon}^p) \} \quad (A8)$$

Following the procedure described in the crystal plasticity case, similar relations for engineering strain at peak stress, total engineering strain and ductility are derived:

$$\left. \frac{u}{L_0} \right|_{\delta=\delta_m} = \frac{\delta_m}{L_0} + \frac{1-\nu-2\nu^2}{1-\nu} \frac{\sigma_{\max}}{E} + \frac{1-2\nu}{1-\nu} \bar{\epsilon}_{\max}^p \quad (A9)$$

$$\left. \frac{u}{L_0} \right|_{\delta=\delta_c} = \frac{\delta_c}{L_0} + \bar{\epsilon}_{\max}^p - \frac{\nu}{1-\nu} \bar{\epsilon}_{\max}^p \quad (A10)$$

$$W = \int_0^{\delta_c} f(\delta) d\delta + L_0 \int_0^{\bar{\epsilon}_{\max}^p} H(\bar{\epsilon}^p) d\bar{\epsilon}^p + \frac{EL_0}{4(1-\nu)} (\bar{\epsilon}_{\max}^p)^2 \quad (A11)$$

Finally we note that the perfect interface problem does not have always an equilibrium solution during unloading. The existence of an equilibrium solution depends on the interface and the material properties. During unloading, the bottom boundary displacement increment is larger than that prescribed on the top boundary, i.e.

$$0 \leq du \leq d\delta$$

The above inequalities, combined with the stress-strain relation during unloading, result in the following necessary condition for the existence of equilibrium solution:

$$0 \geq \frac{df}{d\delta} \geq -E \frac{1-\nu}{1-\nu-2\nu^2} \frac{1}{L_0} \quad (A12)$$

The left inequality is automatically satisfied in the unloading part of the adhesive relations. The right inequality gives a lower bound for the tangent of the adhesive relation during unloading.

The issue of existence of an equilibrium solution also arises in problems of debonding of imperfect interfaces, which were discussed in the main sections of this paper. It is clear that the existence of an equilibrium solution can be given in a manner similar to (A12). However, an explicit

relation cannot be found owing to the complexity of the boundary value problem.

Reference for Appendix A

A1 A. G. Varias, R. J. Asaro and C. F. Shih, to be published.